CERN-2004-007
15 July 2004
Accelerators and Beams
Department

ORGANISATION EUROPÉENNE POUR LA RECHERCHE NUCLÉAIRE
CERN EUROPEAN ORGANIZATION FOR NUCLEAR RESEARCH

LHC PROTON BEAM DIAGNOSTICS USING SYNCHROTRON RADIATION

L. Ponce, R. Jung and F. Méot[1]

GENEVA
2004

[1]CEA DAPNIA, Saclay, France

CERN Scientific Information Service–260–July 2004

ABSTRACT

A synchrotron light monitor will be used to carry out diagnostics using the transverse profiles of the Large Hadron Collider (LHC) proton beams. In order to optimize the performance over the whole LHC energy range (from 450 GeV up to 7 TeV), a comparative study of various types of source was undertaken. Analytical models for the determination of the angular spectral energy density emitted by these sources were studied; then simplifying models like the low-frequency model or the interference between source were used for some derivations. The study was then completed by numerical simulations to evaluate the sources' performance in more realistic conditions. The results obtained led to propose and launch the construction of a superconducting undulator with two 28 cm long periods. Combined with a separation dipole, the set-up makes it possible to measure beam profiles over the whole LHC energy range. The evaluation of the monitor's performance is supplemented by a detailed analysis of the optical system. The components of the telescope are described in order to evaluate the thresholds of detection. Then, the effects of diffraction and depth of field that constitute the limits of the system's resolution were studied numerically.

CONTENTS

FREQUENTLY USED SYMBOLS AND ABBREVIATIONS

$\alpha = \frac{B.L}{B\rho} = \frac{L}{\rho}$ [rad]	deflection of a long magnet of length L and magnetic field B
$\beta = \frac{v}{c} = \sqrt{\frac{\gamma^2-1}{\gamma^2}}$	normalized speed
$\beta_{h,v}$ [m]	betatron function in the horizontal (H) or vertical (V) plane
$B\rho = \frac{p}{q}$ [T.m]	rigidity of the particle
$c = 2.998 \times 10^8$ [m.s^{-1}]	speed of light in vacuum
$\epsilon_0 = 8.854 \times 10^{-12}$ [F.m^{-1}]	permittivity in vacuum
$\epsilon_{h,v}$ [m]	particle beam emittance, defined at 1 r.m.s., in the horizontal or vertical plane
$\epsilon_n = \epsilon_{h,v}\beta\gamma$ [m.rad]	particle beam normalized emittance
$E_0 = m_0c^2$ [GeV]	proton rest energy
$E = \gamma m_0 c^2$ [TeV]	proton beam energy
$\tilde{f}(\omega) = \frac{1}{\sqrt{2\pi}} \int_{-\infty}^{+\infty} f(t)e^{-i\omega t}dt$	definition of the Fourier transform
$\gamma = \frac{E}{E_0} = \frac{1}{\sqrt{1-\beta^2}}$	Lorentz factor
G	optical magnification
$g1$	spectral range 1.3–6.2 eV, or 200–900 nm
$g2$	spectral range 1.46–2.75 eV, or 450–850 nm
$g3$	spectral range 1.13–3.54 eV, or 350–1100 nm
IP	beam interaction point in LHC
IR	interaction region (straight section that houses an IP)
$k_u = \frac{2\pi}{\lambda_u}$	spatial frequency of the undulator
λ [m]	wavelength
$\lambda_1(\theta)$ [m]	wavelength emitted by an undulator in the θ direction on harmonic 1
λ_u [m]	undulator spatial period
$\mu_0 = 4\pi \times 10^{-7}$ [N.A^{-2}]	permeability ($\epsilon_0\mu_0 = 1/c^2$)
m_0 [kg]	mass of a particle, $m_0 = 1.672 \times 10^{-27}$ kg $= 938.272$ MeV for protons
$\nu = \frac{c}{\lambda}$ [Hz]	frequency
(ϕ, ψ)	angular coordinates defined in Fig. 7
$p = \gamma m_0 c$ [kg.m.s^{-1}] for $v \equiv c$	momentum of the particle
$q = 1.602 \times 10^{-19}$ [C]	electric charge of the particle
ρ [m]	curvature radius of the trajectory in a magnetic field
$r_0 = \frac{q^2}{4\pi\epsilon_0 m_0 c^2} = 1.535 \times 10^{-15}$ m	classical radius of the proton
$\sigma = \sqrt{Esp\left([X - Esp(X)]^2\right)}$	r.m.s. value, with $Esp(X)$ the average of X
t	'observer' time
t'	'particle' time
(x, y, z)	Cartesian coordinate axes
$\omega_0 = \frac{c}{\rho}$	angular velocity
$\omega_1 = \frac{4\pi\gamma^2 c}{\lambda_u(1+\gamma^2\theta^2)}$ [rad.s^{-1}]	frequency radiated in an undulator in the direction θ
$\omega_c = \frac{3\gamma^3 c}{2\rho}$ [rad.s^{-1}]	critical frequency
ω_l [rad.s^{-1}]	limit frequency defining the low-frequency approximation
$\cdot$	scalar product
$*$	convolution product
$\times$	vector product

1 INTRODUCTION

Any relativistic charged particle emits electromagnetic radiation, called synchrotron radiation, when it follows a curved trajectory [1]. Observed for the first time on 24 April 1947 [2] in a 70 MeV electron synchrotron, this radiation corresponds to a particle energy loss and was regarded for a long time as a limiting factor for the construction of high energy circular electron accelerators. The studies undertaken thereafter for a better understanding of the characteristics of this type of radiation made possible the development of electron storage rings dedicated to the production of intense synchrotron radiation for the analysis of the intrinsic properties of matter. Following the development of circular accelerators, another application also appeared: the use of synchrotron radiation for beam diagnostics [3]. This method, used on electron machines, is more difficult to implement for proton machines because of the much lower levels of emitted signals. However, the increase in the energy of accelerators and the development of increasingly sensitive optical detectors made beam profile measurement on proton synchrotrons possible [4]. The work completed here presents the developments which were necessary to design a synchrotron light installation intended to measure proton beam profiles over the whole energy range of the Large Hadron Collider (LHC).

Section 2 introduces the machine characteristics, the questions related to the transverse diagnostics, and the working constraints. In Section 3 the principal results of synchrotron radiation theory used for our study are recalled. Section 4 gathers various analytical calculations which were carried out to evaluate synchrotron radiation for various types of source, under various conditions of approximation. Without being an exhaustive catalogue of all the possible sources, it reviews sources usable in the LHC in order to compare them in terms of effectiveness for the diagnostics and for the choice of monitor. Section 5 presents the computer code Zgoubi, which was used where analytical calculation are no longer possible. After having confronted the numerical and analytical results in simple cases, this code was used to evaluate the spectral energy distribution under real conditions, in particular with magnetic field maps and in configurations with several interferential sources. In Section 6, the performance of the various sources studied for the LHC are presented. They are then compared in order to explain the choice of the solution proposed, according to the constraints of space and performance. Section 7 deals with the optical performance of the final monitor. It first presents the optical chain of the monitor, called telescope, then evaluates the different sources of resolution loss introduced by the optics (diffraction and depth of field) by taking into account the particular properties of the light source retained for the LHC.

2 LHC AND BEAM DIAGNOSTICS

2.1 Presentation of the machine

The Large Hadron Collider (LHC) is a proton–proton collider designed to allow high-energy physicists to answer the questions which the Standard Model still raises: the origin of the mass related to the existence of the Higgs field and its associated particle (Higgs boson), the existence of supersymmetric particles, extension of the Standard Model to gravity, etc.

In the LHC, the nominal centre-of-mass energy is 14 TeV in order to reach the interesting masses for the physics studies. The two proton beams are injected from the SPS at 450 GeV and then accelerated until the collision energy of 7 TeV.

In practice, the LHC (Fig. 1) is a machine of about 27 km circumference that uses superconducting magnets. It is made up of eight arcs and eight straight sections (IR) accommodating the four principal experiments (ATLAS in IR1, ALICE in IR2, CMS in IR5 and LHCb in IR8), acceleration (IR4), the cleaning sections (IR3 and IR7), and the extraction to the beam dump (IR6). The two beams circulate in two different vacuum chambers which cross each other only at the locations of the four experiments. The dipoles are of the two-in-one concept: the two beam pipes are incorporated in the same iron yoke.

The parameters of the LHC [5] are shown in Table 1.

2.2 The LHC beam

2.2.1 Definition of the beam emittance

The layout of an accelerator is defined for a nominal orbit of the particles. However, because of the presence of the various optical elements of the machine, the particles deviate from the nominal orbit while following 'betatron' oscillations. In the case of a circular machine, this movement is described by Hill's equations [6]:

$$u'' + K(s)u = 0 \tag{1}$$

Table 1: LHC nominal parameters

		Injection	Collision
Beam data			
Energy	[TeV]	0.45	7
Luminosity	[$cm^{-2}s^{-1}$]	10^{34}	
Normalized transverse emittance	[μm.rad]	3.75	
Mean circulating current per beam	[A]	0.56	
Number of particles per nominal bunch		1.1×10^{11}	
Number of particles per pilot bunch		5×10^{9}	
Number of bunches		2808	
Bunch spacing	[ns]	25	
r.m.s. length of bunch	[cm]	13	7.7
r.m.s. length of bunch	[ns]	0.434	0.257
Geometry			
Circumference	[m]	26658.883	
Vacuum chamber diameter	[mm]	56	
Separation between the vacuum chambers	[mm]	194	
Revolution frequency	[kHz]	11.25	
Main Dipole			
Number of main dipoles		1232	
Length	[m]	14.2	
Magnetic field	[T]	0.539	8.386
Radius of curvature	[m]	2784.32	
Separation dipole: type D2			
Length	[m]	9.45	
Magnetic field	[T]	0.17	2.65
Radius of curvature	[m]	8829.5	
Separation dipole: type D3			
Length	[m]	9.45	
Magnetic field	[T]	0.25	3.9
Radius of curvature	[m]	5993	

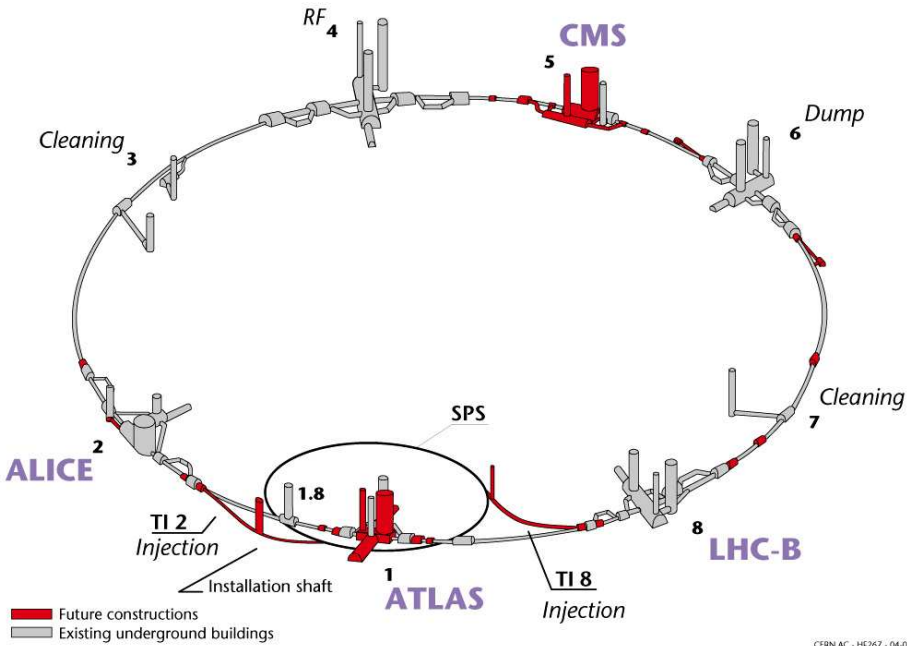

Fig. 1: Layout of the LHC

with $K(s)$ a periodic function, s the curvilinear coordinate and u the coordinate in the transverse plane (y or z). The general solution of this equation can be put under the form $u(s) = a\sqrt{\beta(s)}\cos[\mu(s) - S]$, with a and S two constants, $\beta(s)$ called betatron function, and $\mu(s)$ the phase function having the same periodicity as $K(s)$. From this general solution, it is possible to define an invariant of the movement, called the Courant–Snyder invariant:

$$\gamma(s)u^2(s) + 2\alpha(s)u(s)u'(s) + \beta(s)u'^2(s) = a^2 \tag{2}$$

with [2] α, β and γ Twiss parameters [7], bound by the relation $\beta(s)\gamma(s) = 1 + \alpha^2(s)$ and defined by the geometry of the machine. For a given s, Eq. (2) defines an ellipse of surface πa^2 in the space of (u, u'), called the phase space (Fig. 2). The Twiss parameters then determine the shape and the orientation of this ellipse.

In this space, each couple (u, u') represents a particle of the beam, and the ellipse of parameter a includes the particles having an a 'amplitude' of betatron oscillation. When the parameter a is such that 63% of the particles of the beam are contained in the ellipse then $a = \sqrt{\epsilon}$ and ϵ is called **beam emittance**[3]. The projection of the distribution n(u) of the particles in the beam on the coordinate u in the phase space (u, u') defines the beam profile (Fig. 2). The r.m.s. sizes of the Gaussian beam at the point of measurement, H for horizontal ($u = y$) and V for vertical ($u = z$), are written then for a non-dispersive region:

$$\sigma_{\mathrm{H,\,V}} = \sqrt{\beta_{\mathrm{H,V}}\ \epsilon_{\mathrm{H,V}}} \tag{3}$$

with $\beta_{\mathrm{H,\,V}}$ the horizontal or the vertical betatron function and $\epsilon_{\mathrm{H,\,V}}$ the horizontal or vertical emittance. Along the trajectory, the ellipse continuously changes in shape and orientation with the evolution of the Twiss parameters, but its surface remains constant and it returns to its initial shape after having described one complete period. Equation (2) describes the evolution of the Twiss parameters along s. Knowing two initial conditions u_0 and u'_0 at a reference point s_0 of the trajectory, the solution at any other point s is written using the transfer matrix:

$$\begin{aligned}\begin{pmatrix} u(s) \\ u'(s) \end{pmatrix} &= \begin{pmatrix} C(s) & S(s) \\ C'(s) & S'(s) \end{pmatrix} \begin{pmatrix} u_0 \\ u'_0 \end{pmatrix} \\ &= \begin{pmatrix} \cos\mu + \alpha(s)\sin\mu & \beta(s)\sin\mu \\ -\gamma(s)\sin\mu & \cos\mu - \alpha(s)\sin\mu \end{pmatrix} \begin{pmatrix} u_0 \\ u'_0 \end{pmatrix} .\end{aligned} \tag{4}$$

[2] Twiss parameter $\gamma(s)$ has not to be confused with the Lorentz factor $\gamma = \frac{E}{E_0}$.

[3] Another definition of the emittance is also used for machine optics. One defines the emittance as the surface containing 95% of the particles. The definition retained in this document is that used for the transverse diagnostics, namely the surface containing 63% of the particles.

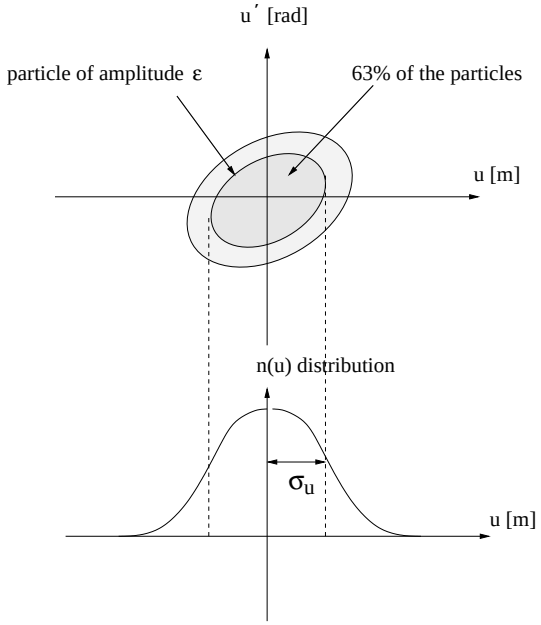

Fig. 2: Definition of the beam profile: projection on the H and V planes of the particle distribution

This transfer matrix gives the Courant–Snyder invariant at point s with the transport rule of the Twiss parameters:

$$\begin{pmatrix} \beta(s) \\ \alpha(s) \\ \gamma(s) \end{pmatrix} = \begin{pmatrix} C^2(s) & -2C(s)S(s) & S^2(s) \\ -C(s)C'(s) & S'(s)C(s)+S(s)C'(s) & -S(s)S'(s) \\ C'^2(s) & -2S'(s)C'(s) & S'^2(s) \end{pmatrix} \begin{pmatrix} \beta_0 \\ \alpha_0 \\ \gamma_0 \end{pmatrix} . \tag{5}$$

2.2.2 Beam dimensions in IR4 and IR5

After the choice of the collision energy, the characteristics of an accelerator are determined by the desired luminosity $\mathcal{L}$, i.e. the rate of proton–proton collisions per cm^2 and per second. A simplified expression of $\mathcal{L}$ is:

$$\mathcal{L} = \frac{I^2}{4\pi q^2 N f_{rev} \sigma_{\mathrm{H}} \sigma_{\mathrm{V}}} F \tag{6}$$

with I the circulating beam current, f_{rev} the revolution frequency, N the number of bunches, and F the reduction factor due to the angle between the beams at the interaction point. To increase the luminosity of the LHC, the optics is changed when the beam reaches the nominal energy. The β functions are decreased at collision points 1 and 5 in order to reduce the transverse beam dimensions σ_{H} and σ_{V} and to increase the luminosity. By the focusing principle, a small β at the IP means large β at the closest quadrupoles and thus larger beam dimensions, allowing a more comfortable measurement. The various optical functions of the regions where the size diagnostic could be done are given in Figs. 3–5.

Table 2 presents the $\beta_{\mathrm{H,\,V}}$ functions and beam dimensions $\sigma_{\mathrm{H,\,V}}$ for the two possible positions of the synchrotron radiation sources: the entry of the D3 dipole in IR4 and the entry of the D2 dipole in IR5.

2.3 Various methods of beam profile measurement

For the control of the machine, it is important to know precisely the transverse dimensions of the beams $\sigma_{\mathrm{H,\,V}}$. Since the emittance is an invariant of the beam, the knowledge of $\sigma_{\mathrm{H,\,V}}$ and $\beta_{\mathrm{H,\,V}}$ at a given point of the circumference yields the emittance $\epsilon_{\mathrm{H,\,V}}$ with Eq. (3). Then by optics transport with the matrix (5), it is possible to know the $\beta_{\mathrm{H,\,V}}$ functions in any other point of the machine and to calculate the local beam envelope $\sigma_{\mathrm{H,\,V}}$. Various methods of measurement of the transverse profiles are being developed in parallel for the LHC: the wire-scanners, the luminescence, ionization and synchrotron light profile monitors.

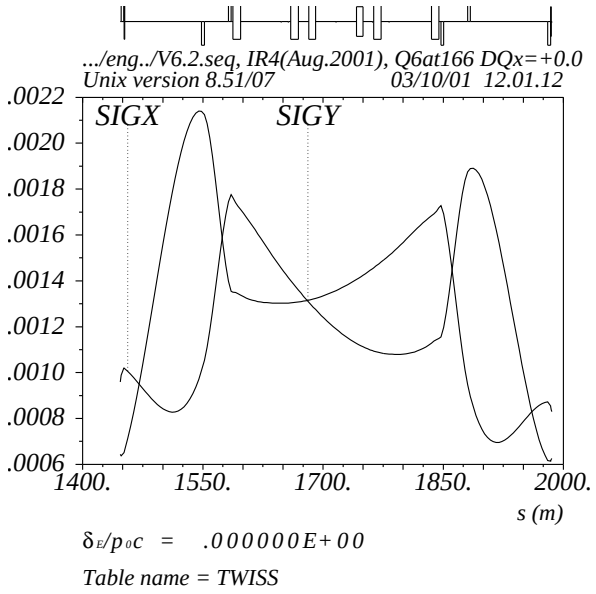

Fig. 3: Beam envelopes ($\sigma_{\rm H} = SIGX$ and $\sigma_{\rm V} = SIGY$) for 450 GeV in IR4. D3 is at $s = 1760$ m

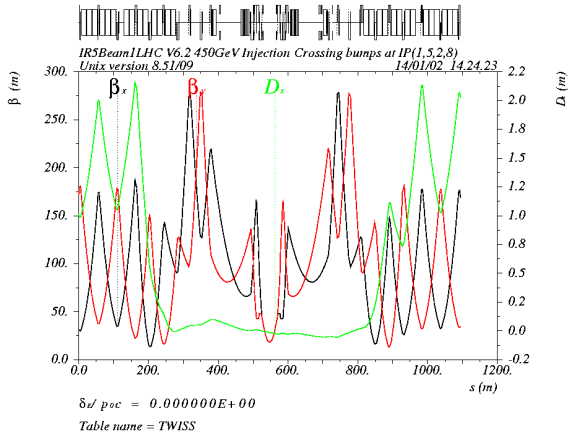

Fig. 4: Optical functions in IR5 at 450 GeV. D2 is in $s = 400$ m

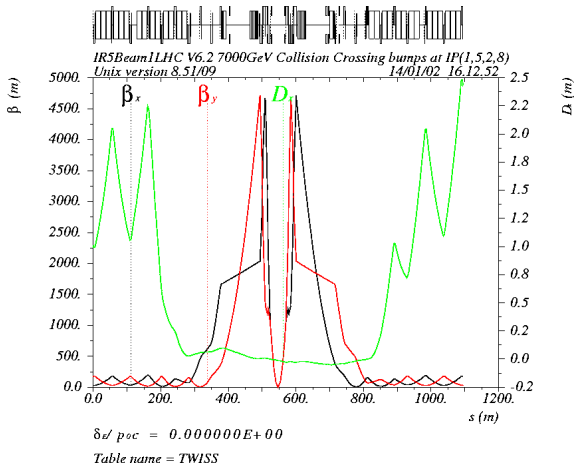

Fig. 5: Optical functions in IR5 at 7 TeV with the collision optics. D2 is in $s = 400$ m

Table 2: Beam dimensions at D3 in IR4 and at D2 in IR5

Energy (TeV)	γ	D3 in IR4				D2 in IR5			
		$\beta_{\rm H}$ (m)	$\sigma_{\rm H}$ (mm)	$\beta_{\rm V}$ (m)	$\sigma_{\rm V}$ (mm)	$\beta_{\rm H}$ (m)	$\sigma_{\rm H}$ (mm)	$\beta_{\rm V}$ (m)	$\sigma_{\rm V}$ (mm)
0.45	480.6	160	1.12	280	1.48	100	0.88	200	1.26
1	1066.3	160	0.75	280	0.99	100	0.59	200	0.83
2	2132.6	160	0.53	280	0.70	100	0.42	200	0.60
7 (injection)	7461.5	160	0.28	280	0.38	100	0.22	200	0.32
7 (collision)	7461.5	160	0.28	280	0.38	600	0.55	1840	0.96

Wire scanner: when a wire crosses the beam, secondary electrons of low energy are emitted by the wire, thus creating a current which can then be measured. Secondary particle are also emitted which can be measured by means of a scintillator. This system has a good resolution, but requires several passages of a bunch to give a profile and cannot thus measure an instability turn by turn. This measurement is also perturbative and will create a beam blow-up. In addition, a study carried out at CERN [8] showed that this system could not be used with the nominal intensity in the LHC since the heat produced will destroy the wire. It will be used to calibrate the other instruments over the whole energy range of the LHC beam by using a reduced number of bunches.

Luminescence: a gas (nitrogen N_2) is injected into the vacuum chamber [9]. As the beam passes through, the gas molecules are ionized and excited in N_2^+ ions which are de-excited by emitting photons of 391.4 nm wavelength. The direct observation of the emitted photons makes it possible to measure the beam profile. It is a simple device, but with a low sensitivity due to the low efficiency of luminescence. It should be of interest for high density beams.

Ionization profile monitor (IPM): the beam ionizes the residual gas in the vacuum chamber around 10^{-8} Pa. An electric field separates the ions and the emitted electrons [10]. Electrons, guided by a magnetic field to limit the angular divergence, or the ions, are collected and the signal is amplified by a multichannel plate (MCP). The electrons produced by the MCP are accumulated onto a screen of phosphorus and one observes the emitted light. This system has a higher efficiency than luminescence but may suffer from space charge effects.

Synchrotron light: the system uses the visible light emitted by the beam when travelling in an external magnetic bending field. This monitor is the subject of the work developed in this document and its principle is detailed in the following paragraph.

All these monitors provide projection in the vertical or horizontal plane of the image of the beam. But only the synchrotron light monitor provides a two dimensional image of the beam and has then the advantage to be able to observe a possible coupling between the horizontal plane and the vertical plane in the shape of a tilted ellipse compared to the transverse axes Oy and Oz. The synchrotron light monitor can also carry out bunch-by-bunch and turn-by-turn measurements.

2.4 Use of synchrotron radiation for diagnostics

The method using synchrotron radiation is a non-interceptive one and allows three types of measurements:

- the transverse dimensions of the beams by image forming,
- the angular divergence of the beam by direct observation without a focusing system [3] or at infinity when this divergence is large compared to the angular opening of the cone of radiation (which is not the case in the LHC),
- the longitudinal distribution of the particles by observing the temporal structure of the radiation [11].

In the following we are interested only in the first type of measurement, which makes it possible to obtain the beam emittance ϵ by supposing that the $\beta_{\mathrm{H,\,V}}$ functions are known with enough precision.

2.4.1 General principle of the monitor

When passing through a magnetic bending element, the beam emits radiation of which the visible spectral part is used and focused on a detector (Intensifier and CCD) by an optical system (Fig. 6) described more precisely in Section 7.1.2. The beam has a transverse spatial distribution of r.m.s. width σ. This radiation is **incoherent**, i.e. the total intensity collected is proportional to the number of particles in the beam. For a bunched beam, the radiation is incoherent for observed wavelengths lower than the bunch length. In the LHC case with σ_{bunch} = 7.7 cm and the observed wavelengths for protons in the range 200–900 nm, the criterion is satisfied. The spatial distribution of the intensity $D(y,z)$ collected on the detector, is thus the convolution product of the intensity distribution in the image plane of a single proton $I(y,z)$ (point spread function PSF) by the spatial distribution of the protons in the beam $O(y,z)$ [12]:

$$D(y,z) = I(y,z) * O(y,z)\ . \tag{7}$$

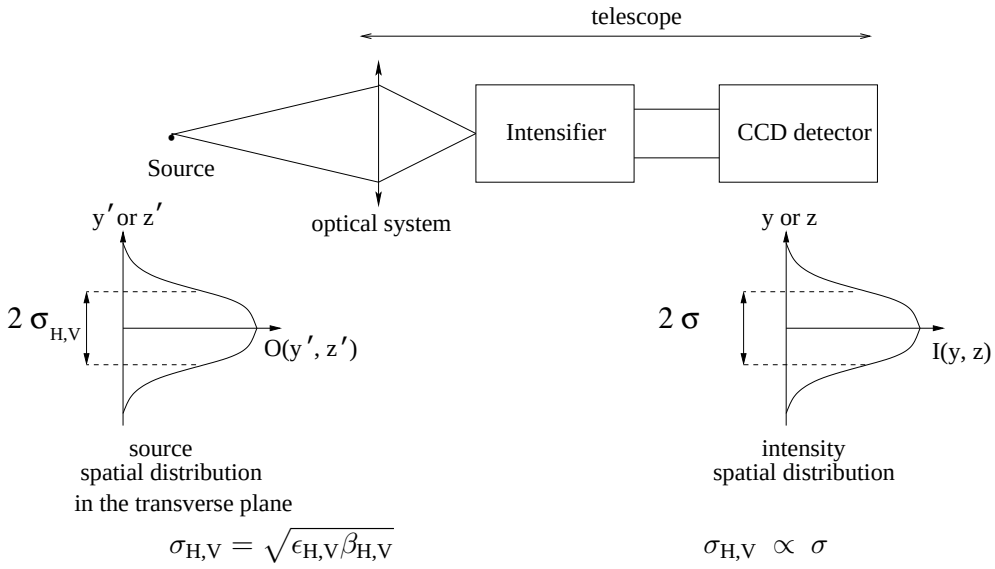

Fig. 6: Principle of the detector

By considering the optics as perfect, the r.m.s. width $\sigma_{\mathrm{H,\,V}}$ of $D(y,z)$ is thus related to the r.m.s. width σ of $O(y,z)$ and to the r.m.s. width of $I(y,z)$ (PSF), i.e. the image obtained for a point source. It is then necessary to add the various contributions of the optics defects (diffraction, depth of field, aberrations, etc.). To obtain a good precision of the profile measurement, it is necessary to calculate $I(y,z)$ by determining the intensity distribution radiated by a single proton (Sections 3, 4 and 6), and, the optical transfer function (Section 7).

Measurements of the horizontal and vertical profiles are obtained, as for the other monitors, by projections on the two planes. However, the synchrotron radiation monitor also provides an image in two dimensions of the beam allowing one 'to visualize' the shape of the particle distribution.

2.4.2 Working hypotheses

The work carried out to design a synchrotron radiation source and an optical chain to perform the required profile measurements is set out in the following sections. For a better understanding of the choices made, it is necessary to specify the particular conditions of use of the monitor and the constraints thus introduced.

Operating modes of the monitor. Two operating modes are foreseen for the synchrotron light monitor. The first one, 'TV mode', must provide an image in two dimensions used under normal operation over the whole energy range to observe the evolution of the beam envelope. The intensity collected is hence integrated over 20 ms (that is to say 225 turns in the LHC), the refreshing time of the video screens. In this case, the use of only a CCD camera as a detector is sufficient, if the level of signal is sufficient.

The second type of use, 'turn-by-turn mode', must make it possible to follow the evolution of a particle bunch or of a batch (a set of bunches) over individual turns. This implies a fast shutter (revolution period in the LHC of 89 μs) in front of the CCD. Indeed, the start-up scenario of the machine [13] foresees the injection and acceleration of a pilot bunch before a full-intensity filling. The profile monitor must thus be able to operate with this pilot bunch (5×10^9 particles). The collected intensity being directly proportional to the number of particles and the integration time, the addition of an intensifier in front of the CCD detector is necessary for this application. A Multi Channel Plate (MCP) intensifier will provide both functions.

Let us add that to measure profiles with 5% accuracy for the nominal bunch, taking into account the thresholds of sensitivity and of the noise on the CCD pixels, one needs a minimal energy emitted by a proton per turn of 1.5×10^{-23} J, Section 7.1.1.

Geometrical constraints. The light emitted by the beam is extracted from the vacuum chamber by a mirror, located in the vacuum chamber and sending the photon beam to the telescope. To avoid reducing the machine

acceptance, the edge of this mirror must remain at a minimal distance of 15 $\sigma_{\text{H or V}}$ from the beam axis, with $\sigma_{\text{H or V}}$ the r.m.s. width of the beam. Dimensions of the beam decrease when the beam energy increases (variation in $1/\sqrt{\gamma}$). It then appears possible to bring the mirror progressively closer to the beam axis during the energy ramp. This solution is, however, not adopted a priori in the various configurations studied because it requires a positioning system controlled by the beam energy. In our case, the strongest constraint is at the injection energy and the edge of the mirror is thus preferably at 15 $\sigma_{450\text{ GeV}}$ from the proton beam axis.

To collect the maximum amount of light, it is necessary to use the largest possible extraction mirror wrt the light cone. But taking into account the dimensions of the standard vacuum chamber, Table 1, the light extraction and the insertion of the mirror by respecting the specified distance compared to the proton beam axis require a local widening of the vacuum chamber. This must then be brought back to the standard dimension for the next elements of the machine. This condition limits the maximum distance between the source and the extraction mirror according to the space available at the location of the source in the machine (from 20 m in IR 5 to 62 m in IR 4, Figs. 3 and 4).

Since a very high quality mirror is required (surface flatness greater than $\lambda/10$), a square mirror 40 mm or 50 mm wide is considered according to the possible widening of the vacuum chamber. Thus, in the following, the mirror dimensions and the distance to the extraction will be specified for each configuration studied.

Constraints over the exploitable wavelengths. After the extraction mirror, the light is extracted from the vacuum chamber through a quartz window to be transparent to ultraviolet rays. The bandwidth (at 90% of transmission) of the window corresponds to a wavelengths range between 200 and 2500 nm.

In addition, the optical detector used will be a CCD camera with an intensifier, Section 7.1. The bandwidths vary according to the types, but the typical values used in the following are as follows. Two ranges are used for the CCD camera: g1 = [200–900 nm] and g3 = [350–1100 m]; and one range for the intensifier (for example of type 'super S25' [14] doped to shift the bandwidth toward the red) : g2 = [450–850 nm].

3 SYNCHROTRON RADIATION: THEORETICAL REMINDER

The theory of synchrotron radiation has been developed in many reference books [1, 15, 16]. We shall thus just point out here the principal results that were directly used for the calculations which follow. First of all, the expression of the electric field received by the observer according to his position and to the observation frequency is given starting from the retarded potentials. This formula is used as a basis, in Section 4, for the approximations making it possible to analytically derive the Fourier transform of this electric field. It also allows to determine the spectral angular energy densities which it is possible to produce with the various types of sources present in the LHC layout.

3.1 Field emitted by a moving particle

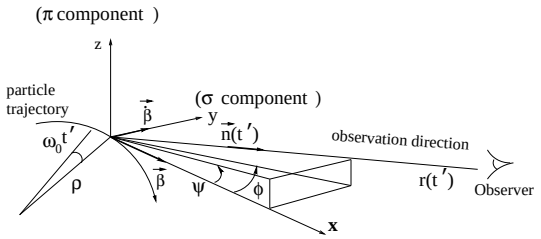

Fig. 7: Reminder of the notations

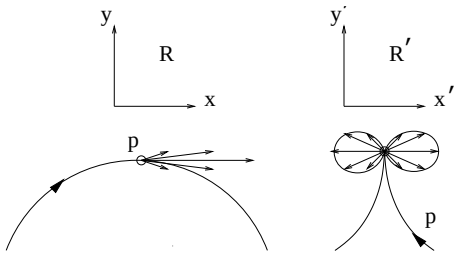

Fig. 8: Trajectories of the particle in the reference R and R' frames

3.1.1 The time-scales

When a charged particle is accelerated, it emits, at time t', an electromagnetic radiation which propagates. A fixed observer located at the distance $\vec{r}(t')$ from the particle, which varies with the particle movement, receives this

radiation at the time t (Fig. 7) given by:

$$t = t' + \frac{\vec{r}(t')}{c} \tag{8}$$

where c is the speed of light in vacuum. t' is called the 'particle time' and t the 'observer time'.

In the R' reference frame moving at the speed of the particle and tangentially to the trajectory, the particle describes a cycloid with a strong acceleration at the cusp (Fig. 8, right-hand side). The radiation of the charge in the R' reference frame has a space-distribution like that of an oscillating dipole. When returning in the fixed frame R of the observer by applying the Lorentz transformation, a photon emitted at 90 degrees with respect to the tangent to the trajectory in R' appears at an angle $1/\gamma$ in R. Hence, the radiation is concentrated in the forward direction in a cone with an angular opening $1/\gamma$ (Fig. 8, left-hand side).

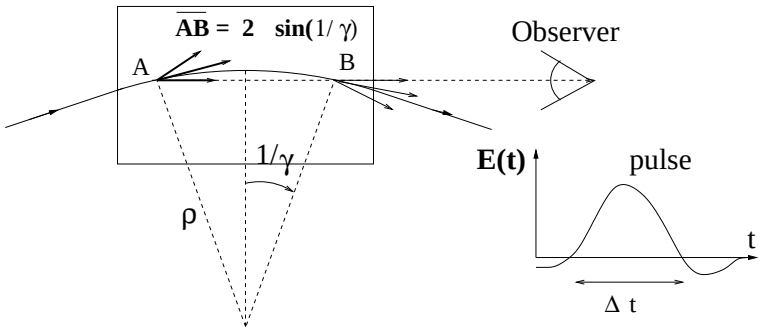

Fig. 9: Duration of the electric field pulse

Taking into account the small angular opening of the light cone for relativistic particles (typically some mrad), the observer 'sees', in practice, the radiation only between the point A, where the trajectory forms an angle $-1/\gamma$ with the observation direction, and the point B, where the trajectory forms an angle +1/γ with the observation direction (Fig. 9). The duration of the electric field pulse Δt received by the observer corresponds to the difference between the particle travel time $t_{\rm p}$ through the arc $\overset{\frown}{\rm AB}$ and the travel time $t_{\rm photon}$ through the segment $\overline{\rm AB}$ by the photon emitted in A:

$$\Delta t = t_{\rm p} - t_{\rm photon} = \frac{2\rho}{\beta\gamma c} - \frac{2\rho \sin 1/\gamma}{c} \ , \tag{9}$$

where ρ is the curvature radius of the arc $\overset{\frown}{\rm AB}$, and β the normalized speed of the particle. For relativistic particles, $\gamma \gg 1$ and $1 - \beta \simeq \frac{1}{2\gamma^2}$, therefore:

$$\begin{aligned} \Delta t &\simeq \frac{2\rho}{\beta\gamma c}\left(1 - \left(\beta - \frac{\beta}{6\gamma^2}\right)\right) \\ &\simeq \frac{2\rho}{\gamma c}\left(\frac{1}{2\gamma^2} + \frac{1}{6\gamma^2}\right) \\ \Delta t &\simeq \frac{4\rho}{3\gamma^3 c} \ . \end{aligned} \tag{10}$$

3.1.2 Radiated field

The electromagnetic field received at time t is calculated starting from Maxwell's equations and the Liénard–Wiechert potentials giving the retarded potentials created at time t' by a moving charge. These calculations will not be detailed here because largely developed in several reference books (see for example Refs. [1, 16]). The electric and magnetic fields emitted by a charge q with the speed $\vec{v} = \vec{\beta}c$ are written:

$$\vec{E}(t) = \frac{q}{4\pi\epsilon_0}\left(\frac{(1-\beta^2(t'))(\vec{n}(t') - \vec{\beta}(t'))}{r^2(t')(1 - \vec{n}(t')\cdot\vec{\beta}(t'))^3} + \frac{\vec{n}(t') \times \left[(\vec{n}(t') - \vec{\beta}(t')) \times \dot{\vec{\beta}}(t')\right]}{cr(t')(1 - \vec{n}(t')\cdot\vec{\beta}(t'))^3}\right) \tag{11}$$

$$\vec{B}(t) = \frac{\vec{n}(t') \times \vec{E}(t')}{c} \tag{12}$$

where ϵ_0 is the vacuum permittivity and $\vec{n} = \vec{r}/r$ the direction of observation (Fig. 7).

In our application, the observation is done at a long distance from the synchrotron radiation source. The first term of Eq. (11), proportional to $1/r^2$ (speed field), becomes then negligible compared to the second term, proportional to $1/r$ (acceleration field), and the electric field at the observer can be written in the form:

$$\vec{E}(t) = \frac{q}{4\pi\epsilon_0 c} \frac{\vec{n}(t') \times \left[(\vec{n}(t') - \vec{\beta}(t')) \times \dot{\vec{\beta}}(t') \right]}{r(t')(1 - \vec{n}(t') \cdot \vec{\beta}(t'))^3} \quad . \tag{13}$$

3.2 Various expressions of the electric field

The calculation of the electric field in particle time t' and observer time t was already derived [16] in the case of the synchrotron radiation emitted by a particle on a circular orbit: the problem is then independent of the observer's position in the plane of the orbit and thus of the angular variable ϕ (Fig. 7). Nevertheless, for the majority of the sources studied for the diagnostics in the LHC, the magnetic field crossed by the particle along the observed portion of trajectory is not necessarily uniform. The sole dependence in ψ of the expressions is not sufficient any more and calculation in three dimensions is necessary.

3.2.1 In particle time t'

With the notations of Fig. 7, by taking ϕ = 0 for $\omega_0 t' = 0$ (with $\omega_0 = c/\rho$ the angular velocity and ρ the curvature radius), the vectors $\vec{n}$, $\vec{\beta}$ of Eq. (13) are written:

$$\vec{n} = (\cos\psi\cos\phi, \cos\psi\sin\phi, \sin\psi) \quad , \quad \vec{\beta} = \beta(\cos\omega_0 t', \sin\omega_0 t', 0) \quad . \tag{14}$$

It is convenient to use the radiation component in the trajectory plane, called σ (or horizontal) component, and the component orthogonal to the trajectory plane, called π (or vertical) (Fig. 7). In the far field approximation and taking into account the weak angular opening of the radiation, it is possible to make a series expansion of the co-ordinates by retaining only the terms up to second order in ϕ, ψ and with $\beta \simeq 1 - 1/(2\gamma^2)$. Equation (13) then gives the two components:

$$\begin{aligned} E_\sigma(t') &\simeq \frac{q\omega_0\gamma^4}{\pi\epsilon_0 cr} \frac{(1+\gamma^2\psi^2) - \gamma^2(\omega_0 t' - \phi)^2}{(1+\gamma^2\psi^2+\gamma^2(\omega_0 t' - \phi)^2)^3} \\ E_\pi(t') &\simeq \frac{q\omega_0\gamma^4}{\pi\epsilon_0 cr} \frac{-2\gamma\psi\gamma(\omega_0 t' - \phi)}{(1+\gamma^2\psi^2+\gamma^2(\omega_0 t' - \phi)^2)^3} \quad . \end{aligned} \tag{15}$$

3.2.2 In observer time t

The preceding expression (15) makes it possible to obtain the electric field $\vec{E}(t')$ emitted by the particle. For the application considered, i.e. the profile measurement, it is the intensity at the observation point which should be known and thus the field received by the observer $\vec{E}(t)$. The calculation developed in the following is a generalization of the method, developed in Ref. [16], that accounts for non-zero ϕ component of the (ϕ, ψ) observation direction. For ultra-relativistic particles ($\gamma \gg 1$), by using the expansion of order 2 of the co-ordinates (14), the relation (8) between t and t' is written according to the position (ϕ, ψ) of the observer:

$$t \simeq \frac{1+\gamma^2(\phi^2+\psi^2)}{2\gamma^2} t' - \frac{c\phi}{2\rho} t'^2 + \frac{c^2}{6\rho^2} t'^3 \tag{16}$$

or, by differentiation and rearrangement of the terms:

$$\frac{dt}{dt'} = 1 - \vec{n}(t')\vec{\beta}(t') \simeq \frac{1+\gamma^2\psi^2+\gamma^2(\omega_0 t' - \phi)^2}{2\gamma^2} \quad . \tag{17}$$

To obtain $\vec{E}(t)$ starting from Eqs. (15) according to t', it is necessary to calculate $t'(t)$ by reversing relation (16). The trigonometric method of solving a cubic equation gives in this case:

$$t' = -2\frac{\rho}{c\gamma}\sqrt{1+\gamma^2\psi^2}\,\sinh\left[\frac{1}{3}\mathrm{Asinh}\,u\right] + \frac{\rho\phi}{c} \tag{18}$$

where

$$u = \frac{1}{2}\frac{\gamma\phi}{\sqrt{1+\gamma^2\psi^2}}\left(3+\frac{\gamma^2\phi^2}{1+\gamma^2\psi^2}\right) - 2\frac{\omega_c}{(1+\gamma^2\psi^2)^{3/2}}t \ . \tag{19}$$

When using these expressions in Eq. (15), the electric field received by the observer becomes:

$$\begin{aligned} E_\sigma(\phi,\psi,t) &= \frac{q\omega_0\gamma^4}{\pi\epsilon_0 cr(1+\gamma^2\psi^2)^2}\frac{(1-4\sinh^2[\frac{1}{3}\,\mathrm{Asinh}\,u(\phi,\psi,t)])}{(1+4\sinh^2[\frac{1}{3}\,\mathrm{Asinh}\,u(\phi,\psi,t)])^3} \\ E_\pi(\phi,\psi,t) &= \frac{q\omega_0\gamma^4}{\pi\epsilon_0 cr(1+\gamma^2\psi^2)^{5/2}}\frac{4\gamma\psi\sinh[\frac{1}{3}\,\mathrm{Asinh}\,u(\phi,\psi,t)]}{(1+4\sinh^2[\frac{1}{3}\,\mathrm{Asinh}\,u(\phi,\psi,t)])^3} \ . \end{aligned} \tag{20}$$

The angular spectral energy density is obtained by calculating the temporal Fourier Transform (FT) of Eqs. (20). In the general case, this operation is not possible in an analytical way and requires a numerical calculation. To facilitate the analytical calculation of the FT, it is often preferable to change the variable to arrive at a calculation in particle time t' in order to use the approximate expression (15), a rational fraction of t'.

3.3 Angular spectral energy density and intensity at the observer

The instantaneous energy flux (watt/m^2) transported by an electromagnetic wave is calculated starting from the Poynting vector $\vec{S}$:

$$\vec{S} = \frac{1}{\mu_0}\vec{E}\times\vec{B} = \frac{1}{\mu_0 c}\,\vec{E}^2\,\vec{n} \ . \tag{21}$$

The energy received when the particle passes in the magnetic element is calculated then by integrating the Poynting vector on the surface (Σ) of the detector related to the solid angle (Ω) by $d\Sigma = r^2(t)d\Omega$ and over the duration of the pulse (Δt):

$$W = \int_\Sigma\int_{\Delta t}|\vec{S}|d\Sigma dt = \frac{1}{\mu_0 c}\int_\Omega d\Omega\int_{\Delta t}\vec{E}^2 r^2(t)dt \tag{22}$$

where $r(t)$ is the distance at the time t between the particle and the observer. When this is large with respect to the source length, it is useful to consider $r(t) = r =$ constant in the calculation of the integral. However, for calculations of intensity with several successive sources, the validity of this approximation must be checked.

By considering that there is no emission outside the interval Δt, it is possible to extend the limits of the temporal integration to infinity and to use the Fourier Transform (FT) of the electric field [16] defined by:

$$\tilde{\vec{E}}(\omega) = \frac{1}{\sqrt{2\pi}}\int_{-\infty}^{\infty}\vec{E}(t)e^{-i\omega t}dt \quad \text{and its inverse} \quad \vec{E}(t) = \frac{1}{\sqrt{2\pi}}\int_{-\infty}^{\infty}\tilde{\vec{E}}(\omega)e^{i\omega t}d\omega \tag{23}$$

where $\omega = 2\pi c/\lambda$ is called the frequency and λ the wavelength of the considered emission. By using Parseval's theorem:

$$\int_{-\infty}^{\infty}|\tilde{\vec{E}}(\omega)|^2 d\omega = \int_{-\infty}^{\infty}|\vec{E}(t)|^2 dt \ . \tag{24}$$

Equation (22), with $r =$ constant, is written:

$$W = \frac{2r^2}{\mu_0 c}\int_\Omega\int_0^\infty|\tilde{\vec{E}}(\omega)|^2 d\Omega d\omega \tag{25}$$

by considering only the positive frequencies for the FT. The spectral energy density received at time t by an observer located at the distance $r(t)$ from a particle radiating at time $t' = t - \vec{r}(t')/c$ results from the preceding equations:

$$\frac{\partial^2 W}{\partial\omega\partial\Omega} = 2\epsilon_0 cr^2|\tilde{\vec{E}}(\omega)|^2 \ . \tag{26}$$

This last equation is the basis for the majority of analytical and numerical calculations of intensity received at the observation point developed in the following. To calculate the intensity received on a detector, it is enough to integrate it over the frequency bandwidth $\Delta\omega$ and over the angular acceptance $\Delta\Omega$ of the system considered.

4 MODELS FOR THE CALCULATION OF THE INTENSITY

The development of a transverse system of beam diagnostics for the LHC goes through two stages:

1. the choice of the synchrotron radiation source and thus the evaluation of the photon flux which one can collect,
2. the study of the optics allowing to obtain the image of the beam and thus the evaluation of the diffraction and depth of field effects related to the source specificities.

These two stages, in theory independent, pass nevertheless by the same determination of the characteristics of the synchrotron radiation received by the observer. The calculations presented in the preceding section showed that the emitted electric field depends on the trajectory of the particle and thus on the shape of the traversed magnetic field. Various types of synchrotron radiation sources are envisaged, defined according to the magnetic field that generates them: infinitely long dipole (constant field); short magnet (angular deflection lower than the light cone opening); edge effect (fast variation of the magnetic field at the ends of a dipole); undulator (sinusoidal field). This section presents, first of all, the analytical models that describe these sources. These results will be used in particular in the following section to validate the numerical methods. Then, methods of calculation in combination with the simplifying low-frequency model are exposed. These methods allow the evaluation of the intensities produced by a succession of sources.

4.1 Various models of sources

4.1.1 Dipole

The first source studied historically, which is also that present in all machines, is the dipole. It is the solution already successfully used for the diagnostics of electron and positron beams at LEP [17]. In this case, the magnetic field is regarded as uniform on a portion of the trajectory much larger than the characteristic length L_0 of an arc of opening angle $1/\gamma$ (Fig. 9):

$$L_0 = \frac{m_0 c}{qB} = \frac{\rho}{\gamma} \tag{27}$$

where m_0 is the mass of the particle, q its charge, B the magnetic field seen by the particle, and ρ the radius of curvature of the trajectory. The expression of the power radiated in the trajectory plane ($\psi = 0$) is given in many publications [1, 15, 16]). It is obtained starting from the angular spectral energy density [Eq. (26)], the Fourier transform being calculated from Eq. (13). One thus has

$$\frac{\partial P}{\partial \omega \partial \Omega}(\psi, \omega) = \left(\frac{3}{2\pi}\right)^3 P_0 \frac{\gamma}{\omega_c} \frac{\xi^2}{(1+\gamma^2\psi^2)} \left[K_{2/3}^2(\xi) + \frac{\gamma^2\psi^2}{1+\gamma^2\psi^2} K_{1/3}^2(\xi)\right] \tag{28}$$

where $\omega_c = 2\pi\nu_c = \frac{3c\gamma^3}{2\rho} \simeq \frac{2}{\Delta t}$ is the critical frequency in rad.s^{-1}, $P_0 = \frac{2}{3}\frac{1}{4\pi\epsilon_0}\frac{cq^2\gamma^4}{\rho^2}$ is the total power radiated by a particle in J.s^{-1}, $\xi = \frac{\omega}{2\omega_c}(1+\gamma^2\psi^2)^{3/2}$, $K_{1/3}$ and $K_{2/3}$ are the modified Bessel functions.

The term between square brackets represents the sum of the contributions of each polarization, that with $K_{2/3}$ comes from the σ component and that with $K_{1/3}$ defines the π component (Fig. 7).

The integration over all the solid angle of Eq. (28) allows to obtain the spectral energy density represented on Fig. 10. The curve is characterized by the position ω_c, which cuts the energy spectrum in two parts of the same integrated value, and defined as two times the inverse of the duration of the electric field impulse Δt received by the observer [Eq. (10)].

Figure 10 shows that, for a long dipole, the curves of spectral energy density have the same shape whatever ω_c and are simply 'relocated'. Moreover, for a given observation frequency bandwidth, for example g3 shown in gray, the relative position of ω_c is decisive for the level of collected signal: in the case of the 7 TeV protons in the LHC and of the 45 GeV electrons in LEP (ω_c above g3), the level of signal is about the same. It is, however, orders of magnitude higher than that from the 450 GeV protons in the LHC (ω_c below g3). In the case of the LHC main dipole, the critical frequency is determined by the machine parameters and cannot be adjusted. The dipole thus does not provide enough intensity at 450 GeV. This is why other types of sources are considered with the aim of increasing the radiation for $\omega > \omega_c$, at injection.

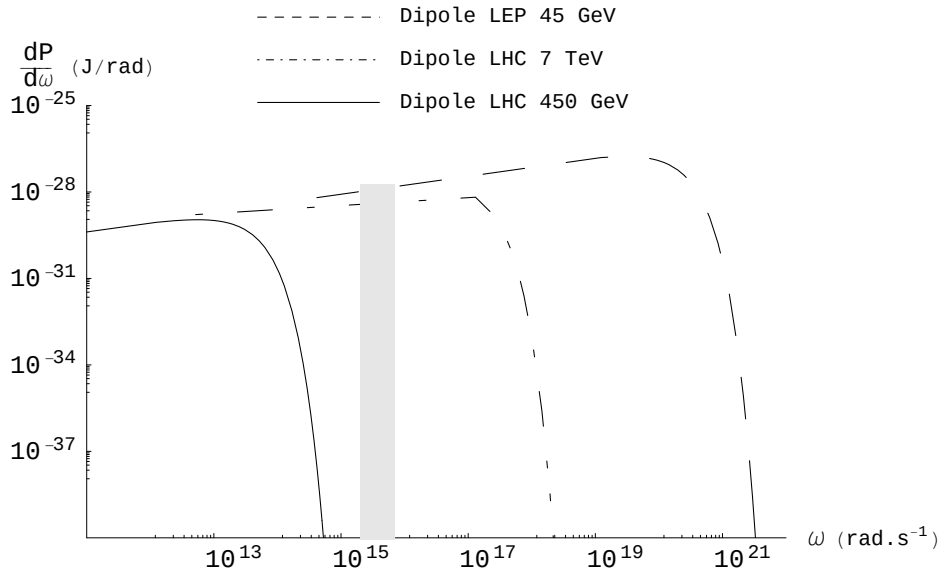

Fig. 10: Spectral energy density for an LHC dipole for a proton at 450 GeV and 7 TeV and a LEP dipole for an electron at 45 GeV. The gray shaded rectangle represents the frequency range g3.

4.1.2 Short magnet

A short magnet is a dipole in which the particle deflection $\alpha = BL/B\rho$ satisfies $\alpha \ll 1/\gamma$ (Fig. 11). The trajectory length L in the source is then much shorter than the characteristic length L_0 defined by Eq. (27).

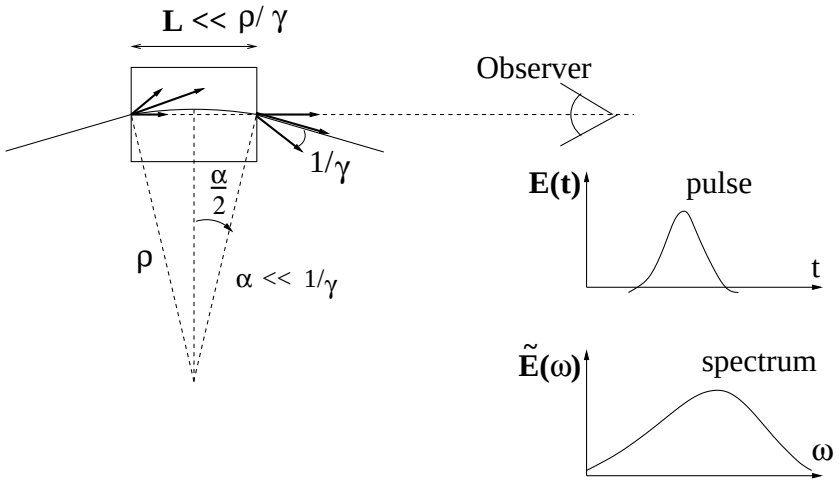

Fig. 11: Short magnet

The duration of the electric field impulse is thus shorter:

$$\Delta t = \frac{L}{\beta c} - \frac{L}{c} \simeq \frac{L(1-\beta)}{\beta c} \simeq \frac{L}{2\gamma^2 c} \tag{29}$$

and the increased critical frequency of the spectrum ω_c is written

$$\omega_{c,short\ magnet} = \frac{4\pi c\gamma^2}{L} \quad . \tag{30}$$

With equivalent beam energy, the short magnet allows to shift the maximum of the spectral density toward detectable frequencies compared to the case of the dipole. For example, $\omega_c = 5.6 \times 10^{13}$ rad.s^{-1} at 450 GeV for a LHC main dipole, while for a 50 cm long short magnet, $\omega_c = 1.7 \times 10^{15}$ rad.s^{-1} (to be compared for example with g3 = $1.7 \times 10^{15} - 5.4 \times 10^{15}$ rad.s^{-1}).

We saw previously that the radiated power can be expressed from the Fourier transform of the electric field [Eq. (26)]. In the 'short magnet' approximation, the observation direction $\vec{n}$ can be considered as constant: $\vec{n} \cdot \vec{\beta} = \beta \cos \alpha \simeq \beta$ (as $\alpha \ll 1/\gamma$). The Fourier transform of the electric field is then, according to Eq. (12), proportional to the FT of the magnetic field [18]:

$$\frac{\partial P}{\partial \Omega \partial \nu} = C^2 \gamma^6 f^2 \tilde{B}^2(t) = \frac{1}{4} C^2 \gamma^2 f^2 (1 + \gamma^2 \theta^2)^2 \tilde{B}^2 \left(\frac{1 + \gamma^2 \theta^2}{2\gamma^2} \nu \right) \tag{31}$$

where $C = \left(\frac{e^2}{\pi m}\right) \left(\frac{1}{\epsilon_0 c}\right)^{1/2} = 9.45 \times 10^{-11}$ m$^{3/2}$.s$^{-1/2}$ for protons and f is a function of the angles θ and φ (Fig. 12), with $f^2 = (1 + \gamma^2\theta^2)^{-6}[(1 - \gamma^2\theta^2)^2 + 4\gamma^2\theta^2 \sin^2 \varphi]$. The function $\tilde{B}\left(\frac{1+\gamma^2\theta^2}{2\gamma^2}\nu\right)$ is obtained from the Fourier transform of $B(t') = B(x/c)$ by replacing the variable ν' corresponding to t' by $\frac{1+\gamma^2\theta^2}{2\gamma^2}\nu$.

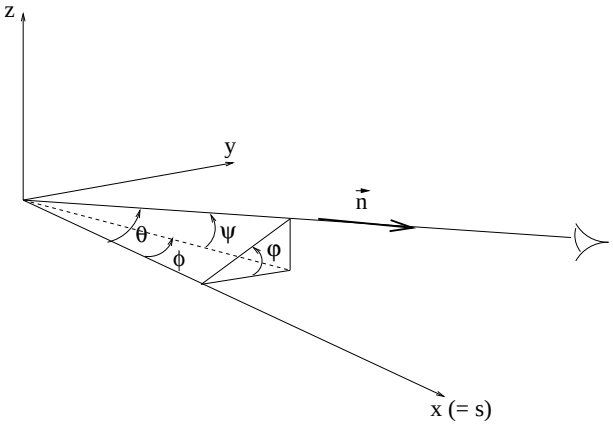

Fig. 12: Correspondence between the (ϕ, ψ) and (θ, φ) angles

4.1.3 Edge effect

The edge effect is the emission of radiation by the particle when it crosses the fringe field of a dipole, i.e. the variation of the dipole end's magnetic field along a few tens of centimetres. The typical duration of the electric field impulse is then again very short compared to that emitted in the long dipole. If one is interested in frequencies higher than the critical frequency of the dipole, it is a particular case of a short magnet, which has the advantage of not having to insert an additional magnet in the machine layout: it is possible to use the fringe field of the bending magnet. This technique was already used successfully in the Sp$\bar{\text{p}}$S [4] and in the SPS [19].

The angular spectral energy density is still given by Eq. (26). The difficulty in this case is to find an analytical expression representing the fringe field of the magnets [18]. For the LHC dipoles, the model of fringe field used is of the type:

$$B(x) = B_0 \left[\frac{1}{2} + \frac{1}{\pi} \arctan \frac{x}{L} \right] = \frac{B_0}{\pi L} \frac{1}{1 + (x/L)^2} * H(x) \tag{32}$$

where $H(x)$ is the Heaviside distribution, * indicates the convolution product, and B_0, the peak field, depends on beam energy.

4.1.4 Undulator

An undulator is a periodic magnetic structure generally used to produce quasi-monochromatic synchrotron radiation (Fig. 13). In the case of a harmonic plane undulator, of spatial period λ_u, the magnetic field produced is of the

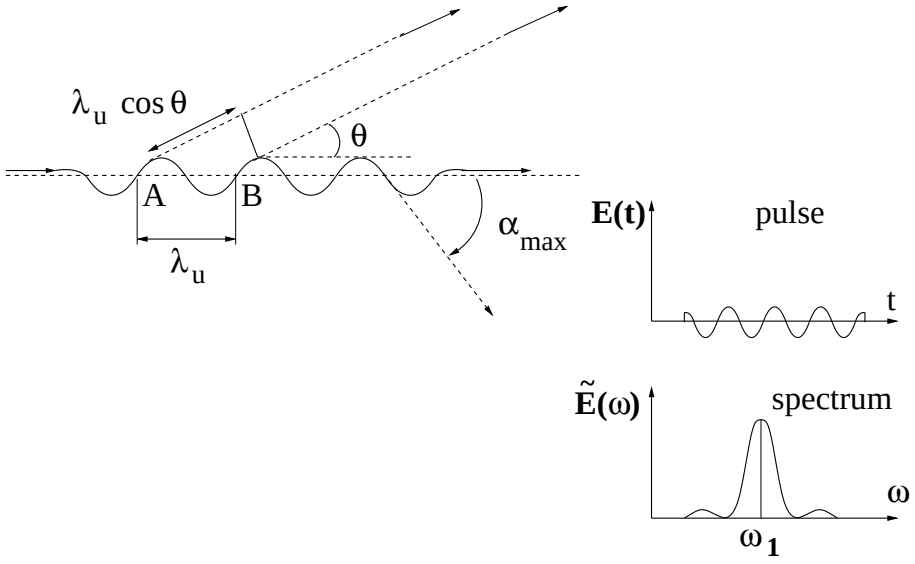

Fig. 13: Scheme of an undulator

form:

$$B(x) = B_z(x) = B_0 \cos(k_u x) \tag{33}$$

where $k_u = 2\pi/\lambda_u$ and B_0 is the peak field. If the magnetic field is not too strong, the particle undergoes small oscillations around the x axis:

$$y(x) \simeq \frac{qB_0}{m_0 c\gamma k_u^2} \cos(k_u x) \ . \tag{34}$$

The undulator deflection parameter, characterizing the relationship between the maximum deflection angle α_{max} and the natural opening of the synchrotron radiation $1/\gamma$, is defined by:

$$K = \frac{qB_0\lambda_u}{2\pi m_0 c} = \gamma\alpha_{max} \ . \tag{35}$$

When K is greater than 1, the opening of the light cone is small compared to the deflection, and the observed radiation comes mainly from the tops of the sine-like trajectory. The received electric field consists of a series of peaks whose Fourier transform contains a series of harmonics. One speaks in this case of a 'wiggler'. On the other hand, when K is smaller than 1, the cone of radiation is broader than the deflection and the observer 'sees' the whole trajectory. The transform of this quasi-sinusoidal electric field results in a narrow spectrum. One speaks then of an 'undulator'.

For protons, with typical maximum values of magnetic field of the order of one tesla and a period λ_u of a few tens of centimetres, the typical values of K are some 10^{-2} thus $K \ll 1$. For low values of K, one can apply the small oscillation approximation in the calculation of the particle trajectory in the undulator [16]. The radiation emitted presents a relation of temporal coherence, giving place to an interferential behaviour [20]. In two equivalent points A and B of the trajectory (i.e. separated by one period λ_u) (Fig. 13), the particle emits in the direction θ two wave fronts, separated by the distance d corresponding to the delay taken by the particle on the wave front emitted in A to arrive at B:

$$d = \frac{\lambda_u}{\beta} - \lambda_u \cos\theta \ . \tag{36}$$

In the case of small amplitude oscillations, $\beta \simeq 1 - \frac{1}{2\gamma^2} - \frac{K^2}{4\gamma^2}$ and $\cos\theta \simeq 1 - \frac{\theta^2}{2}$.

$$d \simeq \lambda_u \left(1 + \frac{1}{2\gamma^2} + \frac{K^2}{4\gamma^2} - (1 - \frac{\theta^2}{2})\right) \simeq \frac{\lambda_u}{2\gamma^2}\left(1 + \frac{K^2}{2} + \gamma^2\theta^2\right) \ . \tag{37}$$

When this distance d is an integer number of wavelength $n\lambda$, then the interferences are constructive. For the case $n = 1$, one can write:

$$\lambda_1 = \frac{\lambda_u}{2\gamma^2}\left(1 + \frac{K^2}{2} + \gamma^2\theta^2\right) \underset{K\ll 1}{\simeq} \frac{\lambda_u}{2\gamma^2}\left(1 + \gamma^2\theta^2\right) \ . \tag{38}$$

The wavelength emitted in the direction $\theta = 0$ is called the 'fundamental wavelength' and is written $\lambda_1(\theta = 0) = \frac{\lambda_u}{2\gamma^2}$. In the case of small oscillations, by differentiating the trajectory Eq. (34) with respect to $x \simeq ct$, one obtains the coordinates of $\vec{n}$ and $\vec{\beta}$ [16], with the notations of Fig. 12:

$$\vec{n} \simeq (\sin\theta\cos\varphi, \sin\theta\sin\varphi, \cos\theta) \quad \text{and} \quad \vec{\beta} \simeq (-\frac{\beta K}{\gamma}\sin(k_u x), 0, 0) \ . \tag{39}$$

The electric field emitted by a particle crossing the undulator is written then by deferring in Eq. (13) the expressions of the vectors $\vec{n}$ and $\vec{\beta}$ with $\theta \ll 1$:

$$\begin{aligned} E_\sigma(t) &= \frac{4r_0 cB_0\gamma^3}{r}\frac{(1-\gamma^2\theta^2\ \cos(2\varphi))}{(1+\gamma^2\theta^2)^3}\cos(k_u ct') \\ E_\pi(t) &= \frac{4r_0 cB_0\gamma^5}{r}\frac{\theta^2\ \sin(2\varphi)}{(1+\gamma^2\theta^2)^3}\cos(k_u ct') \end{aligned} \tag{40}$$

where r_0 is the proton classical radius.

Again, by using the Fourier transform, it is possible to write the angular spectral energy density emitted in an undulator observed in the direction (θ, φ) [16] (with $\theta^2 = \phi^2 + \psi^2$ and $\varphi = \text{Arctan}\ \frac{\psi}{\phi}$) (Fig. 12):

$$\begin{aligned} \frac{d^2W_\sigma}{d\Omega d\omega} &= \frac{r_0 e^2 B_0^2 N_u \lambda_u \gamma^4}{\pi m_0}\frac{(1-\gamma^2\theta^2\cos(2\varphi))^2}{(1+\gamma^2\theta^2)^5}\frac{N_u}{\omega_1}\left(\frac{\sin\left(\frac{(\omega-\omega_1)\pi N_u}{\omega_1}\right)}{\frac{(\omega-\omega_1)\pi N_u}{\omega_1}} + \frac{\sin\left(\frac{(\omega+\omega_1)\pi N_u}{\omega_1}\right)}{\frac{(\omega+\omega_1)\pi N_u}{\omega_1}}\right)^2 \\ \frac{d^2W_\pi}{d\Omega d\omega} &= \frac{r_0 e^2 B_0^2 N_u \lambda_u \gamma^4}{\pi m_0}\frac{(\gamma^2\theta^2\sin(2\varphi))^2}{(1+\gamma^2\theta^2)^5}\frac{N_u}{\omega_1}\left(\frac{\sin\left(\frac{(\omega-\omega_1)\pi N_u}{\omega_1}\right)}{\frac{(\omega-\omega_1)\pi N_u}{\omega_1}} + \frac{\sin\left(\frac{(\omega+\omega_1)\pi N_u}{\omega_1}\right)}{\frac{(\omega+\omega_1)\pi N_u}{\omega_1}}\right)^2 \end{aligned} \tag{41}$$

where N_u is the number of periods of the undulator and $\omega_1 = 2\pi c/\lambda_1 = 4\pi\gamma^2 c/(\lambda_u(1+\gamma^2\theta^2))$. For observation frequencies ω close to ω_1, $\frac{(\omega-\omega_1)\pi N_u}{\omega_1} \underset{\omega\simeq\omega_1}{\ll} \frac{(\omega+\omega_1)\pi N_u}{\omega_1}$ and the second term in the bracket is negligible compared to the first one. One can then use the simplified expression:

$$\begin{aligned} \frac{d^2W_\sigma}{d\Omega d\omega} &= \frac{r_0 e^2 B_0^2 N_u \lambda_u \gamma^4}{\pi m_0}\frac{(1-\gamma^2\theta^2\cos(2\varphi))^2}{(1+\gamma^2\theta^2)^5}\frac{N_u}{\omega_1}\left(\frac{\sin\left(\frac{(\omega-\omega_1)\pi N_u}{\omega_1}\right)}{\frac{(\omega-\omega_1)\pi N_u}{\omega_1}}\right)^2 \\ \frac{d^2W_\pi}{d\Omega d\omega} &= \frac{r_0 e^2 B_0^2 N_u \lambda_u \gamma^4}{\pi m_0}\frac{(\gamma^2\theta^2\sin(2\varphi))^2}{(1+\gamma^2\theta^2)^5}\frac{N_u}{\omega_1}\left(\frac{\sin\left(\frac{(\omega-\omega_1)\pi N_u}{\omega_1}\right)}{\frac{(\omega-\omega_1)\pi N_u}{\omega_1}}\right)^2 \ . \end{aligned} \tag{42}$$

On the other hand, when the observation frequency is far from ω_1, the terms are equivalent and the complete expression (41) should be used.

4.2 The low-frequency approximation

When the observation frequency ω and the total duration of the electric field impulse Δt are such that $\omega\Delta t$ is much lower than 1, it is possible to simplify the expression of the Fourier transform by taking a series expansion of the exponential.

$$e^{-i\omega t} = 1 - i\omega t - \frac{(\omega t)^2}{2} + i\frac{(\omega t)^3}{6} + ... + \frac{(-i\omega t)^n}{n!} + ... \ . \tag{43}$$

4.2.1 With order 0

By retaining only the first term of the development (43), it is possible to define a simple approximate model to represent in a satisfactory way the radiation received by an observer in the 'low-frequency'

mode [21]. With $e^{-i\omega t} \simeq 1$ and E taken null outside the time interval Δt, one can write:

$$\tilde{\vec{E}}(\phi,\psi,\omega) = \frac{1}{\sqrt{2\pi}}\int_{-\infty}^{+\infty}\vec{E}(\phi,\psi,t)e^{-i\omega t}dt \tag{44}$$

$$\underset{\omega\ll\omega_l}{\simeq} \frac{1}{\sqrt{2\pi}}\int_{\Delta t}\vec{E}(\phi,\psi,t)dt \tag{45}$$

where ω_l is the frequency limit for the model application, satisfying $\omega_l\Delta t = 1$.

It is often easier to perform the integration in particle time t'. Indeed, the expression of $\vec{E}(\phi,\psi,t')$ [Eq. (15)], and that of dt/dt' [Eq. (17)] are rational fractions of t'. This yields

$$\tilde{\vec{E}}(\phi,\psi,\omega) = \frac{1}{\sqrt{2\pi}}\int_{\Delta t}\vec{E}(\phi,\psi,t')\frac{dt}{dt'}dt' \ . \tag{46}$$

The integral over a limited interval is thus defined and an analytical expression of the Fourier transform can be obtained. As in the case of the undulator, one can define a deflection parameter of $K = \frac{\alpha\gamma}{2}$. One obtains then, in the case of a dipole of finite length $L = \alpha\rho$ [21], Appendix A:

$$\begin{aligned}
\tilde{E_\sigma}(\phi,\psi,\omega) &= \frac{q\gamma}{(2\pi)^{3/2}\epsilon_0 cr}\left[\frac{K-\gamma\phi}{1+\gamma^2\psi^2+(K-\gamma\phi)^2}+\frac{K+\gamma\phi}{1+\gamma^2\psi^2+(K+\gamma\phi)^2}\right] \\
\tilde{E_\pi}(\phi,\psi,\omega) &= \frac{q\gamma^2}{(2\pi)^{3/2}\epsilon_0 cr}\psi\left[\frac{1}{1+\gamma^2\psi^2+(K-\gamma\phi)^2}-\frac{1}{1+\gamma^2\psi^2+(K+\gamma\phi)^2}\right] \ .
\end{aligned} \tag{47}$$

The corresponding angular spectral energy density radiated is obtained by inserting these relations in Eq. (26):

$$\begin{aligned}
\frac{\partial^2 W_\sigma}{\partial\omega\partial\phi\partial\psi} &= \frac{q^2\gamma^2}{4\pi^3\epsilon_0 c}\left[\frac{K-\gamma\phi}{1+\gamma^2\psi^2+(K-\gamma\phi)^2}+\frac{K+\gamma\phi}{1+\gamma^2\psi^2+(K+\gamma\phi)^2}\right]^2 \\
\frac{\partial^2 W_\pi}{\partial\omega\partial\phi\partial\psi} &= \frac{q^2\gamma^4}{4\pi^3\epsilon_0 c}\psi^2\left[\frac{1}{1+\gamma^2\psi^2+(K-\gamma\phi)^2}-\frac{1}{1+\gamma^2\psi^2+(K+\gamma\phi)^2}\right]^2 \ .
\end{aligned} \tag{48}$$

Example 1: short dipole For a short dipole of length L and magnetic field B, the duration of the impulse Δt corresponds to the difference in travel time in the magnet between the proton and the photon, Appendix B:

$$\Delta t = \frac{L}{2\gamma^2 c}\left[1+\gamma^2(\phi^2+\psi^2)-\gamma^2\phi\alpha+\frac{\alpha^2\gamma^2}{3}\right] \tag{49}$$

where $\alpha = BL/B\rho$. The low-frequency limit is thus written:

$$\omega \ll \omega_l = \frac{2\gamma^2 c}{L\left[1+\gamma^2(\phi^2+\psi^2)-\gamma^2\phi\alpha+\frac{\alpha^2\gamma^2}{3}\right]} \ . \tag{50}$$

Prototype LHC dipoles have been designed and built [22]; these magnets have $L = 1$ m and $B = 6$ T, hence the typical values for the direction $(\phi,\psi) = (0,0)$ are $\omega_l = 2.6\times10^{16}$ rad.s^{-1} (or 16.8 eV) at 7 TeV and $\omega_l = 2.1\times10^{15}$ rad.s^{-1} (or 1.4 eV) at 450 GeV. The shape of the energy spectra is given in Fig. 14. In the low-frequency range, the spectral energy density becomes independent of the frequency. Thus, depending on the observation frequency bandwidth and the energy of the particles, the angular spectral energy density can have very different shapes for the same source.

The comparison between the derivation with Eq. (15) and the low-frequency model, Eq. (48), is presented in Fig. 15, for the observation range g3, showing that the model applies well at 7 TeV whereas it is at the limit of validity at 2 TeV.

This study shows that the spectral energy density emitted by a magnet of this type in the selected observation frequency range (e.g g3) can be represented by Eq. (48).

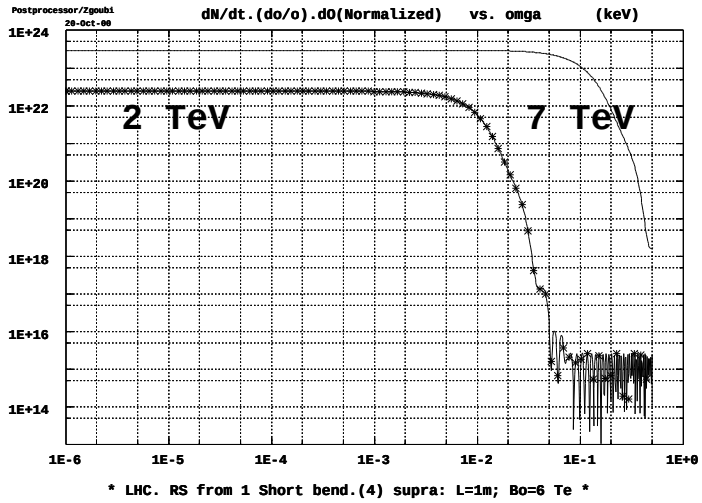

Fig. 14: Energy spectrum in the direction $(\phi, \psi) = (0, 0)$, for 7 TeV and 2 TeV in the case of a LHC prototype dipole with length 1 m and field $B = 6$ T.

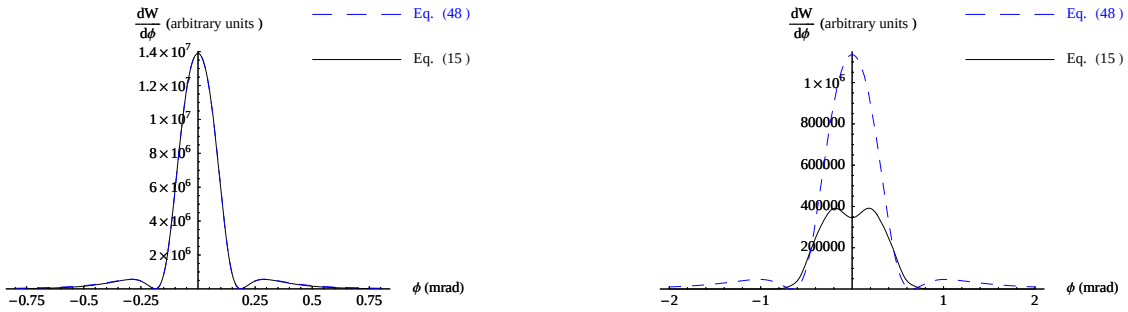

Fig. 15: Spectral energy density at $\psi = 0$ for 7 TeV (on the left) and 2 TeV (on the right) for $\omega = 1.71 \times 10^{15}$ rad.s^{-1}. The solid curve represents the calculation from Eq. (15) and the dotted curve is the low-frequency approximation based on Eq. (48).

Example 2: long dipole In the case of a long dipole with strong deflection ($K = \frac{\alpha\gamma}{2} \gg 1$), the angular spectral energy density of the σ component of the radiation in the direction $\psi = 0$ cancels for the angles ϕ beyond magnet edges directions because of the truncation of the electric field impulse in relation with the finite magnet length [21]. There are two peaks of energy density centred at $\pm 1/\gamma$ on both sides of the edges of the magnet (the maximum inside the core of the magnet and the relative maximum outside) (Fig. 16). The amplitude of each peak is obtained from Eq. (48) with $\psi = 0$ and:

$$\gamma\phi = \pm(K+1) \quad \text{for the largest peak} \tag{51}$$

$$\gamma\phi = \pm(K-1) \quad \text{for the smallest peak} \ . \tag{52}$$

One can thus compare the relationship between the amplitudes of the two peaks, from Eq. (48),

$$\frac{\partial^2 W_{\sigma,\text{low-peak}}}{\partial\omega\partial\Omega} \Big/ \frac{\partial^2 W_{\sigma,\text{high-peak}}}{\partial\omega\partial\Omega} \simeq \frac{\left(1-\frac{1}{K}\right)^2}{\left(1+\frac{1}{K}\right)^2} \tag{53}$$

with the one estimated from the plots of the numerical Fourier transform of Eq. (15), Figs. 16 and 17. Typically, the angular spectral energy density obtained in the case of a 9.45 m long dipole of the D2 type, Table 1, and a magnetic field of 2.65 T at 7 TeV ($K = 4$), observed at the frequency $\omega = 1.53 \times 10^{13}$ rad.s^{-1} (in this case, $\omega_l = 5.6 \times 10^{13}$ rad.s^{-1}) has the shape of Fig. 16. For the 7 TeV protons, in a D2 dipole, the ratio given by Eq. (53) is 0.36 and the measurement on the cuts obtained by numerical simulation from Eq. (15) (Fig. 16) gives 0.37. The agreement is thus very good, which justifies using the low-frequency model in these conditions.

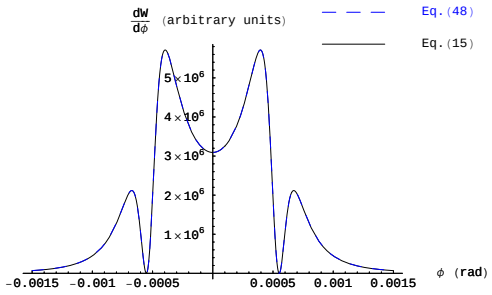

Fig. 16: Spectral angular energy density at $\psi = 0$ at 7 TeV in D2 (K = 4) for $\omega = 1.51 \times 10^{13}$ rad.s^{-1}

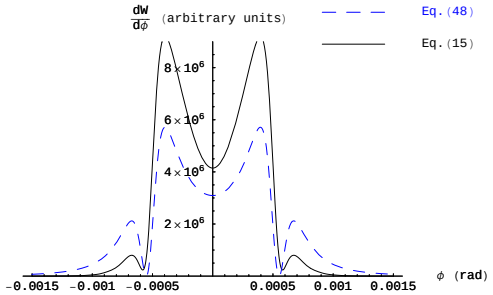

Fig. 17: Spectral angular energy density at $\psi = 0$ at 7 TeV in D2 (K = 4) for $\omega = 1.51 \times 10^{15}$ rad.s^{-1}

In the same way, the ratio of the amplitudes between the radiation emitted by a long dipole, equivalent to the radiation emitted by the centre of D2 (direction $\phi = 0$ on Fig. 16), and the maximum energy is written:

$$\frac{\partial^2 W_{\sigma,\text{long dipole}}}{\partial\omega\partial\Omega} \Big/ \frac{\partial^2 W_{\sigma,\text{high-peak}}}{\partial\omega\partial\Omega} = \frac{16}{(K)^2} \tag{54}$$

and is 0.56 here. An estimate from the plot of the numerical FT of Eq. (15) in Fig. 16 gives 0.52.

If the observation frequency is close to the limit frequency ω_l [Eq. (50)], as is the case for the diagnostics system, the model is no longer in such good agreement with the numerical simulation. Indeed, the position of the maximum remains identical, but the relative heights of the peaks and the centre no longer correspond to the calculation (Fig. 17).

4.2.2 With higher orders

When the approximation with order 0 is not sufficient, it is possible to take additional terms, in Eq. (43), in order to improve the model. The analytical calculation remains possible because the series expansion (43) transforms the function under the integral sign in Eq. (44) into a rational fraction. For the needs

of the following section, calculations up to order 2 were carried out. In this case, Eq. (44) is written:

$$\tilde{\vec{E}}(\phi,\psi,\omega) \underset{\omega\ll\omega_l}{\simeq} \frac{1}{\sqrt{2\pi}} \int_{\Delta t} \vec{E}(\phi,\psi,t)(1-i\omega t-(\omega t)^2/2)\,dt \ . \tag{55}$$

This results in calculating integrals of the form $\int E(t)t^n dt$ with $0 \leq n \leq 2$. By a change of variable from t to t', by using expressions (15) – (17), and by integrations by parts in cascade, one obtains the following results for the σ component, calculations detailed in Appendix A:

$$\int_0^{\frac{L}{c}} E_\sigma(\phi,\psi,t)dt = \frac{q\gamma^2}{2\pi\epsilon_0 cr}\left(\frac{\alpha-\phi}{1+\gamma^2\psi^2+\gamma^2(\alpha-\phi)^2}+\frac{\phi}{1+\gamma^2(\phi^2+\psi^2)}\right) \tag{56}$$

$$\int_0^{\frac{L}{c}} E_\sigma(\phi,\psi,t)\ t\ dt = \frac{q\gamma^2\alpha\rho}{4\pi\epsilon_0 c^2 r}\left[\left(\frac{1+\gamma^2(\phi^2+\psi^2)}{\gamma^2}-\alpha\phi+\frac{\alpha^2}{3}\right)\frac{\alpha-\phi}{1+\gamma^2((\alpha-\phi^2)+\psi^2)} + \frac{2\phi-\alpha}{2\gamma^2}\right] \tag{57}$$

$$\begin{aligned}\int_0^{\frac{L}{c}} E_\sigma(\phi,\psi,t)\ t^2\ dt = \\ &\frac{q\rho^2(1+\gamma^2(\phi^2+\psi^2))}{4\pi\epsilon_0 c^3 r\gamma^2}\left[\left(\frac{1+\gamma^2(\phi^2+\psi^2)}{2\gamma^2}-\alpha\phi\right)\frac{\gamma^2\alpha^2(\alpha-\phi)}{1+\gamma^2((\alpha-\phi)^2+\psi^2)}\right. \\ &-\alpha\left(\frac{1+\gamma^2(\psi^2-2\phi^2)}{\gamma^2}-\frac{3}{2}\alpha\phi\right)-\frac{2\phi(1+\gamma^2(\psi^2-\phi^2/2))}{\gamma^2}\ln\frac{1+\gamma^2((\alpha-\phi)^2+\psi^2)}{1+\gamma^2\phi^2+\gamma^2\psi^2} \\ &\left.+\frac{\sqrt{1+\gamma^2\psi^2}(1+\gamma^2(\psi^2-5\phi^2))}{\gamma^3}\left(\mathrm{Arctan}\frac{\gamma(\alpha-\phi)}{\sqrt{1+\gamma^2\psi^2}}+\mathrm{Arctan}\frac{\gamma\phi}{\sqrt{1+\gamma^2\psi^2}}\right)\right] \ .\end{aligned} \tag{58}$$

These formulas will be used for the representation of the interference between two dipoles in the next paragraph.

4.3 Interference between two sources

Any magnetic element of the machine is a potential source of synchrotron radiation. Along its trajectory, the particle thus crosses a succession of sources and the radiation emitted in each portion of the trajectory presents a certain degree of temporal coherence with the radiation emitted on other portions. Thus, according to the distances between the various sources, the principal directions of emission, and the particle energy, this can cause a phenomenon of interference which it is advisable to study in evaluating the intensity distribution received by the detector.

The formalism describing the phenomenon of interference between synchrotron radiation sources was developed in various cases for electrons [23] by using the low-frequency model. However, the application to the case of protons at high energy highlighted an additional limit to the application conditions of the low-frequency model to order 0 and required a development to higher orders.

4.3.1 Formalism

The crossing of a particle through two successive short dipoles (Fig.18) generates two coherent sources. The total emitted electric field is the sum of the electric fields emitted by the beam during the passage in each of the two magnetic elements:

$$E_{\text{tot}}(\phi,\psi,t) = E_1(\phi,\psi,t-T/2)+E_2(\phi,\psi,t+T/2) \ . \tag{59}$$

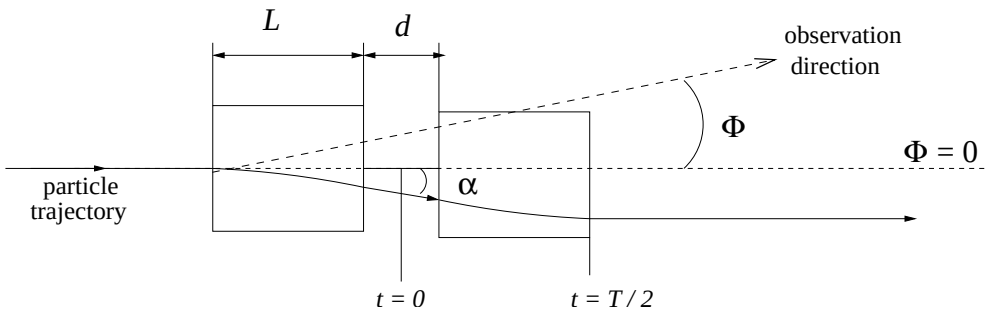

Fig. 18: Interference between two sources with opposite signs

where $E_1(\phi, \psi, t)$, ($E_2(\phi, \psi, t)$) represents the electric field emitted by the first, (second) magnet. The time T represents the time delay between the two impulses received by the observer.

The general expression of the Fourier transform is then written:

$$\tilde{E}_{\text{tot}}(\phi, \psi, \omega) = e^{-i\omega T/2}\tilde{E}_1(\phi, \psi, \omega) + e^{i\omega T/2}\tilde{E}_2(\phi, \psi, \omega) \tag{60}$$

with $\tilde{E}_{1,2}(\phi, \psi, \omega)$ the Fourier transform of $E_{1,2}(\phi, \psi, t)$.

This expression can have a simplified form in various particular cases treated later on, in particular if $E(t)$ is an odd function of T and in the low-frequency approximation.

4.3.2 Interference between two successive edges

Let us detail initially the case of interference between two successive edges of two identical dipoles separated by the distance d [23] (Fig. 19).

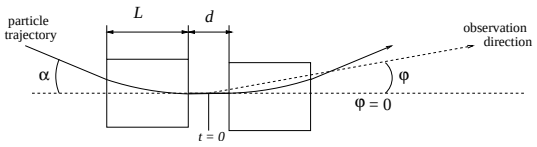

Fig. 19: Dipoles with interference between edges

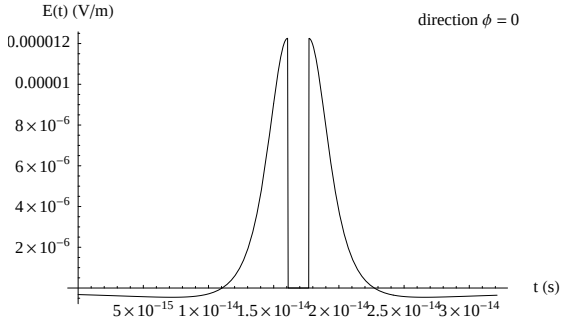

Fig. 20: Electric field emitted in the direction $\varphi = 0$ [Eq. (20)]

Since the edges are symmetrical, the electric field radiated in the $\phi = 0$ direction corresponding to that of the trajectory between the two magnets is an even and real function of t (Fig. 20), and $E_2(0, \psi, t) = E_1(0, \psi, -t)$. Equation (60) is then written:

$$\tilde{E}_{\text{tot}}(0, \psi, \omega) = e^{-i\omega T/2}\tilde{E}_1(0, \psi, \omega) + e^{i\omega T/2}\tilde{E}_1(0, \psi, -\omega) \ . \tag{61}$$

The radiated angular spectral density is proportional to the square module of the Fourier transform of $E_{\sigma,\text{tot}}(0, \psi, t)$ and is thus written:

$$\frac{\partial^3 W_{\sigma,\text{tot}}}{\partial\omega\partial\phi\partial\psi} = 2\epsilon_0 c r^2 \left(|\tilde{\vec{E}}_1(\omega)|^2 + |\tilde{\vec{E}}_1(-\omega)|^2 + 2\cos(\omega T)\tilde{\vec{E}}_1(\omega)\tilde{\vec{E}}_1(-\omega)\right) \tag{62}$$

where T is the travel time through the straight section d separating the two sources.

4.3.3 Interference between the edges of a long dipole

Let us now consider the complementary case to that presented in Fig. 19 from the point of view of the total magnetic field: the interference between the two edges of a single dipole (Fig. 21).

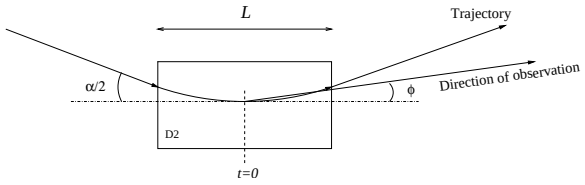

Fig. 21: Geometry considered for the interference between the edges of D2

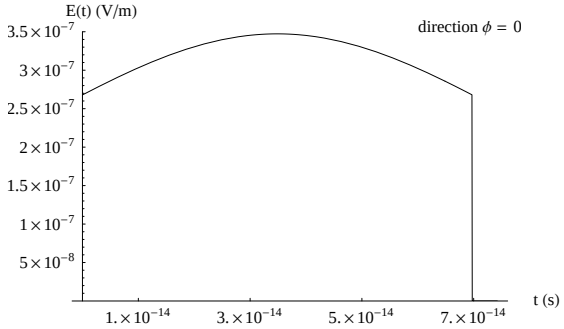

Fig. 22: Electric field emitted in the D2 dipole by a 450 GeV proton [Eq. (20)]

In the case of a weak magnet deflection ($\alpha < 1/\gamma$), the dipole behaves like a short magnet and the electric field is proportional to the magnetic field (Section 4.1.2). The total electric field emitted by the dipole in the $\phi = 0$ direction (Fig. 22) can thus be approximated by the difference of two step functions corresponding to the two edges with an almost constant part corresponding to the core of the magnet. The edges and the centre of the magnet emit in two different spectral domains: high frequency for the edges and low-frequency for the centre. In the high-frequency spectral domain corresponding to the edges, the radiation of the dipole is reduced to the interference between two sources (two edges) separated by the distance L, i.e. the magnet length. The angular spectral energy density is represented by Eq. (62), with $\tilde{\vec{E}}_1(\omega)$ representing the FT of the electric field produced by an edge.

By definition of a Heaviside function, in this case, $E_1(t)$ is odd [4] thus $\tilde{\vec{E}}_1(\omega) = -\tilde{\vec{E}}_1(-\omega)$ and Eq. (62) is simplified into:

$$\frac{\partial^3 W_{\sigma,\text{tot}}}{\partial\omega\partial\phi\partial\psi} = 4\sin^2\left(\omega\frac{T}{2}\right)\frac{\partial^3 W_{\sigma,1}}{\partial\omega\partial\phi\partial\psi} \tag{63}$$

where $\frac{\partial^3 W_{\sigma,1}}{\partial\omega\partial\phi\partial\psi}$ is the spectral angular energy density emitted by one edge.

In the particular case of the D2 dipole at 450 GeV, the angular deflection α is 1 mrad, whereas the angular opening of the cones of radiation is approximately $1/\gamma$ = 2 mrad. There is overlap in the emission direction and thus interference between the two edges (Figs. 23 and 24). The time T, calculated in Appendix B, is then the crossing time of the dipole, i.e. the length $L \simeq \rho\alpha$ of the arc (Fig. 21):

$$T = \frac{L}{2\gamma^2 c}(1 + K^2/3 + \gamma^2(\phi^2 + \psi^2)) \tag{64}$$

where $K = \alpha\gamma/2$. The term in $\sin^2(\omega T/2)$ in Eq. (63) describes a series of oscillations comparable with Newton's rings. The minima are given by $T = n\frac{2\pi}{\omega}$, i.e.:

$$n\lambda = \frac{L}{2\gamma^2}(1 + K^2/3 + \gamma^2(\phi^2 + \psi^2)) \ . \tag{65}$$

To check the relevance of the model, a cut in the $\phi = 0$ plane of the spectral energy density for a given frequency is plotted, Fig. 24. The solving of Eq. (65) in the ψ variable for a chosen wavelength gives the position of the various minima (ψ according to n), to be compared with the cut in the $\phi = 0$ plane of the spectral energy density (Fig. 24). The agreement obtained in the case of D2 at 450 GeV (K = 0.25), for $\omega = 9.1 \times 10^{14}$ rad.s^{-1} (that is to say $\hbar\omega/q$ = 0.6 eV) is very good (Table 3). The last

[4] If we except a constant component of offset which, in FT, gives a Dirac peak located at the origin and so outside the observation domain.

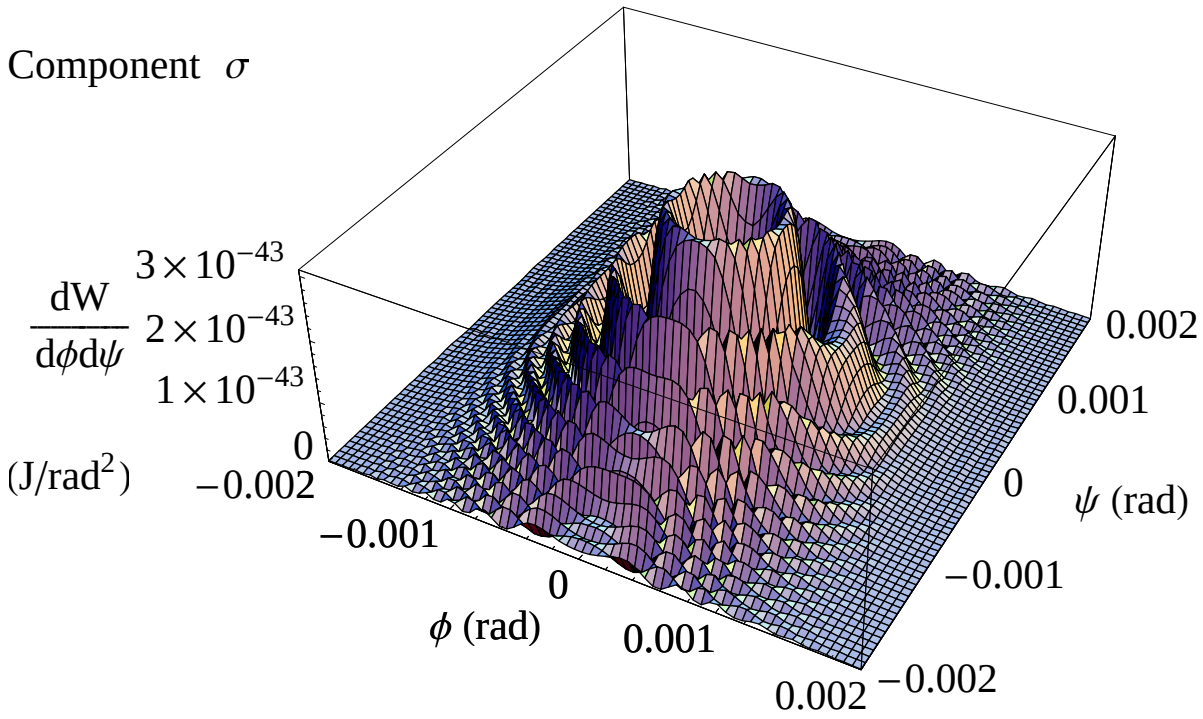

Fig. 23: Density of energy emitted by the whole of D2 (component σ) by a 450 GeV proton for $\omega = 9.1 \times 10^{14}$ rad.s^{-1}.

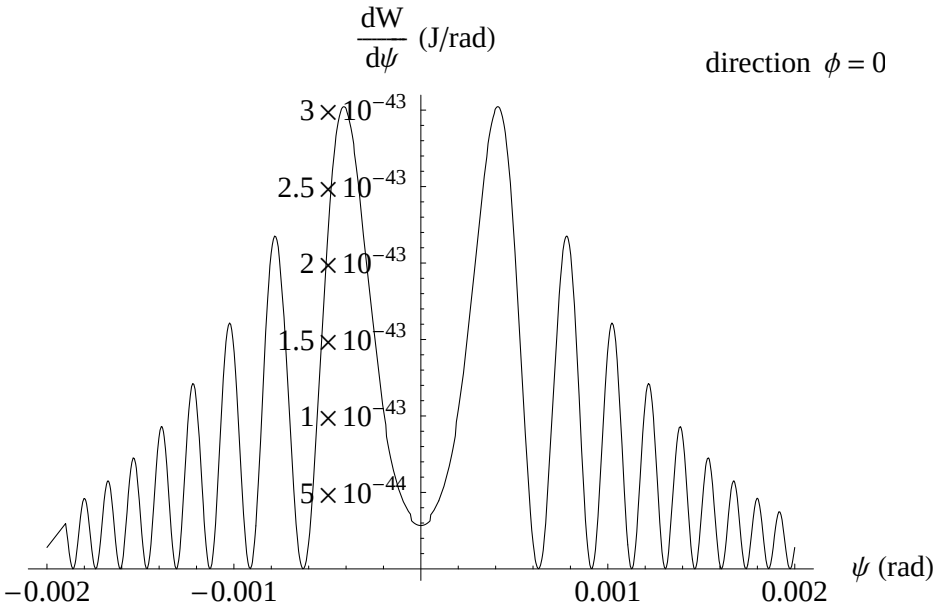

Fig. 24: Cut in the $\phi = 0$ plane of the angular spectral energy density radiated by the D2 dipole for $\omega = 9.1 \times 10^{14}$ rad.s^{-1}, i.e. $\lambda = 2$ μm, at 450 GeV.

Table 3: Comparison of the angular positions of the minima of a high order given by the numerical simulation, calculation with the term in K and without the term in K of the Eq. (64)

n value	11	12	13	14	15
$\psi_{\text{calculated}}$ (mrad)	0.608	0.904	1.116	1.297	1.456
$\psi_{\text{numerical}}$ (mrad)	0.620	0.910	1.120	1.310	1.450
$\psi_{\text{calculated}}$ with $K = 0$	0.682	0.950	1.158	1.333	1.488

line of the table highlights the considerable effect of $K \neq 0$ (representing the curvature of the trajectory between the two 'sources' materialized at the dipole edges) on the angular opening of the first rings, by contrast with two sources laid out on both sides of a section without field (such that K = 0) (Fig. 19).

4.3.4 Application in the case of the low-frequency model

Section 4.2.1 shows that the low-frequency model can be applied to the case of a short 1 m long dipole with $B = 6$ T and 7 TeV protons observed for ω in the g1 range. The electric field emitted by a dipole is thus written with Eq. (48).

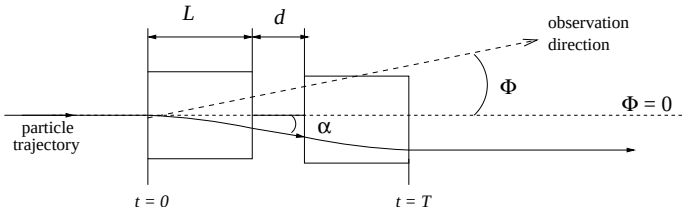

Fig. 25: Interference between two sources

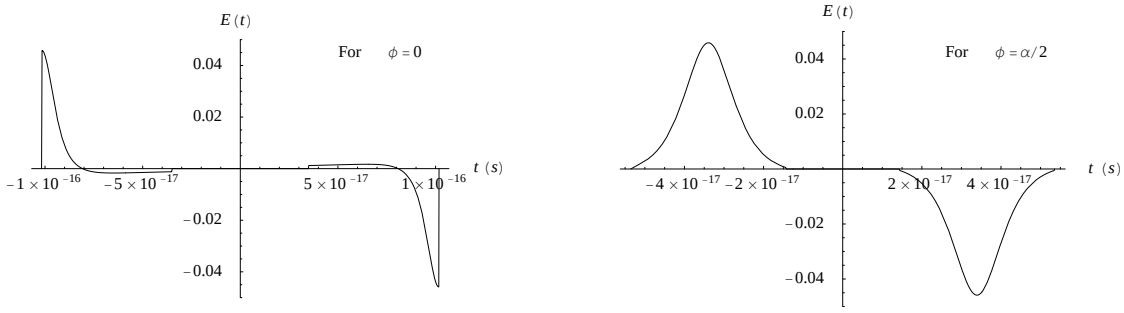

Fig. 26: Impulses of electric field received by the observer looking at the entrance edge of the first magnet (on the left) or the inside of the magnet (on the right)

In the case of two magnets with opposite magnetic fields, separated by the distance d (Fig. 25), the total emitted electric field, represented in Fig. 26, is the sum of the two fields emitted by each dipole. Moreover the anti-symmetry of the magnetic configuration makes it possible to write $E_2(\phi, \psi, t) = -E_1(\phi, \psi, -t + T)$. The time T corresponds to the travel time through the whole of the two dipoles of length L and the straight section d, Appendix B:

$$T = \frac{\alpha\rho}{\gamma^2 c}\left[1 + \gamma^2(\phi^2 + \psi^2) - \gamma^2\phi\alpha + \frac{\alpha^2\gamma^2}{3}\right] + \frac{d}{2\gamma^2 c}\left[1 + \gamma^2((\phi - \alpha)^2 + \psi^2)\right] \qquad (66)$$

where d is the distance between the two magnets (Fig. 25). The apparent position of the maximum of the pulse varies when the observer moves in the deflection plane of the magnets (Fig. 26); this is why the coherence time depends on the coordinates (ϕ, ψ).

Equation (60) is written in this case:

$$\tilde{E}_{\text{tot}}(\phi,\psi,\omega) = e^{i\omega T/2}\tilde{E}_1(\phi,\psi,\omega) - e^{-i\omega T/2}\tilde{E}_1(\phi,\psi,-\omega) \tag{67}$$

where $E_1(\phi,\psi,\omega)$ is the field emitted by the first dipole, described by Eq. (47). In the low-frequency approximation, the electric field is independent of ω, therefore $\tilde{E}_1(\phi,\psi,\omega) = \tilde{E}_1(\phi,\psi,-\omega)$ and Eq. (67) becomes $\tilde{E}_{\text{tot}}(\phi,\psi,\omega) = (e^{i\omega T/2} - e^{-i\omega T/2})\tilde{E}_1(\phi,\psi,\omega)$. The angular spectral energy density is written again with Eq. (63). Nevertheless, Fig. 27 shows that the agreement between this model and the numerical simulation is not very good.

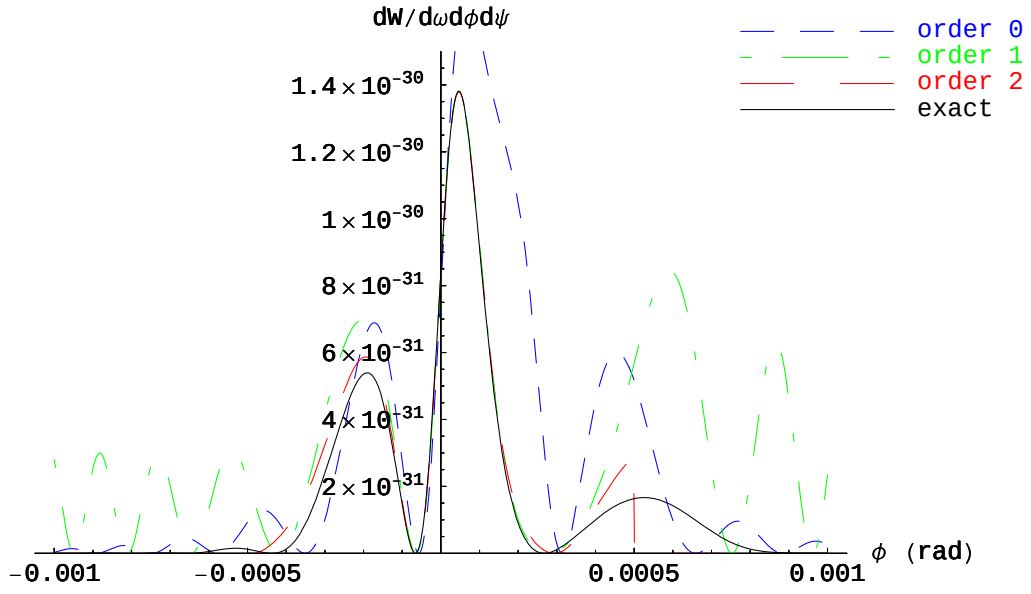

Fig. 27: Comparison between the various orders of development: exact calculation in black solid line, order 0 in dotted lines, order 1 in dashed and dotted lines, and order 2 in dashed.

Indeed, when writting the expressions of the Fourier transforms with the integrals, Eq. (60) is rewritten:

$$\tilde{E}_{\text{tot}}(\phi,\psi,\omega) = \frac{-2i}{\sqrt{2\pi}}\left[\cos\omega T/2\int_{-\infty}^{\infty} E_1(\phi,\psi,t)\sin\omega t\,dt - \sin\omega T/2\int_{-\infty}^{\infty} E_1(\phi,\psi,t)\cos\omega t\,dt\right] \tag{68}$$

where $E_1(\phi,\psi,t)$ is the field emitted by the first dipole, described by Eq. (48). The low-frequency approximation with order 0 is equivalent to neglecting the first term of the square bracket compared to the second:

$$\tilde{E}_{\text{tot}}(\phi,\psi,\omega) \underset{\omega t\ll 1}{\simeq} \frac{2i}{\sqrt{2\pi}}\left[\sin\omega T/2\int_{-\infty}^{\infty} E_1(\phi,\psi,t)dt\right] \tag{69}$$

However, in the particular case of the two 1 m long magnets with $d = 0.5$ m, these two terms are comparable to the first order (Figs. 28 and 29).

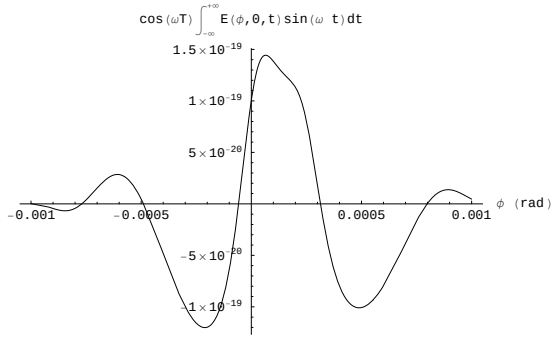

Fig. 28: $\cos(\omega T) \int_{-\infty}^{+\infty} E(\phi, 0, t) \sin \omega t$

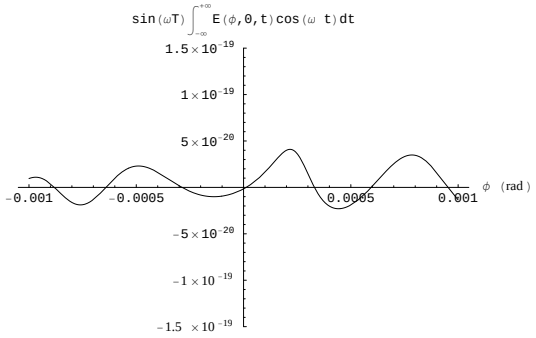

Fig. 29: $\sin(\omega T) \int_{-\infty}^{+\infty} E(\phi, 0, t) \cos \omega t$

To take this effect into account, one thus needs a development to higher orders of Eq. (68):

$$\tilde{E}_{\text{tot}}(\phi, \psi, \omega) = \frac{-2i}{\sqrt{2\pi}} \cos \omega T/2 \int_{-\infty}^{\infty} E_1(\phi, \psi, t)(\omega t) dt + \frac{2i}{\sqrt{2\pi}} \sin \omega T/2 \int_{-\infty}^{\infty} E_1(\phi, \psi, t)(1 - (\omega t)^2/2) dt \ . \quad (70)$$

The difference between the two terms can be calculated at various orders of development by using the derivations of integral carried out in Section 4.2.2 [Eqs. (56)–(58)]. The comparison with an exact numerical calculation (Fig. 27) shows that it is necessary to go at least up to order 2 to have satisfactory results within the radiation cone in the case of interference between two dipoles.

4.4 Conclusions

We tried to show in this section that there is a set of analytical tools that allow to evaluate in a more or less precise way the angular spectral energy densities produced by several types of sources or by various source configurations. However, a more systematic study of the possible sources for the diagnostics requires the use of numerical methods.

5 IMPLEMENTATION OF NUMERICAL CALCULATIONS

The analytical tools presented in the preceding section make it possible to calculate the angular spectral energy density emitted by a particle, but only in particular cases or with approximations limiting the real applications. For more complex magnetic configurations where the models cannot be used, the emitted electric fields must then be evaluated numerically. The Zgoubi program, used for this purpose, under development since the beginning of the 1970s [24] and already used for the LEP miniwiggler [25, 26, 27], is based on the calculation of charged-particle trajectories in magnetic fields to obtain the emitted synchrotron radiation. To check the correct operation of the numerical method used in the particular case of the sources studied for the LHC monitor, a test against the analytical models was carried out.

First of all, this section presents how the code works and the various conditions of use. The second part describes a procedure added to the code to allow the calculation of the synchrotron radiation emitted in an undulator. Finally, the various comparisons between analytical models and equivalent numerical simulations carried out are summarized to allow concluding on the reliability of the method.

5.1 Computer codes employed

The Zgoubi code is based on a step-by-step calculation of the particles' trajectories in an arbitrary magnetic field. The trajectory computation provides the speed and acceleration components needed for the derivation of the radiated electric field. Then, starting from the Fourier transform of this electric field

and from Eq. (26), it is possible to determine the synchrotron radiation characteristics. The calculation method is described in this part in relation to the particular application to the synchrotron radiation monitor.

5.1.1 Calculation of the trajectory

The numerical method is based on the step-by-step integration of the Lorentz equation:

$$m\frac{d\vec{v}}{dt} = q\vec{v} \times \vec{b} \tag{71}$$

where $\vec{b}$ is the magnetic field crossed by the particle and $\vec{v}$ the speed of the particle with $m = \gamma m_0$ the mass, and q the charge.

Starting from a position $\vec{R}(M_0)$ and a normalized speed $\vec{u}(M_0)$, defined by $\vec{u} = \vec{v}/v$, the position $\vec{R}(M_1)$ and the speed $\vec{u}(M_1)$ after a Δs displacement are obtained by a Taylor series truncated to the 6th order:

$$\begin{aligned}
\vec{R}(M_1) &\approx \vec{R}(M_0) + \vec{u}(M_0)\,\Delta s + \vec{u}\,'(M_0)\,\frac{\Delta s^2}{2!} + ... + \vec{u}^{(5)}(M_0)\,\frac{\Delta s^6}{6!} \\
\vec{u}(M_1) &\approx \vec{u}(M_0) + \vec{u}\,'(M_0)\,\Delta s + \vec{u}\,''(M_0)\,\frac{\Delta s^2}{2!} + ... + \vec{u}^{(5)}(M_0)\,\frac{\Delta s^5}{5!} \quad .
\end{aligned} \tag{72}$$

The values of the derivatives $\vec{u}^{(n)} = d^n\vec{u}/ds^n$ are calculated by starting from the differentiation of the Lorentz equation [Eq. (71)] with the definition $\vec{B} = \frac{\vec{b}}{B\rho}$:

$$\begin{aligned}
\vec{u}^{(2)} &= \vec{u}\,' \times \vec{B} + \vec{u} \times \vec{B}\,' \\
\vec{u}^{(3)} &= \vec{u}^{(2)} \times \vec{B} + 2\vec{u}\,' \times \vec{B}\,' + \vec{u} \times \vec{B}^{(2)} \\
\vec{u}^{(4)} &= \vec{u}^{(3)} \times \vec{B} + 3\vec{u}^{(2)} \times \vec{B}\,' + 3\vec{u}\,' \times \vec{B}^{(2)} + \vec{u} \times \vec{B}^{(3)} \\
\vec{u}^{(5)} &= \vec{u}^{(4)} \times \vec{B} + 4\vec{u}^{(3)} \times \vec{B}\,' + 6\vec{u}^{(2)} \times \vec{B}^{(2)} + 4\vec{u}\,' \times \vec{B}^{(3)} + \vec{u} \times \vec{B}^{(4)} \quad .
\end{aligned} \tag{73}$$

The nth derivative of $\vec{B}$ is obtained with different procedures according to the type of description of the magnetic field: field maps or analytical model. The detailed description of these various methods is given in Ref. [28]. For example, for a multipole with a 3D analytical model of the magnetic field, the three components of the field and their derivatives are calculated all along the trajectory starting from the analytical expression of the scalar potential. In the case of a field map, the derivatives are obtained by polynomial extrapolations up to more or less high orders [29].

From the initial conditions $\vec{B}(M_0)$, $\vec{u}(M_0)$ and Eqs. (73), it is possible to calculate successively the derivative of these conditions and by replacing them in Eq. (72) to deduce from them $\vec{R}(M_1)$ and $\vec{u}(M_1)$.

Starting from Eq. (71), Zgoubi thus provides $\vec{R}$, $\vec{v}$ and $\dot{\vec{v}}$ at any point of the trajectory in any magnetic field, determined by a field map or analytical models (short magnet, dipole, multipole, etc). The Zgoubi post-processor Zpop [28] then traces the trajectory in the studied magnetic field (Fig. 30) with the reference frame defined in Fig. 7.

5.1.2 Calculation of the electric field

Knowing the position, the speed, and the acceleration of the particle along the trajectory, Eq. (11) allows to calculate the radiated electric field in the 'far field approximation':

$$\vec{E}(t) = \frac{q}{4\pi\epsilon_0 c}\frac{\vec{n}(t') \times \left[(\vec{n}(t') - \vec{\beta}(t')) \times \dot{\vec{\beta}}(t')\right]}{r(t')(1 - \vec{n}(t') \cdot \vec{\beta}(t'))^3} \quad . \tag{74}$$

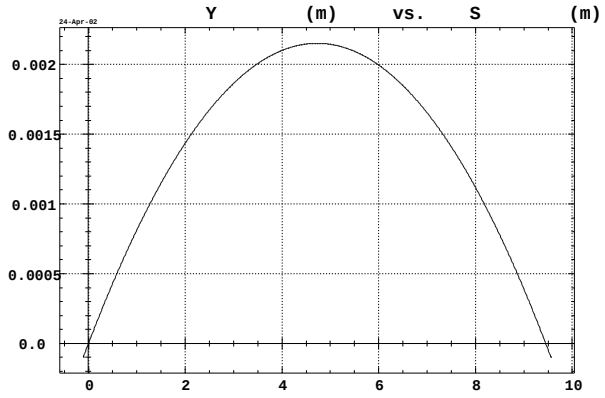

Fig. 30: Example of trajectory in a dipole of the D3 type for a 450 GeV proton

From the numerical point of view, the difficulty lies in evaluating the denominator term. Indeed, in the majority of the applications, the observation direction $\vec{n}$ is almost tangential to the trajectory, that is to say parallel to $\vec{\beta}$. Moreover, for particles with an energy higher than a few hundred times their rest mass, $\beta \simeq 1-1/2\gamma^2$ is very close to 1. With the computer's numerical precision, one thus often gets $\vec{n}-\vec{\beta} \simeq 0$ and $1-\vec{n}\cdot\vec{\beta} \simeq 0$, corresponding to a division by 0 in Eq. (74). The solution is the implementation of a calculation method of this scalar product explained in Ref. [25] using a fast converging series expansion of $\vec{\beta}$.

$$\begin{aligned} \vec{\beta} &= (\sqrt{\beta^2-\beta_y^2-\beta_z^2},\beta_y,\beta_z) \\ &= (\sqrt{1-1/\gamma^2-\beta_y^2-\beta_z^2},\beta_y,\beta_z) \\ &= (1-\underbrace{(a/2+a^2/8+a^3/16+...)}_{\xi_x},\beta_y,\beta_z) \end{aligned} \tag{75}$$

where $a = 1/\gamma^2+\beta_y^2+\beta_z^2$. On the other hand $\vec{n}$ is written:

$$\vec{n} = (\cos\psi\cos\phi, \cos\psi\sin\phi, \sin\psi) \tag{76}$$

$$= (1-\epsilon_x, n_y, n_z) \tag{77}$$

where $\epsilon_x = 2\,(\sin^2\phi/2+\sin^2\psi/2) - 4\sin^2\phi/2\sin^2\psi/2$.

By combining the two expressions (76) and (77), and by defining $\xi_x = a/2+a^2/8+a^3/16+...$, the two problematic expressions are written:

$$\begin{aligned} \vec{n}-\vec{\beta} &= (-\epsilon_x+\xi_x, n_y-\beta_y, n_z-\beta_z) \\ 1-\vec{n}\cdot\vec{\beta} &= \epsilon_x+\xi_x-\epsilon_x\xi_x-n_y\beta_y-n_z\beta_z \ . \end{aligned} \tag{78}$$

The ϕ and ψ angles being of order of $1/\gamma$, the n_y, n_z, β_y and β_z terms are of order of $1/\gamma$, ϵ_x is of order $1/\gamma^2$. Equations (78) can thus be computed with terms of the same orders allowing a numerical evaluation without the problem of precision. Moreover, the precision of the calculation is directly related to the order of development of the series $\xi_x = a/2+a^2/8+a^3/16+...$ which is quickly convergent. There is thus a good precision with very few terms, therefore a fast calculation.

Again, the Zgoubi post-processor plots the electric fields calculated with this method for any observation direction according to observer time or particle time. Figures 31 (a) and 31 (b) show an example for a dipole of the D3 type, with 7 TeV protons observed in the direction tangent to the dipole centre and in the direction of entry of the beam.

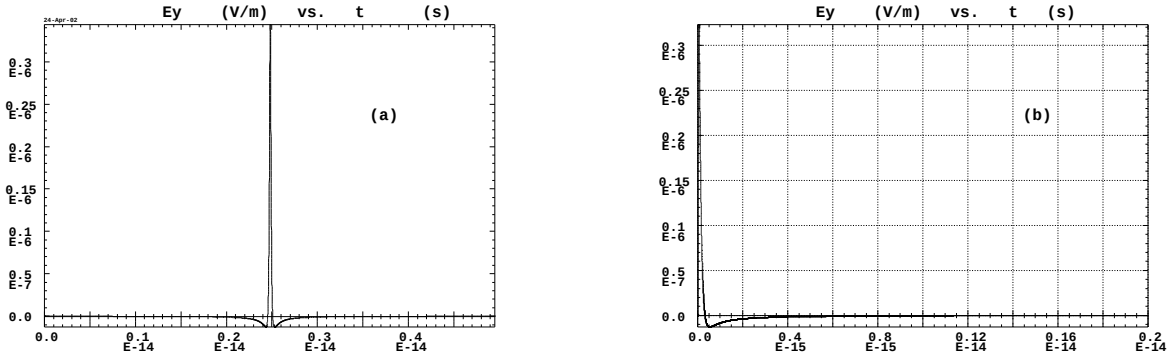

Fig. 31: Electric fields in the observer time frame simulated by Zgoubi, for a dipole of the D3 type and 7 TeV protons, observed in the direction tangent to the dipole centre (a), and in the direction $\gamma\phi = K$ of the magnet edge (b)

5.1.3 Calculation of the Fourier transform

From the electric field emitted by the particle and from Eq. (26), Zgoubi then calculates the Fourier transform of this field to finally obtain the angular spectral energy density received by the observer in a given position [Figs. 32 (a) and 32 (b)].

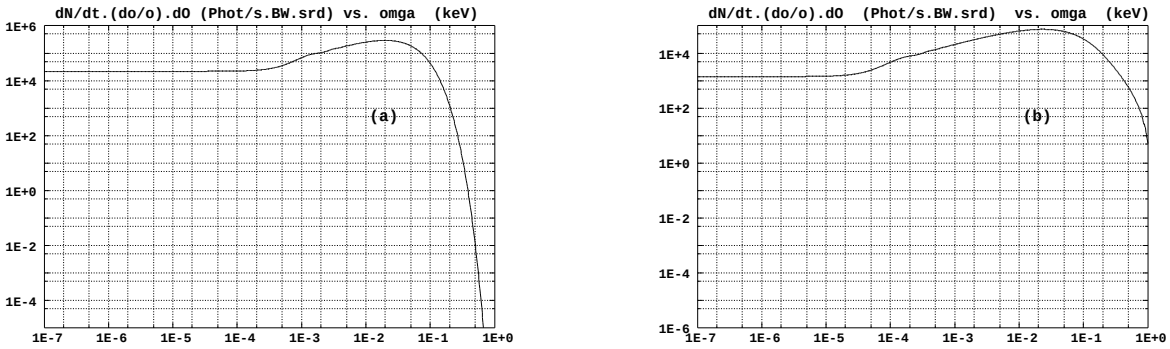

Fig. 32: Angular spectral energy density simulated by Zgoubi, for a dipole of the D3 type and 7 TeV protons, observed in the direction tangent to the dipole centre (a), and in the direction $\gamma\phi = K$ of the magnet edge (b)

The calculation of the Fourier transforms [25] is done without using the Fast Fourier Transform (FFT) algorithms, but by the direct integration of the electric field received during the time interval Δt, i.e. the crossing time of the elements defining the trajectory, $\frac{1}{2\pi}\int_{\Delta t} E(t)\exp(-i\omega t)dt$. The main reason is that the integration step in observer time is not constant. Indeed, the user chooses the constant spatial integration step Δs used for the trajectory derivation. The integration step in particle time $\Delta t' = \Delta s/\beta c$ is also constant, but the relation to obtain the integration step in observer time dt starting from dt' [Eq. (17], is a function of the variable term $1 - \vec{n}\cdot\vec{\beta}$ and of the integration step. In the area around the electric field peak, corresponding to the case $1 - \vec{n}\cdot\vec{\beta} \simeq 1/\gamma^2$ (Fig. 31), dt must be very small, i.e. several orders of magnitude smaller than the total duration of the impulse, for the precision of calculation. Again, because of the computer's precision, it cannot be determined by a difference between two times $t_n - t_{n-1}$, but starting from $1 - \vec{n}\cdot\vec{\beta}$ with the method previously described. This step is thus not constant and the number of steps is not necessarily a power of 2, which precludes using the standard FFT.

5.1.4 Space or frequency integration

From the angular spectral energy density $\frac{\partial^2 W}{\partial\Omega\partial\omega}$, as for the analytical calculation, while integrating either the frequency, or the solid angle, or both, the code calculates the energy received for a selected

wavelength range (chosen by the user in the form of a photon energy band in keV) and a given angular acceptance. Indeed, the Zgoubi post-processor allows the user to choose the location and dimensions of an integration window simulating a finite angular acceptance for the observation and on which one defines a grid. Zgoubi then carries out the calculation of the angular spectral energy density in each point of the grid and plots for each polarization component either the 3D view of the angular densities (Fig. 33), or the projections integrated in ν frequency, or angle ϕ or ψ [Figs. 34 (a) and 34 (b)]. The integration of one of these curves on a given interval provides the power received in an angular opening and a selected frequency range.

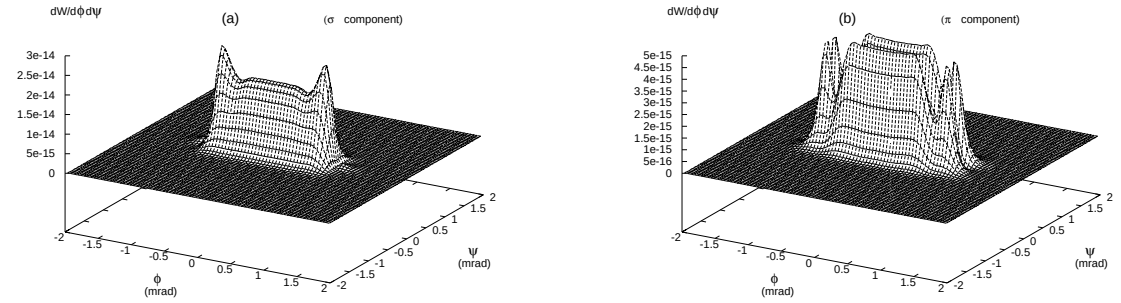

Fig. 33: Angular energy densities integrated over the g3 range simulated by Zgoubi, for a dipole of the D3 type and a 7 TeV proton, σ component (a) and π component (b).

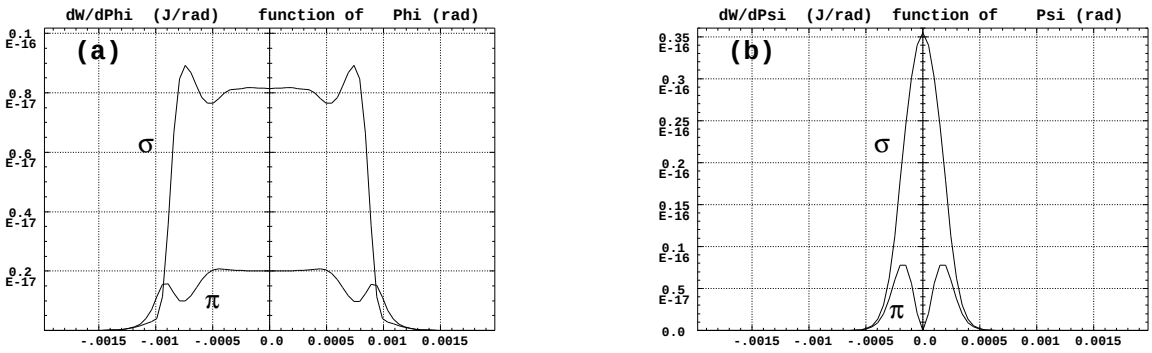

Fig. 34: Projections in the vertical plane $\psi = 0$ (a) and in the horizontal plane $\phi = 0$ (b) of the angular energy density integrated over the photon energy range 1.3–6.2 eV (corresponding to the g3 wavelength range) simulated by Zgoubi, for a dipole of the D3 type and a 7 TeV proton.

Zgoubi simulations can cover various numerical integrations where the user chooses the steps. The first integration relates to the calculation of the electric field impulse with a time sampling (or in longitudinal co-ordinate) and the second yields the Fourier transform of this field, with a frequency step. The choice of these steps results from a compromise between the computing time and the desired precision. It is thus necessary to carry out preliminary tests in order to optimize these two parameters.

5.2 Extension to the undulator radiation

The study of the various possible synchrotron radiation sources for the emittance measurement resulted in the development of a procedure that calculates the trajectory in an undulator magnetic field described in an analytical way by giving the element length, the number of periods, and its magnetic field peak [29]. The basic numerical method is that described in Section 5.1.1. The calculation procedure of the magnetic field, called by the code word UNDULATOR, uses truncated Taylor series, calculated using Maxwell's

equations [30]:

$$\begin{aligned} B_x(x,y,z) &= z\frac{\partial B}{\partial x} - \frac{z^3}{6}\left(\frac{\partial^3 B}{\partial x^3} + \frac{\partial^3 B}{\partial x \partial y^2}\right) \\ B_y(x,y,z) &= z\frac{\partial B}{\partial y} - \frac{z^3}{6}\left(\frac{\partial^3 B}{\partial x^2 \partial y} + \frac{\partial^3 B}{\partial y^3}\right) \\ B_z(x,y,z) &= B - \frac{z^2}{2}\left(\frac{\partial^2 B}{\partial x^2} + \frac{\partial^2 B}{\partial y^2}\right) + \frac{z^4}{24}\left(\frac{\partial^4 B}{\partial x^4} + 2\frac{\partial^4 B}{\partial x^2 \partial y^2} + \frac{\partial^4 B}{\partial y^4}\right) \end{aligned} \tag{79}$$

with x, y and z defined on Fig. 7. The procedure uses a 2D model with the mid-plane symmetry:

$$\begin{aligned} B_x(x,y,0) &= 0 \\ B_y(x,y,0) &= 0 \\ B_x(x,y,z) &= -B_x(x,y,-z) \\ B_y(x,y,z) &= -B_y(x,y,-z) \\ B_z(x,y,z) &= B_z(x,y,-z) \ . \end{aligned} \tag{80}$$

Equations (79) are then written:

$$\begin{aligned} B_x(x,y,z) &= z\frac{\partial B}{\partial x} - \frac{z^3}{6}\frac{\partial^3 B}{\partial x^3} \\ B_y(x,y,z) &\equiv 0 \\ B_z(x,y,z) &\equiv B - \frac{z^2}{2}\frac{\partial^2 B}{\partial x^2} + \frac{z^4}{24}\frac{\partial^4 B}{\partial x^4} \ . \end{aligned} \tag{81}$$

The magnetic field B and its derivative up to the fourth order are calculated starting from the analytical expression characterizing the sinusoidal field in an undulator:

$$B_z(x,y,0) = B_0 \sin\left(k_u x\right) \tag{82}$$

where $k_u = 2\pi/\lambda_u$ and $\lambda_u = L_u/N_u$ is the undulator magnetic period. In the current state, the procedure does not take into account the undulator fringe field[5].

5.3 Comparison between models and simulations

A first series of numerical simulations [31] was carried out in order to compare the results given by the Zgoubi code with those given by the analytical models [32] for three source types. In each case studied, small divergences appeared between the various results. Even if the order of magnitude is satisfactory for validating the computer code, in order to use it in more complex cases, it is advisable to understand the origin of these divergences. A systematic study was thus undertaken in order to insure the consistancy of the various computing techniques.

5.3.1 The LHC dipole case

The instantaneous energy (in J.s^{-1}) emitted by a particle is written [16]:

$$P_0 = \frac{2}{3}\frac{1}{4\pi\epsilon_o}\frac{e^2 c\gamma^4}{\rho^2} \ . \tag{83}$$

[5] A more precise 3D analytical model, derived from the 3D magnet simulations (see Appendix C), has now been implemented.

The synchrotron radiation is not emitted on the whole machine circumference. The power radiated by a particle on the complete circumference is obtained by multiplying the emitted energy by the relation between the emission time and the travelling time of a full machine turn:

$$P_0 \times \frac{2\pi\rho}{c} / \frac{2\pi R}{c} = P_0 \frac{\rho}{R} \tag{84}$$

where R is the average machine radius.

In the LHC case, the local curvature radius in a dipole and the average radius are different. Spectral power radiated by one particle per passage in the dipole is thus written:

$$\frac{dP}{d\omega} = \frac{\rho}{R} \frac{P_0}{\omega_c} \frac{9\sqrt{3}}{8\pi} \left(\frac{\omega}{\omega_c}\right) \int_{\omega/\omega_c}^{\infty} K_{5/3}\left(\frac{\omega}{\omega_c}\right) d\left(\frac{\omega}{\omega_c}\right) \tag{85}$$

where $K_{5/3}(\eta)$ is the modified Bessel function, and the total radiated power in a frequency band $[\omega_1, \omega_2]$ is written:

$$P_{[\omega_1,\omega_2]} = \frac{\rho}{R} \frac{P_0}{\omega_c} \frac{9\sqrt{3}}{8\pi} \int_{\omega_1}^{\omega_2} \left[\left(\frac{\omega}{\omega_c}\right) \int_{\omega/\omega_c}^{\infty} K_{5/3}\left(\frac{\omega}{\omega_c}\right) d\left(\frac{\omega}{\omega_c}\right) \right] d\omega \ . \tag{86}$$

Table 4 presents the comparison between the analytical results calculated starting from Eq. (86) with the *Mathematica* program and Zgoubi simulations. The agreement is very good for energies where the analytical model is applicable. Indeed, as will be shown in Section 6, below 2 TeV, the radiation emitted by the D2 dipole centre is negligible compared to that of the two edges and Eq. (86) cannot be used any more.

Table 4: Comparison between the numerical simulations of Zgoubi and the analytical model for a dipole of the D2 type

	Power		
Energy (TeV)	Eq. (86) (W)	Zgoubi (W)	Zgoubi /Eq. (86)
1.00	6.78×10^{-8}	3.30×10^{-7}	4.90
3.00	2.27×10^{-3}	2.28×10^{-3}	1.00
5.00	3.93×10^{-3}	4.02×10^{-3}	1.02
7.00	4.47×10^{-3}	4.60×10^{-3}	1.02

5.3.2 The short magnet case

To calculate the power radiated by a particle, one defines a vector $\vec{U}(t)$ [1] such as:

$$\frac{d^2P}{d\Omega dt} = \left|\vec{U}(t)\right|^2 \ . \tag{87}$$

The total energy radiated per unit solid angle is written then, according to Parseval's theorem:

$$\frac{dP}{d\Omega} = \int_{-\infty}^{+\infty} \left|\vec{U}(t)\right|^2 dt = \int_{-\infty}^{+\infty} \left|\tilde{\vec{U}}(\omega)\right|^2 d\omega \tag{88}$$

where $\tilde{\vec{U}}(\omega)$ is the Fourier transform of $\vec{U}(t)$ and

$$\frac{\partial P}{\partial\Omega\partial\omega} = \left|\tilde{\vec{U}}(\omega)\right|^2 \ . \tag{89}$$

The $\vec{U}(t)$ vector is thus proportional to $r\vec{E}(t)$ and is written:

$$\vec{U}(t) = C\gamma^3 B\vec{f}(\theta,\phi) \tag{90}$$

where $C = \frac{e^2}{\pi m}\left(\frac{1}{\epsilon_o c}\right)^{1/2}$, $\vec{f}$ is an angular factor, and $B = B(t)$ the magnetic field function at observer time t.

One limits the integration to the positive angular frequencies and the energy radiated per unit angle becomes:

$$\frac{dP}{d\Omega} = \int_0^{+\infty} \frac{\partial^2 P}{\partial\omega\partial\Omega} d\omega \tag{91}$$

where $\frac{\partial^2 P}{\partial\omega\partial\Omega}$ is the spectral angular energy density.

$$\frac{\partial^2 P}{\partial\omega\partial\Omega} = \left|\tilde{\vec{U}}(\omega)\right|^2 + \left|\tilde{\vec{U}}(-\omega)\right|^2 \tag{92}$$

and since in our case $\vec{U}(t)$ is real, one has:

$$\frac{\partial^2 P}{\partial\omega\partial\Omega} = 2\left|\tilde{\vec{U}}(\omega)\right|^2 \quad . \tag{93}$$

The radiated spectral power is then written:

$$\frac{\partial P}{\partial\omega\partial\Omega} = 2C^2\gamma^6 f^2 \tilde{B}(t)^2 \quad . \tag{94}$$

Finally, if one adds it in the formulas of Ref. [18], the power detected in the frequency band $[\nu_1, \nu_2]$ becomes[6]:

$$P_{sm} = \frac{\pi^3 C_1^2}{2c^2} B_0^2 L^2 N_p f_{rev} \int_{\nu_1}^{\nu_2} \left\{ \int_1^{\infty} \left(y^{-2} - 2y^{-3} + 2y^{-4}\right) e^{-xy} dy \right\} d\nu \quad . \tag{95}$$

Table 5 presents the comparison between the numerical results obtained with Zgoubi and the analytical calculations based on Eq. (95) in the case of a 0.15 m long dipole, with a Lorentzian magnetic field [32]:

$$B(z) = \frac{B_0}{1 + (z/L)^2} \tag{96}$$

where $B_0 = 1$ T. The agreement is very good in the validity domain of the model. By contrast, at high energy, the approximation supposing that the magnet deflection $\alpha = BL/B\rho$ is much lower than the radiation cone opening of $1/\gamma$ is no longer true: at 7 TeV, $\alpha\gamma$ = 0.5.

5.3.3 Undulator

The angular spectral energy density radiated by an undulator is given by Eq. (42). While integrating over the whole solid angle and all the frequencies, the total emitted energy is written [16]:

$$W = \frac{r_0 e^2 c^2 B_0^2 L_u \gamma^2}{3 m_0 c^2} \tag{97}$$

where $L_u = N_u \lambda_u$ is the overall undulator length.

[6] A missing factor of 2 has been re-established compared to earlier publication [32].

Table 5: Comparison between the analytical model of Eq. (95) and Zgoubi simulations for the short dipole ($L = 0.15$ m, B_0 = 1 T) for 10^{14} protons and the g3 frequency range

Energy (TeV)	Eq. (95) (W)	Zgoubi (W)	Zgoubi /Eq. (95)
0.45	8.52×10^{-9}	8.59×10^{-9}	1.01
0.55	5.26×10^{-8}	5.30×10^{-8}	1.01
0.60	1.00×10^{-7}	1.02×10^{-7}	1.02
0.70	2.64×10^{-7}	2.67×10^{-7}	1.01
0.90	8.74×10^{-7}	8.93×10^{-7}	1.02
1.00	1.29×10^{-6}	1.32×10^{-6}	1.02
3.00	8.82×10^{-6}	8.92×10^{-6}	1.01
5.00	1.15×10^{-5}	1.15×10^{-5}	1.00
6.00	1.22×10^{-5}	1.31×10^{-5}	1.07
7.00	1.27×10^{-6}	1.44×10^{-5}	1.13

The power emitted by a particle in the undulator is given by $P_u = Wc/L_u$ and the angular spectral power density can be written as:

$$\begin{aligned} \frac{d^2P_\sigma}{d\Omega d\omega} &= P_u\gamma^2\frac{3}{\pi}F_{u,\sigma}(\theta,\varphi)f_{Nu}(\omega-\omega_1) \\ \frac{d^2P_\pi}{d\Omega d\omega} &= P_u\gamma^2\frac{3}{\pi}F_{u,\pi}(\theta,\varphi)f_{N_u}(\omega-\omega_1) \end{aligned} \tag{98}$$

using the following definitions:

$$F_{u,\sigma}(\theta,\varphi) = \frac{(1-\gamma^2\theta^2\cos(2\varphi))^2}{(1+\gamma^2\theta^2)^5} \tag{99}$$

$$F_{u,\pi}(\theta,\varphi) = \frac{(\gamma^2\theta^2\sin(2\varphi))^2}{(1+\gamma^2\theta^2)^5} \tag{100}$$

$$f_{N_u}(\omega-\omega_1) = \frac{N_u}{\omega_1}\left(\frac{\sin\left(\frac{(\omega-\omega_1)\pi N_u)}{\omega_1}\right)}{\frac{(\omega-\omega_1\pi N_u)}{\omega_1}}\right)^2 . \tag{101}$$

For a large number of periods ($N_u \gg 1$), the integration of Eq. (98) over the whole solid angle gives the spectral power density [16]:

$$\begin{aligned} \frac{dP_{u\sigma}}{d\omega} &= \frac{3P_u}{\omega_{10}}\frac{\omega}{\omega_{10}}\left[\frac{1}{2}-\frac{\omega}{\omega_{10}}+\frac{3}{2}\left(\frac{\omega}{\omega_{10}}\right)^2\right] \\ \frac{dP_{u\pi}}{d\omega} &= \frac{3P_u}{\omega_{10}}\frac{\omega}{\omega_{10}}\left[\frac{1}{2}-\frac{\omega}{\omega_{10}}+\frac{1}{2}\left(\frac{\omega}{\omega_{10}}\right)^2\right] \end{aligned} \tag{102}$$

where $\omega_{10} = \omega_1(\theta = 0) = 4\pi\gamma^2 c/\lambda_u$ is the critical frequency in the undulator median plane.

The comparison of the spectral power density simulated with Zgoubi and calculated with Eq. (102) shows a perfect agreement (Fig. 35). The abrupt edge for the frequency $\omega = \omega_{10}$ given by analytical calculation for $N_u = \infty$ is softened in the numerical simulation because of the finite number of periods (N_u = 20).

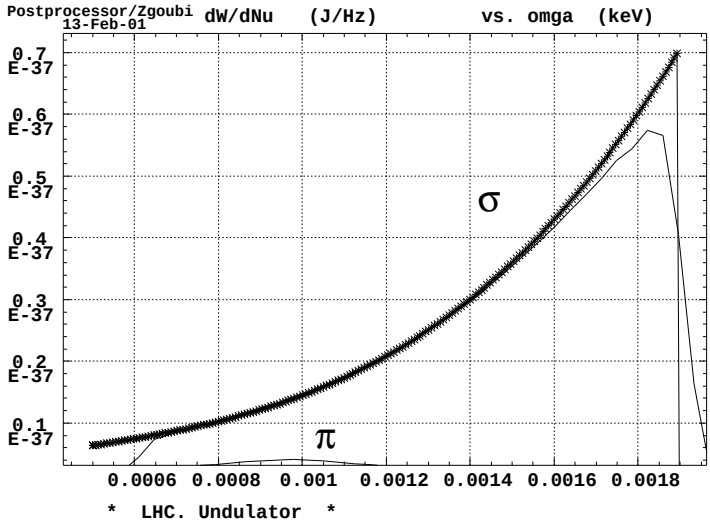

Fig. 35: Spectral energy density integrated over the whole solid angle simulated by Zgoubi (solid line) and calculated with the analytical model [Eq. (102)], (stars).

5.4 Conclusions

The numeric code Zgoubi was tested in particular cases allowing comparison with existing analytical models. The very good agreement from the qualitative as well as from the quantitative point of view validates the numerical methods.

For the choice of a synchrotron radiation source for the profile monitor, the preliminary study [32] carried out using the analytical models for a short magnet, a dipole, and the edge effect underlined the need to study other sources to cover the whole energy range of the proton energy. As the analytical models are not applicable to the majority of the configurations considered, the evaluation of the produced intensities presented in the following section was carried out by numerical simulations using the Zgoubi code.

6 SYNCHROTRON RADIATION SOURCES IN THE LHC

To obtain precise beam profile measurements, the first stage is to choose the best possible source in terms of flux collected by the telescope. This choice is guided not only by the absolute performance of the various sources, but also by the possibilities for the extraction of the produced light. In this section the studies carried out to check the usable sources and to estimate their performance under the prevailing conditions of the machine layout are described. The intensity emitted by a D2 type dipole, the main source considered initially, proved to be insufficient for the diagnostic at energies lower than 2 TeV. Four other sources were then studied to cover energies between 450 GeV and 2 TeV:

1. a set of four superconducting dipoles improperly called ‘miniwiggler’;
2. an alternative to this miniwiggler with a second extraction mirror dedicated to the diagnostic in bunch-by-bunch mode at 450 GeV;
3. an undulator at room temperature;
4. a superconducting undulator.

These various sources are first presented with their particular operating conditions. They are then compared in terms of collected intensity, and finally we give the choice of the source which is currently under development.

6.1 Intensities emitted by the different possible sources

6.1.1 The D2 dipole

A preliminary study [31, 32] showed that it was not possible to use the synchrotron radiation emitted by the superconducting main magnets (in particular because of space problems for the light extraction). On the other hand, the machine layout would make it possible to exploit the synchrotron radiation emitted by a D2 separation dipole near IP1 or IP5.

D2 is a 9.45 m long dipole with a maximum magnetic field of 2.65 T at 7 TeV. It follows the energy ramp in order to maintain a constant deflection angle α = 1.07 mrad, which gives a curvature radius ρ = 8829.5 m. Table 6 gives the evolution of the dipole SR critical frequency, defined as $\omega_c = \frac{3c\gamma^3}{2\rho}$, with energy.

Table 6: Characteristics of the radiation in D2 (centre and edge). Note that the critical frequency ω_c crosses the observation frequency range (g1 or g3) during the energy ramp for the centre of D2 whereas that of the edge always remains above the range.

	Dipole centre		Dipole edge	
Energy (TeV)	$\hbar\omega_c/q$ (eV)	ω_c (rad.s^{-1})	$\hbar\omega_{c,\text{short magnet}}/q$ (eV)	$\omega_{c,\text{short magnet}}$ (rad.s^{-1})
0.45	0.0037	5.64×10^{12}	5.2	7.90×10^{15}
0.75	0.0170	2.61×10^{13}	14.4	2.20×10^{16}
2.00	0.33	4.94×10^{14}	102.0	1.56×10^{17}
7.00	13.9	2.12×10^{16}	1256.0	1.90×10^{18}

The D2 characteristics are such that no simple analytical model can be used to calculate the light production over the whole energy range. Indeed, the deflection angle is α = 1.07 mrad whatever the beam energy, and at 450 GeV the average light cone opening is about $1/\gamma$ = 2.08 mrad. Consequently, the cones emitted by each of the two edges overlap[7] giving the interference pattern of Fig. 36. On the other hand, at 2 TeV, the average light cone opening is then $1/\gamma$ = 0.47 mrad. The light cones can then be distinguished (Fig. 37).

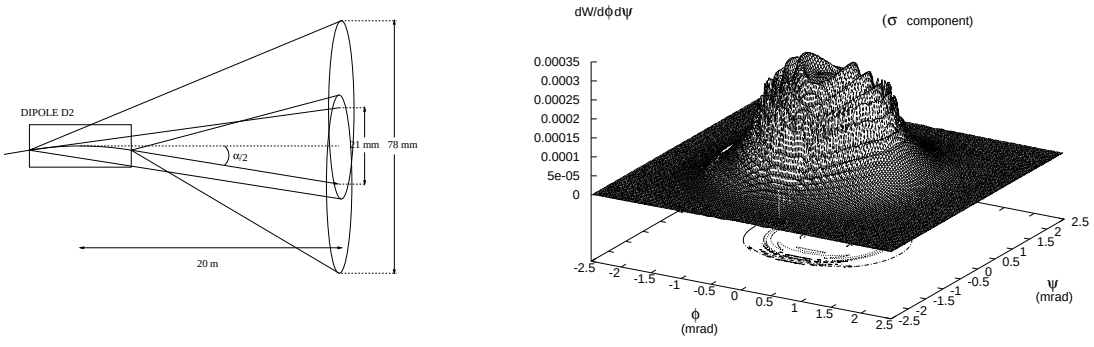

Fig. 36: Scheme of radiation of D2 for a proton of 450 GeV on the left and on the right, emitted angular energy density at 450 GeV (integrated on the g3 frequency range) by D2 (σ component), Zgoubi simulation.

[7]The diameter of the vacuum chamber of 56 mm allows the synchrotron radiation emitted by the entrance edge to exit on the other side without being intercepted.

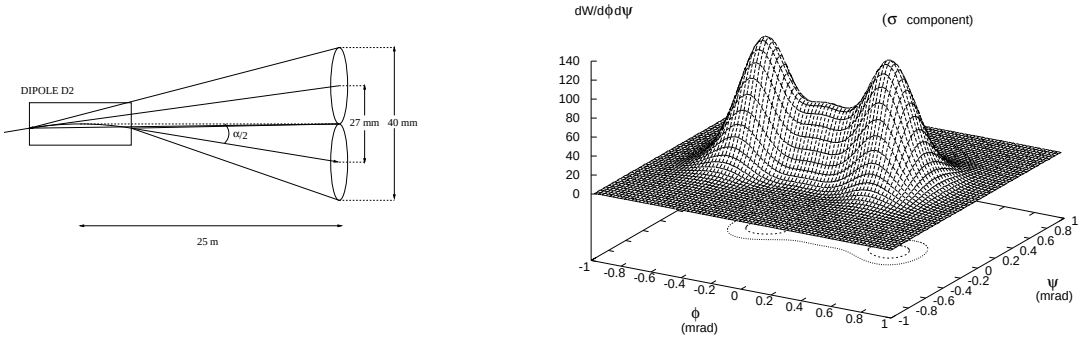

Fig. 37: Scheme of radiation of D2 for a proton of 2 TeV on the left and on the right, emitted angular energy density at 2 TeV (integrated on the g3 frequency range) by D2 (σ component), Zgoubi simulation.

At 450 GeV, the radiation emitted by the D2 dipole comes primarily from its two edges with an interference as described in Section 4.3.3, while at 7 TeV, taking into account the shrinking of the emitted light cone, the observation of the magnet centre becomes possible and the model of classical synchrotron radiation can be used. On the other hand, for intermediate energies, no simple model is at our disposal and it is necessary to use such numerical tools as the ray-tracing code Zgoubi.

The Zgoubi code calculates the total intensity emitted per turn in the D2 dipole for the selected frequency range (g3) and for the various energies of the ramp. The angular opening of the cone given in Table 7 corresponds in the vertical plane to the opening of the edge radiation, while in the horizontal plane, it also includes the angular deflection of the magnet (opening of the cone of each edge plus α).

Table 7: Total energy emitted in the D2 dipole, by one proton per LHC turn (90 ms) and power emitted by the nominal beam (10^{14} protons) in the g3 frequency range. The angular opening is here the angular width taken at 5% of the maximum intensity. In the horizontal plane, it includes the magnet deflection α.

Proton energy (TeV)	Emitted energy (J) 1 part. 1 turn	Emitted power (W) 10^{14} protons	Angular opening (mrad)	
			Horiz.	Vert.
0.45	9.7×10^{-28}	1.0×10^{-9}	4.2	4.6
1.00	2.7×10^{-25}	2.9×10^{-7}	2.4	2.6
2.00	4.4×10^{-23}	4.8×10^{-5}	1.8	1.1
7.00	4.2×10^{-21}	4.6×10^{-3}	1.5	0.8

Taking into account the weak angular deflection of D2, the imaging system intercepts the radiation coming from almost the whole magnet. To shorten the trajectory portion 'seen', in order to limit the depth of field effects, it is necessary to restrict the optics angular acceptance (Section 7.4.4). As in the LEP telescope [17], a slit placed in the focal plane of the telescope [33, 34] allows typical values of 0.25 mrad in the horizontal plane to be obtained, but it limits at the same time the entering light flux. To take account of this, the angular integration in the numerical simulation is thus limited to $\Delta\phi$ = 0.25 mrad in the trajectory plane. With a curvature radius of ρ = 8829.5 m, this angular acceptance limits the trajectory portion l that the observer 'sees' to $l = \rho\Delta\phi$ = 2.2 m, in reference to Fig. 9. So, according to the slit position in the horizontal plane, it is possible to select only a part of the dipole, either inside, or at an edge (Fig. 38).

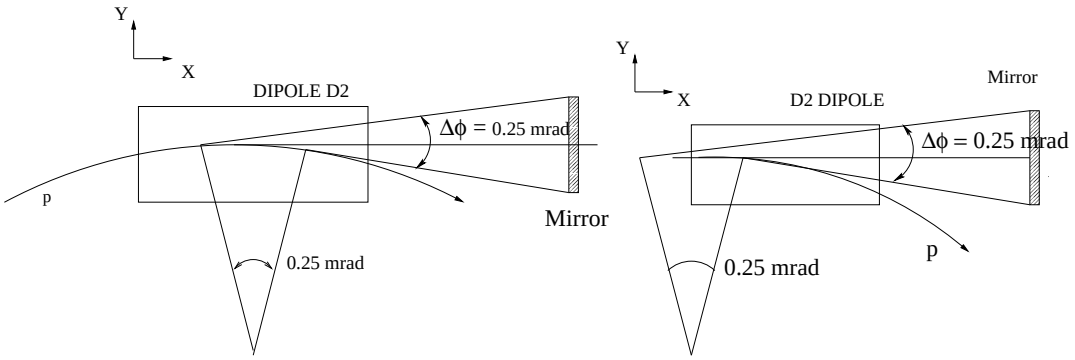

Fig. 38: Portion of trajectory intercepted by the mirror with an angular acceptance reduced to 0.25 mrad to simulate the action of a slit in the focal plane, aiming at the edge or the interior of the dipole.

The energies collected on the mirror for a proton are given in Table 8.

Table 8: Intensities collected by the detector if the angular acceptance is limited by a slit placed in the focal plane of the optical system, for g3

Proton energy (TeV)	Collected energy (for 1 proton)	
	D2 centre (J)	D2 edge (J)
0.45	2.3×10^{-28}	1.9×10^{-28}
1.00	1.1×10^{-26}	4.5×10^{-26}
2.00	4.6×10^{-24}	8.4×10^{-24}
7.00	9.0×10^{-22}	3.6×10^{-22}

Table 9 presents the results which will be demonstrated later (Table 28) and gives the minimal energies necessary to do the profile measurement according to the characteristics of the selected optical device.

Table 9: Minimal energies per proton necessary to allow the profile measurement with a 5% precision with a pilot bunch (5×10^9) or with a nominal bunch (10^{11}protons)

Proton energy (TeV)	Minimum energy per proton (J)			
	for 20 ms (225 turns)		turn-by-turn mode	
	5×10^9 p	10^{11} p	5×10^9 p	10^{11} p
0.45	2.9×10^{-22}	1.5×10^{-23}	1.3×10^{-24}	6.4×10^{-26}
7.00	7.5×10^{-23}	3.8×10^{-24}	3.3×10^{-25}	1.7×10^{-26}

Using this table, the results given in Table 8 show that the D2 dipole provides enough light to allow the beam transverse dimension measurement above 2 TeV, but for energies lower than 2 TeV, it is necessary to find another source. The various sources presented in the following were studied for use in this low-energy range.

6.1.2 Superconducting miniwiggler

In order to design the LHC main dipoles, shorter prototypes were tested. On the basis of the possibility of recovering the coils of these prototypes to reduce the cost of magnet construction, the implantation in IR4 of a superconducting miniwiggler composed of four strong magnetic field magnets was studied (Fig. 39). To avoid complicating the optical system by considering an alignment system following the

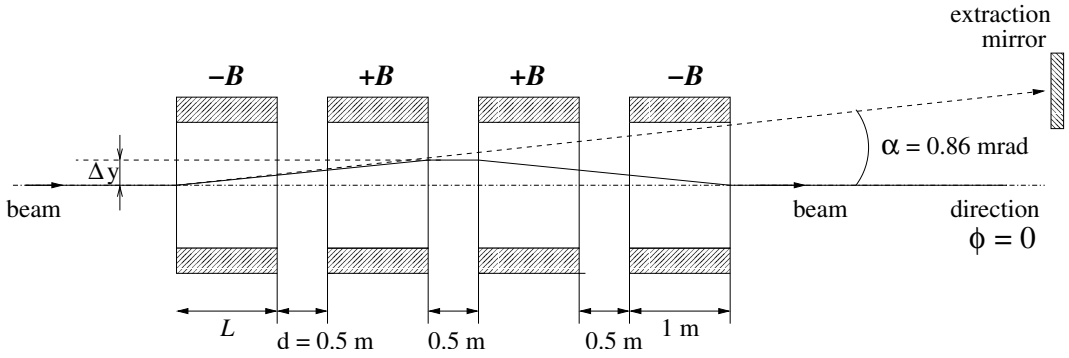

Fig. 39: Configuration of the superconducting miniwiggler with constant aiming direction

beam energy, it was decided to aim the optics at a fixed point of the particle trajectory, chosen as the beam direction at the exit of the first magnet. For that, it is necessary to operate with a constant magnet deflection by increasing the magnetic field proportionally to the proton momentum. The considered source must supplement the D2 dipole for the energy range going from 450 GeV up to 2 TeV. To maintain the constant and maximum deflection over this interval, it is thus necessary to reach the maximum magnetic field at 2 TeV. The test 1 m long dipole prototypes can reach a magnetic field of 6 T, i.e. a deflection α = 0.86 mrad at 2 TeV.

The insertion of a single magnet in the straight section causes a closed orbit bump, which must be closed again locally to avoid its propagation in the machine. The angular deflection obtained in this configuration does not permit to extract the light produced by a single magnet and to close the bump downstream from the extraction mirror in the distance reserved for the device. It is thus necessary to deviate the particle beam after the light source in order to be able to place the extraction mirror at the imposed safety distance of 15σ. The adopted solution would be to place four magnets in a magnetic field configuration $-B$, B, B, $-B$ (Fig. 39).

The spectral densities obtained with the four magnets are given in Fig. 40.

At 450 GeV [Fig. 40 (a)] At injection energy, taking into account the large angular opening of the radiation cone (about $1/\gamma$ = 2 mrad), the magnet deflection is not sufficient to separate angularly the radiation emitted by the first two magnets (in the $\phi = \alpha/2$ direction), and that by the last two (in the $\phi = -\alpha/2$ direction). There is thus partial angular overlap of the light angular spectral densities, and the maximum intensity is emitted in the particle beam direction ($\phi = 0$ on Fig. 40). The mirror whose edge is at 15σ thus intercepts only a fraction of the total emitted intensity, approximately 25%.

At 2 TeV [Fig. 40 (b)] The radiation cone opening is reduced to $1/\gamma \simeq 0.5$ mrad. The two groups of magnets emit respectively in $\phi = \pm\alpha/2 = \pm 0.43$ mrad. There is thus sufficient angular separation between the two radiation cones so that there is overlap only in the low-intensity zone and the produced interferences are not noticeable: the maximum intensity is thus not emitted in the particle beam direction and it is possible to intercept a significant portion of the radiation produced by the first two dipoles.

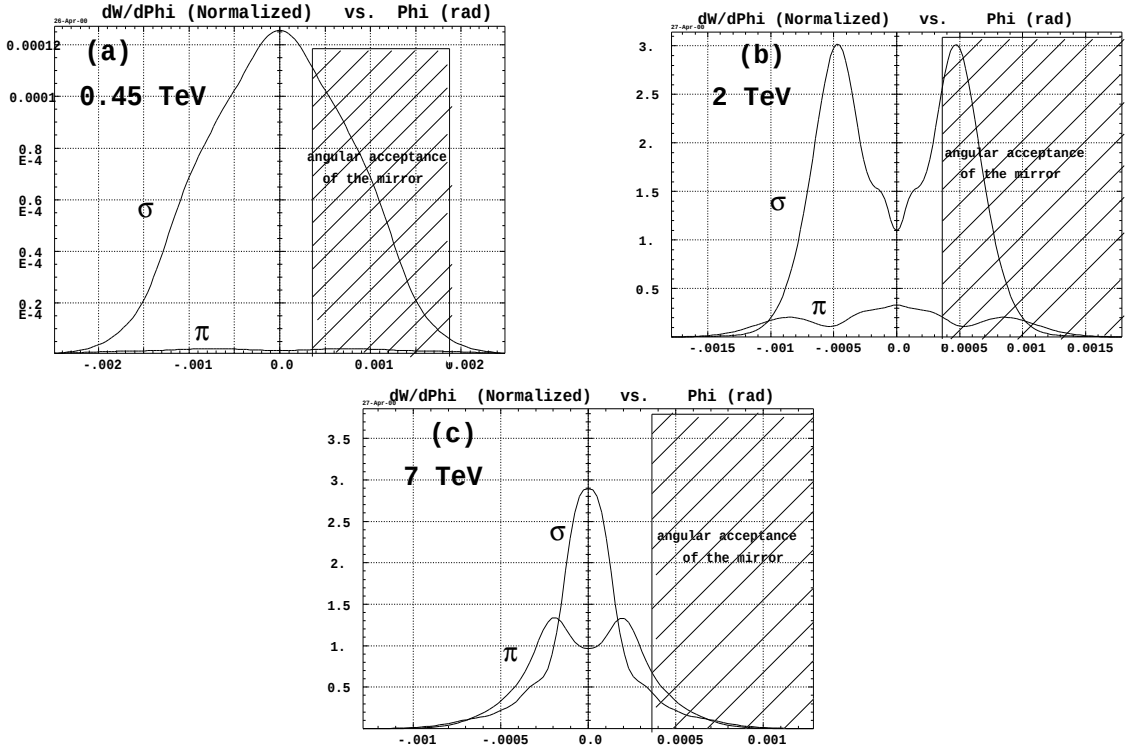

Fig. 40: Projection in the horizontal plane ($\psi = 0$) of the spectral energy densities emitted by four magnets at 450 GeV (a), 2 TeV (b) and 7 TeV (c), integrated over the wavelength range 350–1100 nm. The direction ϕ = 0 corresponds to the proton beam exit direction. The two curves on each figure correspond to the horizontal component (σ) and the vertical component (π).

At 7 TeV [Fig. 40 (c)] At high energy, the magnet deflection is 0.26 mrad and the principal emission direction is $\phi = \alpha/2$ = 0.13 mrad. The angular opening of the radiation being about $1/\gamma \simeq 0.13$ mrad, there is an overlap of the two emissions and thus interference. It was seen that at 7 TeV the low-frequency approximation can be used for a magnet. In this case, the source crossing time, which is characteristic of the interferences and defined in Section 4.3, varies like d/γ^2 (for a given magnet length), where d is the distance between the magnets [23]. In this configuration, the interferences are destructive, there is less total energy produced for 7 TeV protons than for 2 TeV protons (Table 10). This effect is similar to the 'multiple source' effect observed at the LEP 4-dipole miniwiggler that obliged to modify the miniwiggler geometry [25, 26, 27]. Moreover, the maximum intensity is emitted in the beam direction and cannot thus be collected by the extraction mirror. The mirror edge cuts the angular spectral energy density creating additional diffraction at the energy where it is already maximum (see Section 7).

The system is usable only over the energy range 450 GeV–2 TeV for which it was conceived.

Table 10: Superconducting miniwiggler characteristics. Δy is defined on Fig. 39.

				Received energy (1 proton 1 passage)	
Energy	B field	1 magnet deflection	Amplitude Δy	Total	Mirror 40×40 mm^2 at 40m
(TeV)	(T)	(mrad)	(mm)	(J)	(J)
0.45	1.30	0.86	1.3	2.3×10^{-25}	5.6×10^{-26}
2.00	5.78	0.86	1.3	3.2×10^{-21}	4.4×10^{-22}
7.00	6.00	0.26	0.4	1.1×10^{-21}	3.4×10^{-22}

Table 10 gives the total energy produced by the miniwiggler and the portion collected by the extraction mirror taking into account the operating conditions. The results compared with Table 9 show that the superconducting miniwiggler will not yield a good precision for the bunch-by-bunch, turn-by-turn measurements with the nominal bunch, and even less so with the pilot bunch at injection energy.

An alternative to this solution, preserving the principle of the four magnets, was thus considered to improve the performances at 450 GeV.

Optimization of the performances for bunch-by-bunch measurements at 450 GeV. To increase the intensity produced at injection energy, a solution would consist in operating with the maximum magnetic field at 450 GeV, that is to say with $B = 6$ T. In this case, it is the magnet edges which mainly radiate (Fig. 41). The angular separation between the two radiation cones is then equal to the magnet deflection, i.e. $\alpha = BL/B\rho = 4$ mrad.

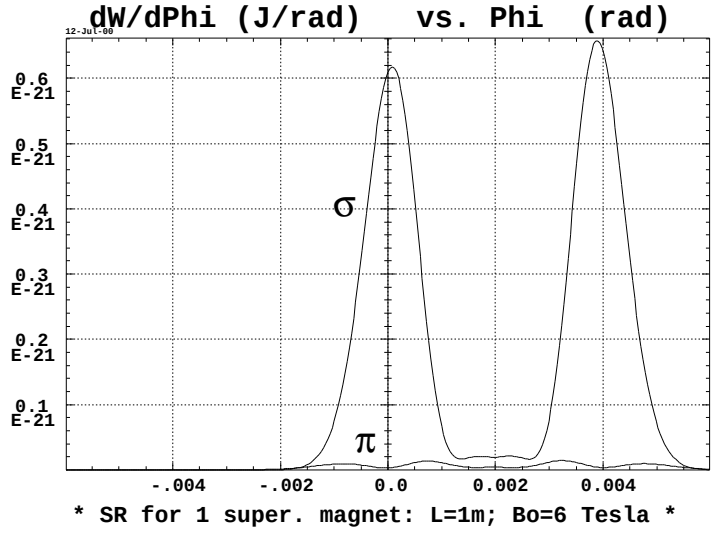

Fig. 41: Projection in the $\psi = 0$ plane of the energy density radiated by a 450 GeV particle in one magnet with $B = 6$ T integrated on the g3 frequency range. The $\phi = 0$ direction corresponds to that of the particle beam at the entrance of the magnet.

Several configurations, summarized in Table 11, were simulated, using one, two, and four magnets. The last two columns, respectively, give the total intensity produced by the device and the intensity intercepted by the extraction mirror 10 m downstream from the source. Indeed, in this case, the strong magnet deflection α insures reaching in a short distance the safety separation of 15σ with respect to the machine central line. Moreover, the distance between the radiation cone axis and the beam trajectory increases very quickly and in order not to have to widen too significantly the vacuum chamber dimensions, it is necessary to place the extraction mirror close enough to the source.

By comparing the data with those of Table 10, one notices that at 450 GeV one magnet with 6 T makes it possible to obtain more intensity than the miniwiggler with 1.3 T. Nevertheless, the problems of closed-orbit bump compensation remain. The simplest solution is thus again to add three magnets with the miniwiggler configuration to locally close the orbit bump. The total intensity emitted by the four magnets is twice that obtained with two magnets, but taking into account the large angular separation between the cones emitted by each edge (equal to the magnets' deflection), one can extract only the part corresponding to the exit of the first magnet and entrance of the second (or in an equivalent way the exit of the third and entrance of the last) (Fig. 42).

Table 11: Results of the various simulated configurations

Layout	B field (T)	Total energy (J)	Energy on mirror (J)
1 magnet	6	1.5×10^{-24}	7.6×10^{-25}
2 magnets	-6 and 6	3.0×10^{-24}	1.5×10^{-24}
4 magnets	-6,6,6,-6	6.2×10^{-24}	1.6×10^{-24}

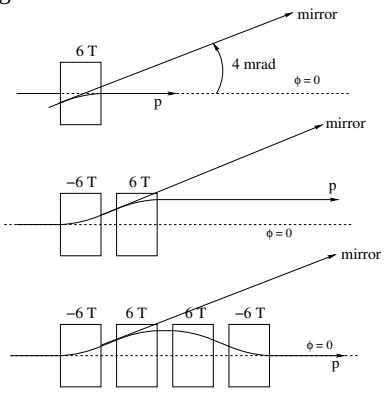

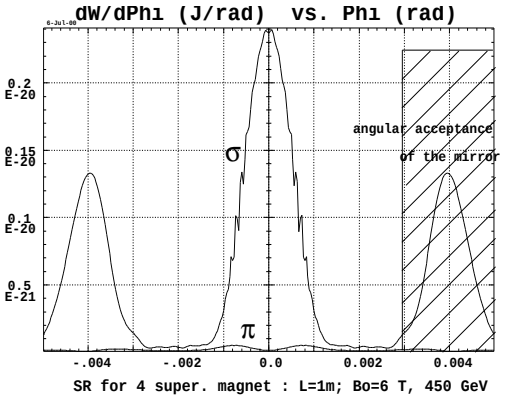

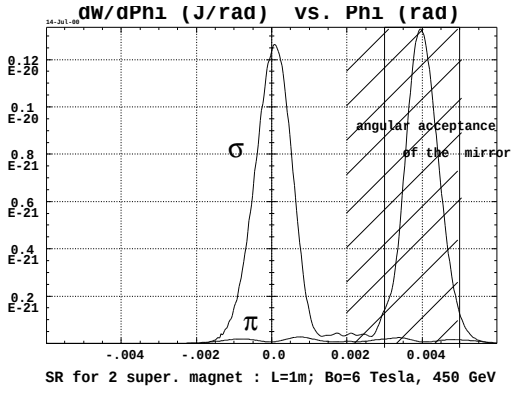

Fig. 42: Projection in the $\psi = 0$ plane of the energy density radiated by four magnets (on the left) and two magnets (on the right) at 450 GeV, with $B = 6$ T and integrated on the g3 frequency range. The direction $\phi = 0$ corresponds to the direction of the beam at the miniwiggler entrance and exit.

The suggested solution to carry out turn-by-turn measurements with a nominal bunch at injection energy is thus to use the miniwiggler configuration (Fig. 39), with a 6 T magnetic field at 450 GeV. The intensity collected by the mirror is then sufficient to measure a profile. However, taking into account the large angular openings, it is necessary to place the extraction mirror at approximately 10 m downstream from the source. When energy increases, the magnetic field in the magnets being maximum at injection, the radiation cone direction varies and approaches the beam direction. The distance between the source and the extraction mirror becomes then too small to extract the light while remaining at 15σ from the beam.

To be able to follow the energy ramp up to 2 TeV, while allowing turn-by-turn measurement with a nominal bunch at injection, the suggested solution is then to use the same source with two extraction mirrors (Fig. 43). A first mirror, placed 10 m from the source is used only with the 6 T miniwiggler for the injection energy. To cover the range 450 GeV–2 TeV, a second mirror placed at 40 m extracts the light produced by the miniwiggler with a variable magnetic field as presented previously.

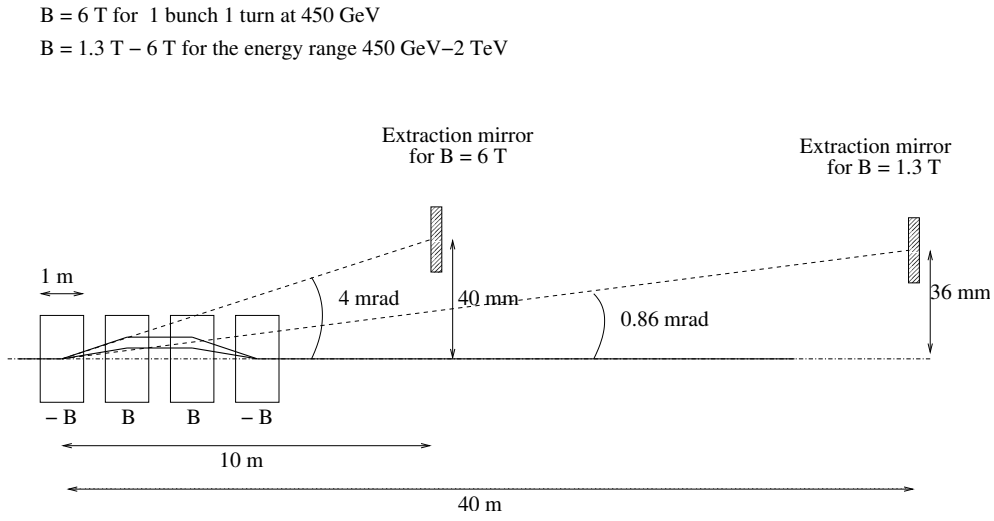

Fig. 43: Double extraction configuration: a first mirror extracts the light at 450 GeV and a second between 450 GeV and 2 TeV

6.1.3 Room-temperature undulator

The objective is still to supplement the synchrotron light monitor at D2 from 450 GeV to 2 TeV.

Choice of the geometry of the undulator Equation (38) $\lambda_1 = \frac{\lambda_u}{2\gamma^2}\left(1+\gamma^2\theta^2\right)$ shows that the wavelength emitted for fixed θ decreases when energy increases. To be able to use the undulator in the largest possible energy range, one thus chooses λ_1 in the $\theta = 0$ direction near to the maximum of the optical detector's wavelength acceptance bandwidth, that is to say $\lambda_1(\theta = 0)$ = 760 nm. The undulator spatial period was then fixed at λ_u = 35 cm. When the beam energy increases, the emitted wavelength in θ = 0 is outside the detector's spectral bandwidth (200–900 nm), Table 12. Nevertheless, Eq. (38) shows also that the emitted wavelength increases with the observation angle. With the extraction mirror at 30 m, the angular acceptance is 1.33 mrad, thus making it possible to widen the range of wavelengths collected [Eq. (38) and Fig. 44].

The emitted intensity is proportional to the square of the magnetic field and to the number of periods [Eq. (42)]. With the current technologies of warm or permanent magnets [35], the maximum reachable field is approximately B_0 = 1.2 T. On the one hand, the choice of the number of period is

Table 12: Wavelength and synchrotron radiation energy emitted in the $\theta = 0$ direction by the 35 cm long period undulator

Energy	450 GeV	750 GeV	1 TeV	2 TeV	7 TeV
γ	480.6	837.2	1116.3	2232.58	7460
$\lambda_1(\theta = 0)$ (nm)	760	250	140	35	3.1
$\hbar\omega/q$ (eV)	1.63	4.97	8.87	35.5	400.6

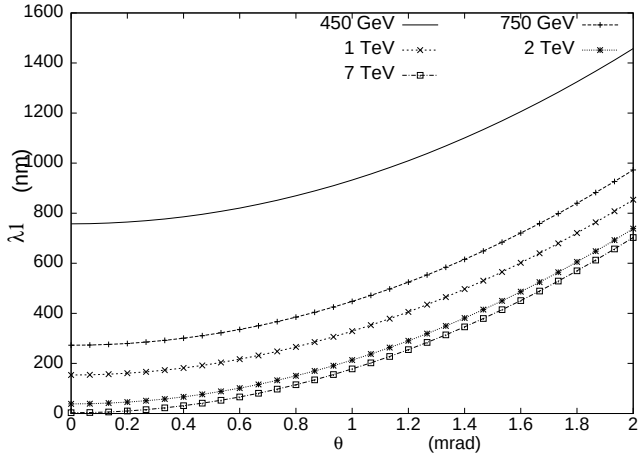

Fig. 44: Wavelengths emitted by the 35 cm long period undulator for various observation directions θ and various proton energies

fixed by the overall source length and by the spectral dispersion around the ω_1 frequency, proportional to $1/N$ [Eq. (42)]. In the case of beam profile measurements, the emitted wavelengths in the angular acceptance of the mirror cross the detector spectral acceptance during the proton beam energy ramp, Table 12. So a quasi-monochromatic source is not an advantage. Moreover, the overall source length conditions the depth of field effects, see Section 7. A limited period number is thus desirable. To cover the 450 GeV–2 TeV energy range while maximizing the emitted intensity, the undulator is thus composed of five periods. With these characteristics, $K = 0.02$; the approximation of Eq. (38) is thus justified. It should be noted, Fig. 45, that the vertical projection ($\phi = 0$ plane) of emitted radiation at 450 GeV is larger than the horizontal one ($\psi = 0$ plane).

Spectral angular energy density at 2 TeV Figure 46 shows the spectral density emitted in the undulator by a 2 TeV proton for the g3 range. As the intensity distribution does not present cylindrical symmetry around the $\theta = 0$ axis, instead of a 1 mrad radius annular distribution, the intersection of the spatial term $F_{u,\sigma}(\theta, \varphi) = (1 - \gamma^2\theta^2 \cos(2\varphi))^2/(1 + \gamma^2\theta^2)^5$ and the spectral term $f_{N_u}(\omega - \omega_1) = \frac{N_u}{\omega_1}\left(\sin\left(\frac{(\omega-\omega_1)\pi N_u)}{\omega_1}\right)/\frac{(\omega-\omega_1)\pi N_u)}{\omega_1}\right)^2$ of Eq. (42) gives a series of peaks, higher in the vertical plane ($\varphi = \frac{\pi}{2}$ gives $\cos(2\varphi) = -1$) than in the horizontal plane ($\varphi = 0$ gives $\cos(2\varphi) = 1$).

The minimal wavelength detected in g3 (i.e 350 nm) corresponds at 2 TeV to a $\theta = 1.33$ mrad angle. However, the intensity emitted in the direction (θ, $\varphi = \frac{\pi}{2}$) varies roughly like $1/(1 + \gamma^2\theta^2)^3$ [Eq. (42)]. The maximum intensity emitted in the $\theta = 1.33$ mrad direction is thus 750 times lower than that emitted in $\theta = 0$. While moving away from the undulator axis, one intercepts the rings corresponding to wavelengths to which the detectors are sensitive (Fig. 46), but one loses enormously in intensity. The levels are then comparable with those emitted at 450 GeV, Table 13.

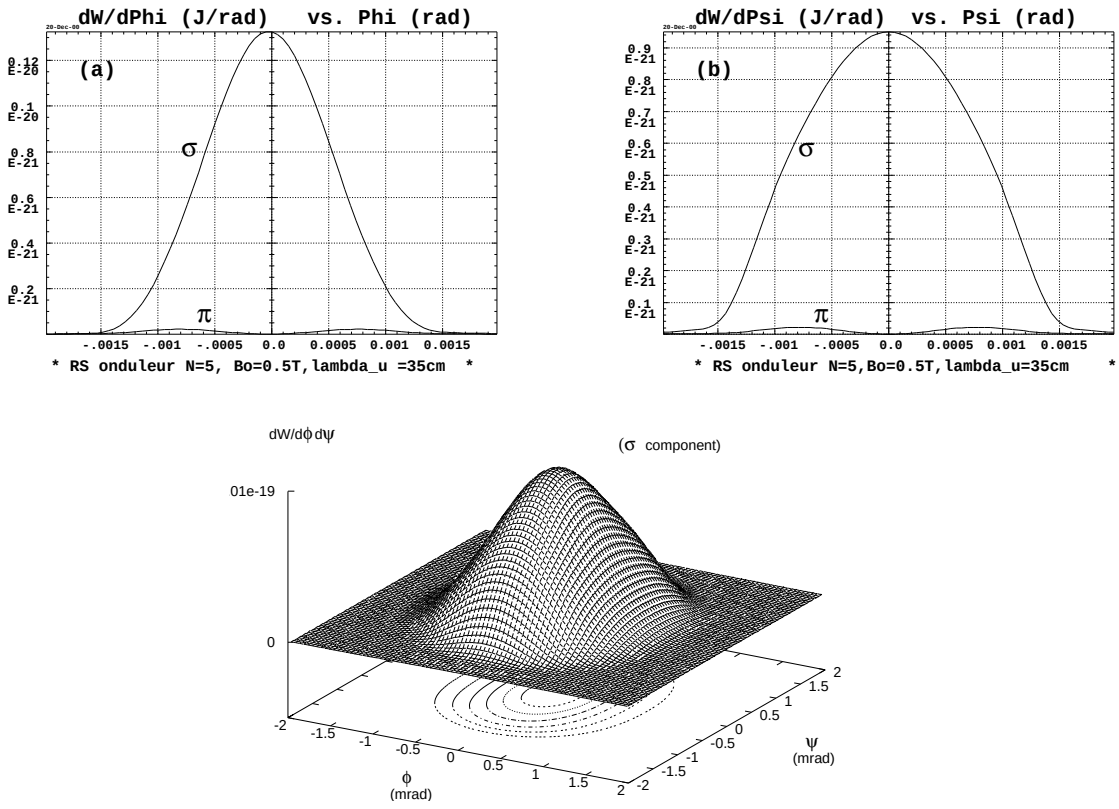

Fig. 45: Projections in the $\psi = 0$ horizontal plane (a), the $\phi = 0$ vertical plane (b), and 3 D plot (σ component) of the energy density integrated on the 350–1100 nm wavelengths range for a five periods undulator with $\lambda_u = 35$ cm, $B_0 = 1.1$ T and for a 450 GeV proton.

Table 13: Energy collected in the case of an undulator of five periods of 35 cm with a 1.2 T magnetic field

Energy	Configuration			Energy
	B	λ_u	$\lambda_1(\theta = 0)$	1 proton / 1 passage
(TeV)	(T)	(cm)	(nm)	(J)
0.45	1.1	35	760	1.8×10^{-24}
2.00	1.1	35	35	2.1×10^{-24}

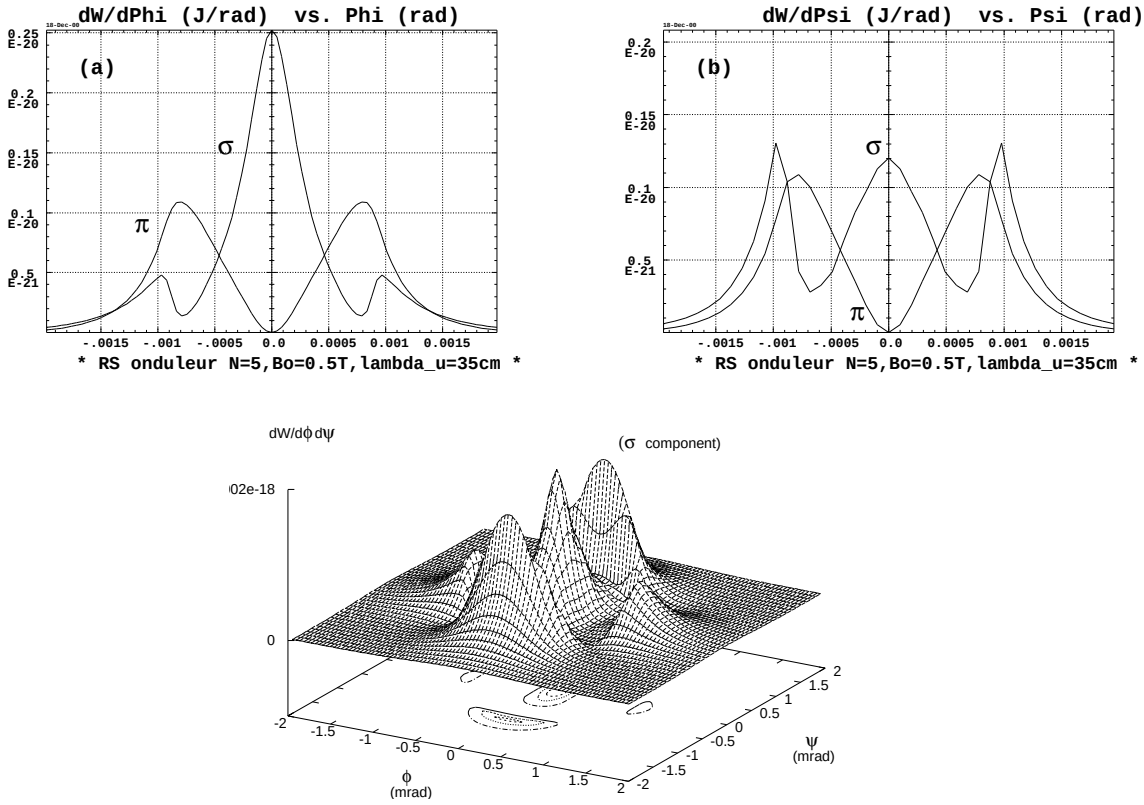

Fig. 46: Projections in the $\psi = 0$ horizontal plane (a), the $\phi = 0$ vertical plane (b), and 3 D plot (σ component) of the energy density integrated over the 350–1100 nm wavelengths range for five periods undulator with $\lambda_u = 35$ cm, $B_0 = 1.1$ T and for a 2 TeV proton.

Proposed configuration According to Eq. (38), the emitted wavelength increases with the observation angle θ, but at the same time the intensity decreases very quickly with $F_u(\theta,\varphi) = (1+\gamma^2\theta^2\cos(2\varphi))^2/(1+\gamma^2\theta^2)^5$ [Eq. (42)]. So, beyond $1/\gamma$ the radiated intensity becomes negligible compared with that emitted in the $\theta = 0$ direction, approximately 2000 times less.

To obtain a sufficient signal level with 450 GeV protons, it is preferable to intercept the light emitted in the undulator axis direction. In IR4 of the LHC, the synchrotron radiation source is placed between two quadrupoles in a straight section; the undulator axis direction is thus also that of the particle beam at its exit. To be able to extract the light even with a small cone opening angle, it is thus necessary to insert deflection magnets to create, as in the miniwiggler case, a local closed-orbit bump (Fig. 47). Four 5 m long magnets with a peak magnetic field of 0.38 T at 450 GeV up to 1.7 T at 2 TeV, must

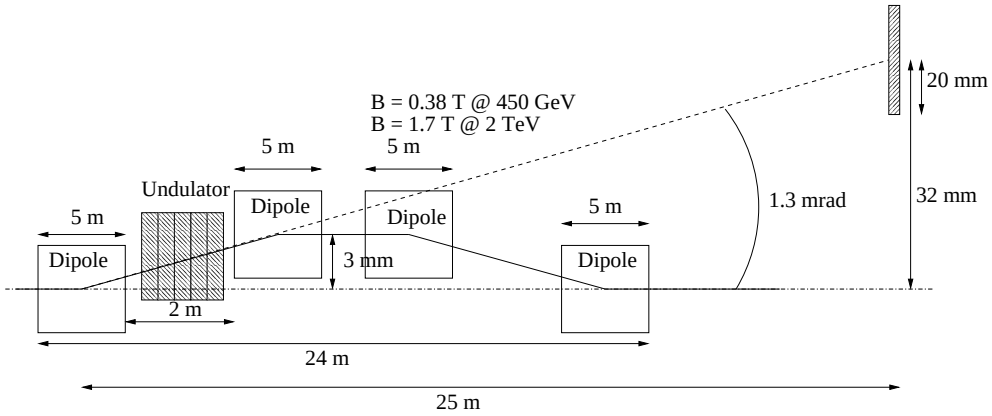

Fig. 47: Configuration of the undulator light source. The unit is composed of four room-temperature dipoles creating a self-compensated closed-orbit bump. The source itself, i.e the undulator, is placed between the first two magnets. The $\theta = 0$ SR emission direction is shifted by 1.3 mrad compared to the proton beam axis at the extraction point.

be used to create the closed-orbit bump. When placing the undulator between the first two magnets, the principal emission direction will be separated from the beam axis by 1.3 mrad (Fig. 47). The device has a 24 m overall length and the extraction is done 25 m downstream of the centre of the first deflection magnet.

However, with $B = 1.7$ T at 2 TeV, the magnet edges emit also in the spectral range considered with an intensity comparable to that of the undulator. The source is thus comprised of the two edges and of the undulator (Fig. 48). With the $\phi = 0$ direction corresponding to the undulator axis direction, the comparison between the angular energy densities with and without the undulator shows that its presence modifies only slightly the signal level emitted by the two edges.

To try to make the undulator signal emerge at 2 TeV, and thus to limit the source length, we planned to add a second undulator optimized for 2 TeV after the first undulator optimized for 450 GeV. But to bring back the emitted wavelength in the $\theta = 0$ direction at 2 TeV in the g3 range, one needs a 1.7 m long spatial period. In order to limit the source length, it is then necessary to reduce the number of periods to N_u = 2. One can improve slightly the intensity level emitted in the λ_u = 1.7 m undulator compared to the shorter λ_u = 35 cm undulator, but taking into account the small number of periods, the edges emit even more light. It thus does not appear interesting to introduce another specific source for 2 TeV because the diagnostics can be made with the edges of the first two deflection magnets (exit of the first dipole and entrance of the second one).

Undulator performance between 450 GeV and 2 TeV A possible configuration is then that presented in Fig. 47, with four 5 m long magnets to create a closed orbit bump and deviate the undulator radiation

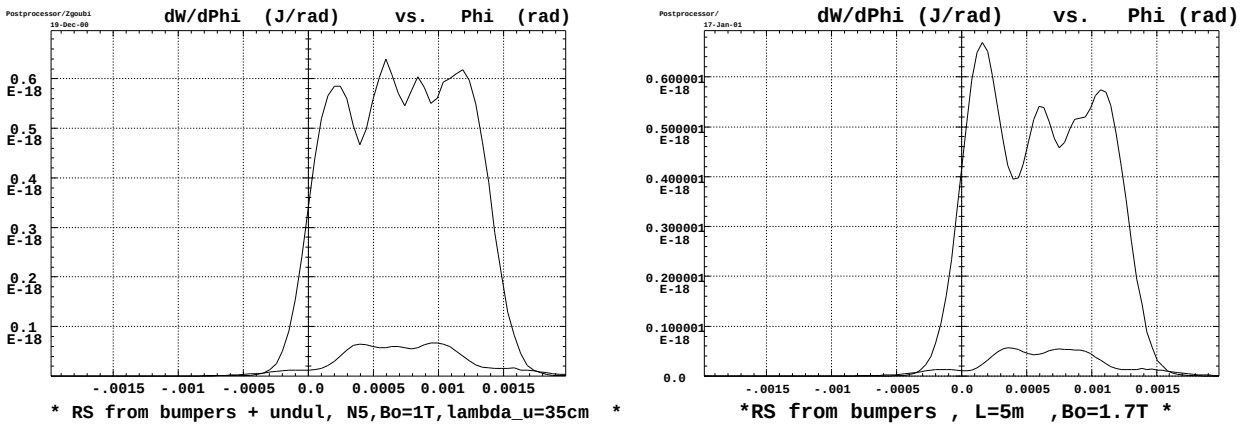

Fig. 48: Projections in the horizontal plane of the energy density integrated over the 350–1100 nm frequency range emitted by a 2 TeV proton, for two 5 m long deflection magnets with a 1.7 T magnetic field (on the right), and for the two magnets plus an undulator with five 35 cm long periods and $B = 1.1$ T (on the left).

axis from the proton beam direction. The undulator is inserted between the first two magnets to increase the intensity collected at injection energy. The magnetic field in the deflection magnets follows the proton beam energy ramp to maintain a constant undulator radiation emission direction. Table 14 shows that this source allows beam diagnostics over the whole 450 GeV–2 TeV energy range.

Table 14: Energy collected by the extraction mirror in the case of an undulator with five 35 cm long periods, of $B = 1$ T and a separation of 1.3 mrad between the proton beam axis and the undulator axis (cf. Table 9)

Proton energy (TeV)	$\lambda_1(\theta = 0)$ (nm)	Energy (J): 1 proton/1passage	
		Total	Mirror (40×40 mm at 25 m)
0.45	760	1.7×10^{-24}	1.1×10^{-24}
0.75	250	8.3×10^{-24}	6.0×10^{-24}
1.00	140	1.4×10^{-23}	9.3×10^{-24}
2.00	38	8.8×10^{-22}	4.7×10^{-22}
7.00	3	2.5×10^{-21}	4.3×10^{-23}

6.1.4 Superconducting undulator

To increase the performance of the undulator while keeping a reasonable source length, a possible solution consists in increasing the peak magnetic field. The use of superconducting magnets is then necessary. The peak magnetic field increase by a factor 5 makes it possible to decrease the number of periods by a factor 2 while still increasing the intensity [Eq. (42)], in order to still reduce the longitudinal source extent and to limit the depth of field effects for the optics. The superconducting undulator studied consists of two 28 cm long periods with a peak magnetic field of 6 T. The various wavelengths emitted in a given observation direction as a function of the proton energy are presented in Table 15. At injection energy, the wavelength in the $\theta = 0$ direction is in the middle of spectral acceptance range g3 of the detector, and the intensity spatial distribution (Fig. 49, left) is a cone emitted in the beam direction.

The undulator is 'out of tune' at 2 TeV: the useful wavelengths (in the g1 range) are emitted with θ angles of the order of one mrad and thus attenuated compared to the maximum emitted in $\theta = 0$, because of the angular term $F_u(\theta, \varphi) = (1 - \gamma^2\theta^2 \cos(2\varphi))^2/(1 + \gamma^2\theta^2)^5$ of Eq. (42).

Table 15: Wavelengths emitted in the θ direction for various proton energies by an undulator of spatial period $\lambda_u = 28$ cm, $K = 0.074$.

λ	θ (mrad)				
(nm)	0	0.5	1	1.5	2
450 GeV	600	643	748	923	1168
2 TeV	31	66	171	346	591
7 TeV	2.5	38	143	318	563

At the same time, the attenuation of the intensity emitted in the $\theta = 0$ direction for any λ wavelength compared to the fundamental $\lambda_1(\theta = 0) = \frac{\lambda_u}{2\gamma^2}$ emitted in this same direction varies like $f_{N_u}(\omega - \omega_1) = \frac{N_u}{\omega_1}\left(\sin\left(\frac{(\omega-\omega_1)\pi N_u)}{\omega_1}\right)/\frac{(\omega-\omega_1)\pi N_u)}{\omega_1}\right)^2$. However, for 2 TeV, $N_u = 2$, $\omega = 9.42 \times 10^{15}$, the attenuation ratios between ($\theta = 0$, $\lambda = 31$ nm) and ($\theta = 1.5$ mrad, $\lambda = 318$ nm) are:

$$\frac{F_u(0,0)}{F_u(1.5 \times 10^{-3}, 0)} = 2095.16 \quad (103)$$

$$\frac{f_{N_u}(\omega - \omega_{1,\theta=0})}{f_{N_u}(\omega - \omega_{1,\theta=1.5 \text{ mrad}})} = 98.47 \ . \quad (104)$$

The useful wavelengths are all the more attenuated at large θ and the central peak, although out of tune, remains higher than the annular ring because of the small number of periods. But, for a large number of periods (e.g $N_u = 20$, $f_{N_u}(\omega - \omega_{1,\theta=0})/f_{N_u}(\omega - \omega_{1,\theta=1.5 \text{ mrad}}) > 79\ 000$), the central peak is more attenuated than the ring.

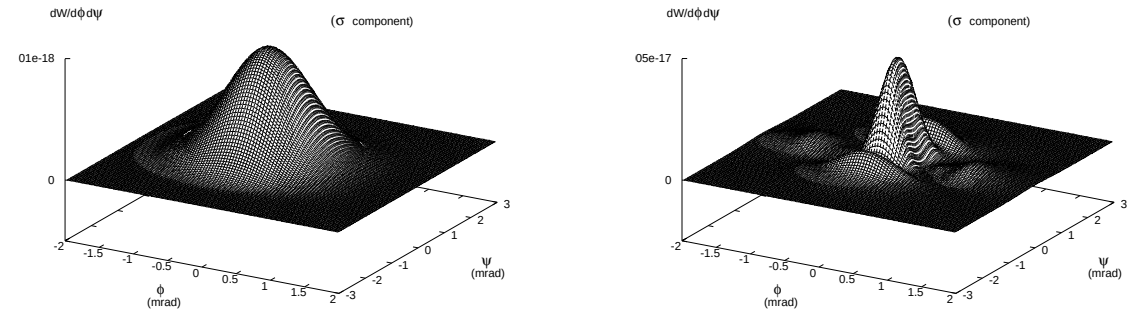

Fig. 49: Angular energy density emitted by the superconducting undulator (450 GeV, left and 2 TeV, right) in the g3 frequency range

Various possibilities were considered for the light extraction. Initially, the existence of a long free straight section (approximately 90 m) in IR4, made it possible to consider an extraction in the vertical plane with only an undulator as the source. Indeed, while changing the spatial period, it is possible to choose the emission direction of a given wavelength for a given energy. However, one cannot choose too large an angle because of the attenuation related to the form factor, Eq. (42). The limit is fixed around 2 mrad to extract the light without deviating the particle beam within a source-to-mirror distance of 35 m (Fig. 50). In this case, the extraction is done in the plane where the beam dimensions are the smallest in order to approach the closest possible to the beam but always within the clearance limit of 15σ.

During the study, the IR4 configuration was modified and it is now possible to place the undulator upstream of the D3 dipole (Fig. 51 and Table 16). This dipole, of the same type as the D2 dipole of IR1/5

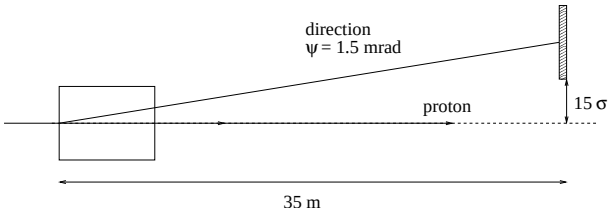

Fig. 50: Light extraction with undulator alone

but with a peak magnetic field of 3.9 T at collision energy, is part of the "dogleg" which provides the separation of the two beams for the installation of the accelerating cavities.

Table 16: D3 dipole characteristics. One notices that the critical frequency crosses the observation range in the course of the energy ramp.

Energy (TeV)	γ	ω_c		ω_l (eV)
		(eV)	(s^{-1})	
0.45	480.6	0.005	8.3×10^{12}	0.008
0.75	800.3	0.025	3.8×10^{13}	0.018
1.00	1066.8	0.060	9.1×10^{13}	0.025
2.00	2132.6	0.479	7.3×10^{14}	0.040
7.00	7461.5	20.50	3.1×10^{16}	0.049

The D3 dipole downstream the undulator makes it possible to extract the light emitted on the undulator axis direction and thus to collect the maximum intensity emitted along $\theta = 0$ (Fig. 51). It introduces at the same time a second light source which becomes preponderant for high-energy protons since the D3 entrance edge radiates in the same direction as the undulator. It is thus necessary to consider it for the emitted intensity evaluation as well as for calculations of optical performance (depth of field). Table 17 shows the intensities collected with the configuration of Fig. 51, for the D3 edge alone, the undulator alone, and the whole undulator plus D3 edge source.

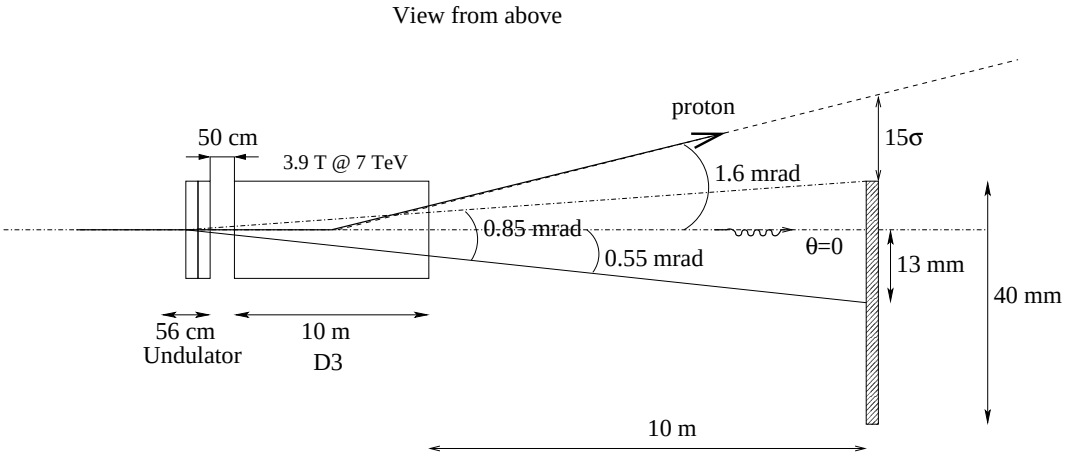

Fig. 51: Configuration in IP4: an undulator with two 28 cm long periods in front of the D3 dipole

Table 17: Energy collected for the g1 range by a 40×40 mm^2 mirror 20 m from the source shifted by 0.55 mrad compared to the undulator axis (see Table 26). The distance between the undulator and the D3 entrance is 50 cm. The column ' D3 centre' corresponds to the energy received with a slit limiting the horizontal acceptance to 0.25mrad, for comparison. These values have been obtained for the maximum field 4.5 T in D3 at 7 TeV (the nominal field 3.9 T yields value different by less than 1% different values for energies above 1 TeV).

Energy (TeV)	D3 centre (J)	D3 edge only (J)	Undul. only (J)	Undul. + D3 edge (J)
0.45	1.2×10^{-28}	9.1×10^{-28}	9.9×10^{-24}	9.9×10^{-24}
0.90	2.8×10^{-27}	2.1×10^{-25}	3.1×10^{-23}	3.1×10^{-23}
1.00	2.9×10^{-27}	4.1×10^{-25}	2.0×10^{-23}	2.1×10^{-23}
1.50	7.4×10^{-25}	8.7×10^{-24}	8.5×10^{-24}	1.9×10^{-23}
2.00	4.1×10^{-23}	1.8×10^{-22}	5.8×10^{-24}	1.8×10^{-22}
7.00	3.7×10^{-21}	1.3×10^{-20}	6.2×10^{-25}	1.3×10^{-20}

Below 1 TeV the main source is the undulator, while at high energy (above 2 TeV), it is the D3 edge. For intermediate energies, the contribution of the two sources is approximately of the same order, Table 17.

6.2 Comparison of the different sources

The comparisons presented hereafter take into account the specific geometrical configurations of each solution. The sources compared are:

1. **Miniwiggler** (Fig. 39): four superconducting 1 m long magnets with B_0 = 6 T; magnetic field increased proportionally with the energy ramp between 450 GeV and 2 TeV; extraction at 25 m in the direction of the first magnet exit.

2. **Miniwiggler with double extraction** (Fig. 43): the same miniwiggler (four superconducting magnets with extraction at 25 m), with an additional extraction mirror at 10 m to increase the collected intensity at 450 GeV for a pilot bunch with the magnetic field at 6 T.

3. **Room-temperature undulator** (Fig. 47): 35 cm period undulator with a 1 T magnetic field plus four 5 m long dipoles allowing a constant deflection of 1.3 mrad from 450 GeV to 2 TeV; extraction in the direction of the first magnet exit.

4. **Superconducting undulator** (Fig. 51): undulator with two 28 cm long periods with a field of 6 T upstream of D3; extraction at 25 m from the undulator in the direction of the axis thanks to the D3 dipole deflection.

Tables 18 and 19 compare the sources studied in terms of calculated intensities collected at the extraction mirror on the g3 wavelengths range at 450 GeV and at 2 TeV. The minimum required energy for obtaining a profile is shown in Table 9.

To make the comparison more realistic, magnetic field map simulations in the various magnetic elements considered were carried out and used for the numerical calculation of the collected intensity.

'Real' miniwiggler For the miniwiggler made of 1 m long prototype superconducting magnets, the simulated magnetic field presents strong irregularities at the end (Fig. 52), and does not reach the nominal 6 T field. Moreover the effective magnetic length is 90 cm.

Table 18: Comparison of the intensities collected in the various configurations studied at 450 GeV. Simulation for the g3 wavelength range. The denomination 'Class. undulator' indicates an ideal room-temperature undulator.

Layout	Configuration		Energy (J)
	B, B_0 (T)	Total length	On mirror (1 part., 1 turn)
Miniwiggler	1.3	5.5 m	5.60×10^{-26}
Double extraction	6	5.5m	1.60×10^{-24}
Class. undulator	1	5×35 cm	1.10×10^{-24}
Superc. undulator	6	2×28 cm	1.04×10^{-23}

Table 19: Comparison of the energies collected in the various configurations studied at 2 TeV. Simulation for the g3 wavelength range. The double extraction case is the same as the simple extraction miniwiggler at this energy (Fig. 43).

Layout	Configuration		Energy (J)
	B (T)	Total length	On mirror J (1 part., 1 turn)
Miniwiggler	6	5.5 m	4.4×10^{-22} 40 m
Class. undulator	1	5×35 cm	4.7×10^{-22} 25 m
Superc. undulator	6	2×28 cm	5.0×10^{-23} 25 m

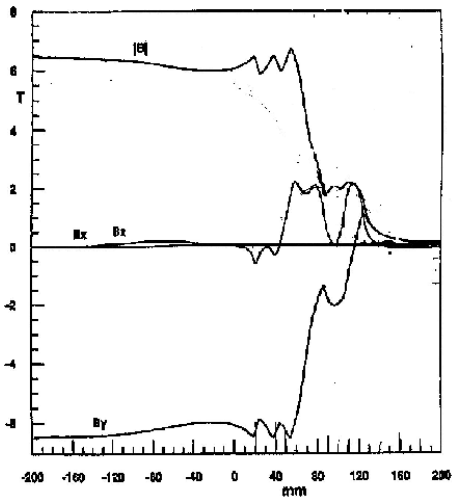

Fig. 52: Simulation of the fringe fields in a 1 m long superconducting dipole [36]

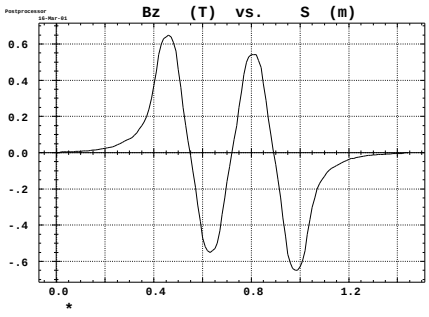

Fig. 53: Simulation of the B_z component of the magnetic field with two 35 cm long periods [37]

The variations obtained for the intensity according to these various parameters can reach a factor 5, Table 20.

Table 20: Collected energies including the differences with respect to the nominal parameters for the miniwiggler and 450 GeV. The first line is a reminder of the required parameters. L and d are defined on Fig. 39.

Proton energy (TeV)	Layout		α (mrad)	d (cm)	Energy (J): 1 proton 1 turn mirror (40×40 mm^2)
	L (m)	B (T)			
0.45	1.0	-6;6;6;-6	4.0	50	1.6×10^{-24} 10 m
0.45	0.9	-6;6;6;-6	3.6	70	8.6×10^{-25} 15 m
0.45	0.9	-5;5;5;-5	3.0	70	5.4×10^{-25} 15 m
0.45	0.9	-4;4;4;-4	2.4	70	3.2×10^{-25} 15 m

'Real' undulators For the room-temperature undulator, the simulated magnetic field map (Fig. 53) was used with the TOSCA Zgoubi procedure [29, 30], Section 5.2. With this type of small dipole assembly, it is not possible to reduce the undulator period and the obtainable maximum field is 0.6 T. Under these conditions, the performance of the room-temperature undulator is clearly below the requirements, Table 21.

Table 21: Energies taking into account the various errors compared to the nominal parameters for the room-temperature undulator at 450 GeV. The term 'OPERA3D simulation' indicates a simulation using the undulator field map coming from the OPERA3D code.

Type	B (T)	λ_u (cm)	L (cm)	Collected energy (J) per proton	
				Centre	15 σ
Class. undulator	1.2	22.2	111	9.31×10^{-25}	5.84×10^{-25}
OPERA3D simulation	0.6	40.0	140	9.10×10^{-26}	3.81×10^{-26}
Class. undulator	0.6	35.0	70	1.06×10^{-25}	4.61×10^{-26}
Class. undulator	0.6	35.0	175	3.39×10^{-25}	1.39×10^{-26}

Only the magnetic field simulations carried out for the superconducting undulator correspond to the optimum parameters (Fig. 54 and Table 22).

Table 22: Comparison between the ideal sinusoidal fields simulated with the UNDULATOR procedure ('Super. undul.') and ROXIE field maps used with the TOSCA procedure ('ROXIE simulation')

Type	B (T)	λ_u (cm)	Collected energy (J) per proton	
			400–600 nm	200–900 nm
Super. undul.	6.0	22.2	2.88×10^{-24}	5.41×10^{-24}
ROXIE simulation	6.0	35.0	2.75×10^{-25}	4.80×10^{-24}
Super. undul.	4.5	22.2	1.64×10^{-24}	3.07×10^{-24}

Comparison between the 'real' sources When considering the feasible parameters for each type of source, the comparison between the various solutions is clearly in favour of the superconducting undulator, Table 23.

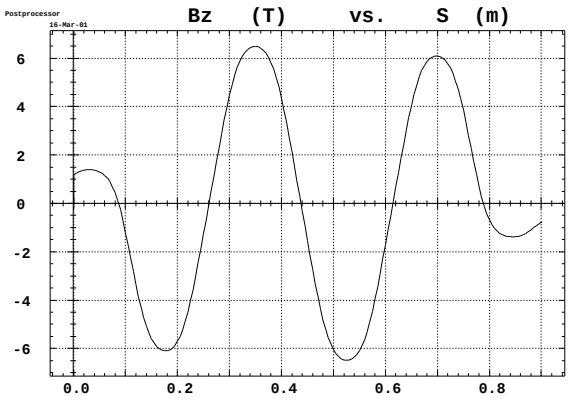

Fig. 54: Field simulation with two periods (ROXIE)

Table 23: Comparison of the simulations based on magnetic field maps at 450 GeV. ΔY represents the maximum closed-orbit bump amplitude.

Type	B,B_0 (T)	λ_u (cm)	L, L_u (cm)	ΔY (μm)	Energy per proton per turn (J)
Real miniwiggler	5.0	90.0	555	4800	5.40×10^{-25}
Class. undulator	0.6	35.0	140	29	9.10×10^{-26}
Permanent magnet	1.2	22.2	111	33	9.31×10^{-25}
Superc. undulator	6.0	35.0	70	100	4.80×10^{-24}

6.3 Sources considered for beam diagnostics

6.3.1 For the whole energy range: undulator and D3 edge

Among all the studied sources, the $\lambda_u = 28$ cm, two periods, B = 5 T superconducting undulator is the one that provides the largest intensity and has the shortest length. Figure 55 shows the configuration proposed for the source in IR4.

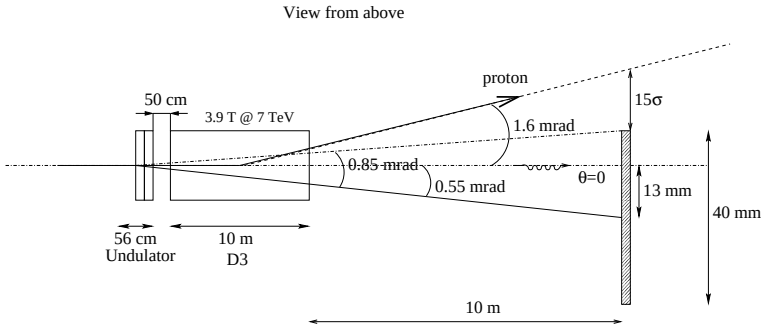

Fig. 55: Configuration of the implementation of the $\lambda_u = 28$ cm, two periods, B = 5 T superconducting undulator in IR4

The undulator is currently under construction. A model was implemented [38] (Fig. 56 with the parameters given in Table 24 and Appendix C).

The performance and characteristics of this source are presented in Table 25 and on Fig. 57, showing the boundaries of the intensity collected at the extraction mirror for three representative energies.

Table 24: Undulator main parameters

Period	280 mm
Period number	2
Iron yoke length	710 mm
Gap	60 mm
Beam tube size	50 mm inside / 53 mm outside
Maximum magnetic field in the gap	5 T
Maximum field error within $\pm$ 10 mm from axis	0.25%
Supply current	250 A
Total energy stored at 250 A	150 kJ
Magnet inductance	4.8 H
Coil cross-section	36.5×42.5 mm^2
Cable size	1.25×0.73 mm^2
Overall coil size	$140\times220\times36.5$ mm^3
Operating temperature	4.2 K
Margin to quench on load line	20%

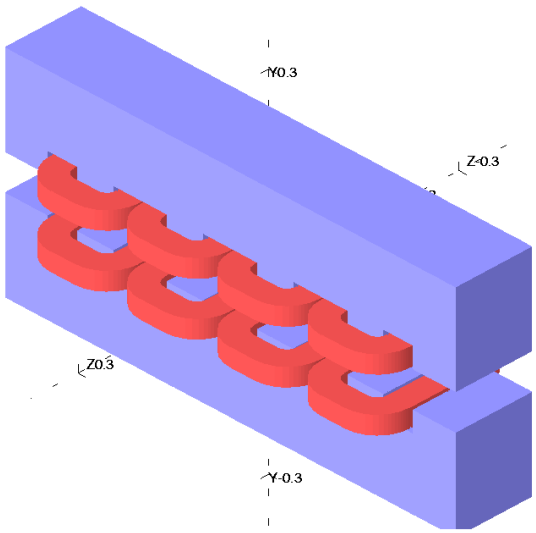

Fig. 56: Full view of the model of the electromagnetic undulator

Table 25: Energies produced by the source in IR4 for various wavelength ranges corresponding to the acceptances of various detectors (with 4.5 T in D3 at 7 TeV)

Proton energy (TeV)	Energy collected on the 40 $\times$ 40 mm^2 mirror (J)			
	200–900 nm 1 part./1 turn	400–600 nm 1 part./1 turn	600–900 nm 1 part./1 turn	400–900 nm 1 part./1 turn
0.45	1.5×10^{-23}	4.1×10^{-24}	1.1×10^{-23}	1.5×10^{-23}
0.75	6.1×10^{-23}	6.1×10^{-24}	1.1×10^{-24}	7.2×10^{-24}
1.00	3.3×10^{-23}	2.9×10^{-24}	8.5×10^{-25}	3.7×10^{-24}
2.00	5.5×10^{-23}	1.7×10^{-23}	2.4×10^{-23}	4.1×10^{-23}
7.00	2.2×10^{-21}	4.9×10^{-22}	3.0×10^{-22}	7.9×10^{-22}

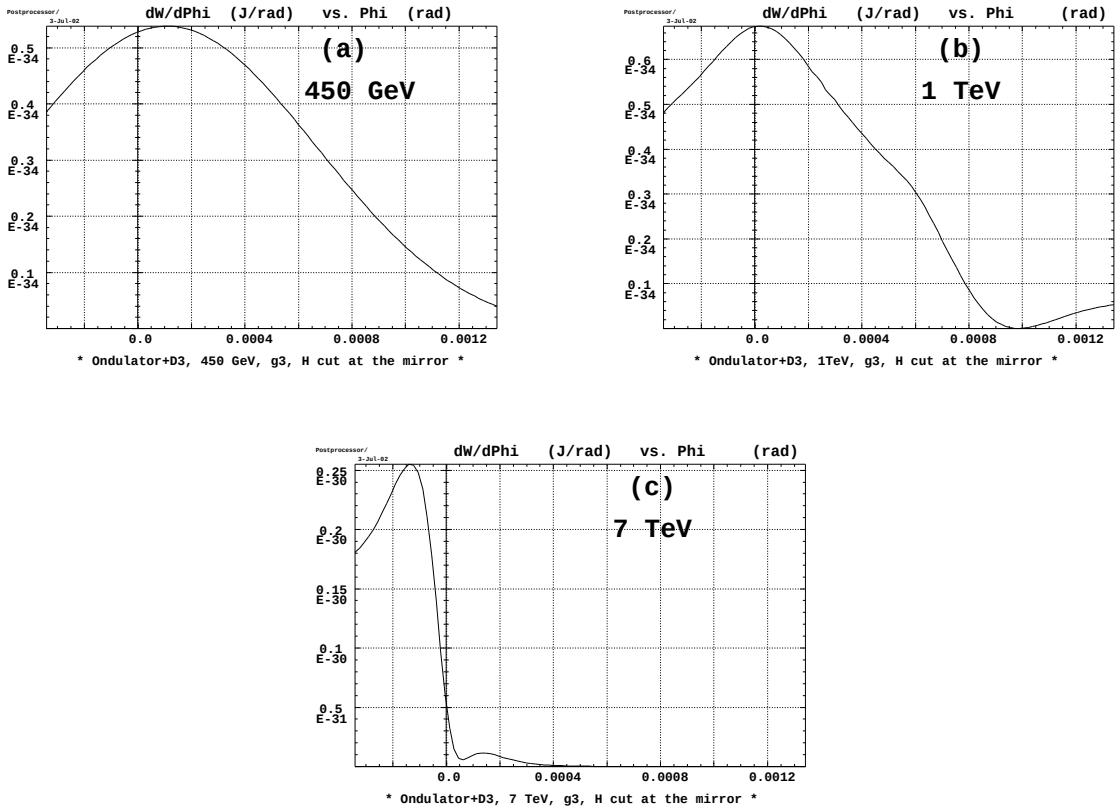

Fig. 57: Cuts in the horizontal plane ($\psi = 0$) of the energy density emitted by the undulator–D3 source at 450 GeV (a), 1 TeV (b), and 7 TeV (c), integrated over the wavelength range 200–900 nm. The direction ϕ = 0 corresponds to the direction of the proton beam at the entry in the undulator. The curves correspond to the horizontal component (σ).

The superconducting undulator provides sufficient intensity to measure the profiles with 5% precision from the injection energy up to approximately 1 TeV. From 1 to 2 TeV, the contributions of the undulator and of the D3 edge are comparable in terms of signal level. There are interferences between the two sources and the depth of field effect degrades the measuring accuracy. To minimize this effect, the distance between the two sources must be minimal and the undulator must be placed directly in the D3 dipole cryostat, Section 7.4.3. The minimum distance between the two sources is then 50 cm.

Above 2 TeV, it is mainly the D3 dipole edge which emits light in the collected wavelength range. In the first part of this section, the study of the D2 dipole led to the conclusion that its use as a source was appropriate from 2 TeV onwards. The D3 dipole emits even more light, its magnetic field being stronger.

Thus, the combination of the undulator and D3 makes it possible to have a source which covers the whole energy range. This geometry is understood free of any other SR sources (e.g orbit correctors, lattice quadrupoles) so as to avoid parasitic multiple source and interference effects.

6.3.2 From 2 TeV to 7 TeV: D2 dipole

To improve the resolution for profile measurement at the collision energy, it is possible to use the D2 dipole in IP5 (or IP1), where the machine optical functions are modified when switching to the the 'low β' collision mode (Figs. 4 and 5, and Table 2). At the measurement point, the β functions are thus increased by a factor 6 (from 100 m up to 600 m in the horizontal plane) and the beam to be measured is 2.4 times larger. The diffraction and depth of field effects being the same for the same diagnostics system, the relative effect compared to the beam sizes decreases and it would be possible to reach a better resolution.

6.4 Conclusion

The study of various synchrotron radiation source types for diagnostics in the LHC, summarized in this section, made the final choice evolve. The monitor using the D2 dipole initially planned as the main monitor will be installed only if it turns out to be necessary to have higher precision measurements in the optics collision mode. For the profile measurement over the whole energy range, the monitor using the superconducting undulator combined with D3 was finally considered as the sole means of measurement using synchrotron radiation for the LHC commissioning.

7 OPTICAL ANALYSIS OF THE DIAGNOSTICS SYSTEM

The synchrotron radiation source was selected according to the optimization of the collected signal level, in order to be able to measure profiles over the whole proton energy range. However, we still need to evaluate the degradation of the monitor performance introduced by the diffraction effect, the depth of field effect, and the imaging system. The first part of this section describes the unit called 'telescope', made up of the optical chain and CCD detector. The two following parts elaborate on the methodology used to evaluate the diffraction and depth of field effects. Finally, the last part presents the performance analysis according to the various adjustable system parameters, treated numerically with the computer code SRW [39].

7.1 Choice of the optical device

7.1.1 Detector

The CCD detector used consists of a matrix of 23 μm $\times$ 23 μm pixels, distributed over 288 lines and 384 columns. The spectral response of the detector extends, according to component type, from 200 nm to 900 nm [40] (range called g1) for the back-illuminated one or from 350 nm to 1100 nm [41] (range called g3) for the front-illuminated one. The CCD sensor considered is composed of two parts: the image zone used for data acquisition and a memory zone in which these data are stored temporarily. The transfer

from one zone to the other, which lasts approximately 0.16 ms, is done at the end of the integration time, thus making it possible to read the data while another acquisition begins. The electronics control of the CCD allows choosing integration and reading times [34]. In TV mode, the CCD is part of a conventional TV camera with an exposure time of 20 ms. In digital mode, the integration time can be selected between 100 μs and 65 ms and the pixels are read one by one at a 1 MHz frequency.

For 'bunch-by-bunch' or 'turn-by-turn' measurements, an optoelectronic shutter made of Multi Channel Plate (MCP) is coupled to the CCD [17] because the time interval between two successive bunches is only 25 ns. Its spectral range is limited by the photocathode, typically between 450 nm and 850 nm (range called g2) for a photocathode of type Super S25 [14].

Minimum and maximum detection thresholds A CCD type sensor has a quantum efficiency η_λ for a given wavelength λ, corresponding to the number of photoelectrons produced by a photon of wavelength λ impinging on the CCD. The CCD response is generally characterized by the manufacturer by the responsivity $R(\lambda)$ in V.cm^2.μJ^{-1}, giving the output voltage for a received energy at wavelength λ per unit area. The quantum efficiency is thus included in this response R. The collected signal for a photon of wavelength λ arriving on a pixel of surface $(\Delta x)^2$ is thus

$$V[\text{volt}] = R[\text{V.cm}^2.\mu\text{J}^{-1}]\frac{hc}{\lambda[\text{m}]}\frac{1}{(\Delta x)^2[\text{cm}^2]}10^6 \ . \tag{105}$$

For this signal to be detected, it must be at least higher than the darkness noise. This noise has a Gaussian distribution of r.m.s. value σ_{noise} and we postulate that the signal can be distinguished from the noise in 95% of the cases if it is higher than 2 σ_{noise}. In this case, the minimum necessary signal, corresponding to our noise floor, is:

$$NR\frac{hc}{\lambda}\frac{1}{(\Delta x)^2}10^6 \geq 2\ \sigma_{\text{noise}} \tag{106}$$

where N is the number of photons arriving on the pixel. The detection threshold is then given by the number of photons N_{noise} corresponding to the noise signal at 2 σ_{noise}:

$$N_{\text{noise}} = \frac{\sigma_{\text{noise}}\lambda(\Delta x)^2}{R\pi c\hbar 10^6} = 1.01\times 10^{19}\frac{\sigma_{\text{noise}}\lambda(\Delta x)^2}{R} \ . \tag{107}$$

By considering square pixels of size 23 μm, and taking the Thomson CCD [41] response curve, the minimum number of photons detectable per pixel is given in Table 26 for various wavelengths between 450 and 900 nm, for a noise level of 2 σ_{noise} = 0.3 mV for a 20 ms integration time. The values for λ = 200 nm are based on a Hamamatsu CCD chip, with a noise level of 9000 electrons per pixel and per second.

Table 26: Minimum and maximum detection thresholds for a pixel surface of $(\Delta x)^2 = (23\times 10^{-4}\ \text{cm})^2$ and a 20 ms integration time, corresponding to the number of noise photons at 2 σ_{noise} (minimum) and to the CCD saturation (maximum)

λ	η_λ	R	Number of photons		Corresponding energy	
		for 20 ms	Noise (20^{o}C)	Saturation	Noise	Saturation
(nm)	(%)	(V.cm^2.μJ^{-1})	per pixel	per pixel	(J/pixel)	(J/pixel)
200	62	–	290	1.0×10^6	2.9×10^{-16}	9.6×10^{-13}
450	20	5	720	8.6×10^6	3.2×10^{-16}	3.8×10^{-12}
600	40	14	340	4.0×10^6	1.1×10^{-15}	1.4×10^{-12}
850	30	14	480	5.7×10^6	1.1×10^{-16}	1.3×10^{-12}
900	20	10	720	8.6×10^6	1.6×10^{-16}	1.9×10^{-12}

To measure the profiles up to $\pm 2\ \sigma$ in width, it is necessary that the received number of photons at $2\ \sigma$ be higher than the equivalent number of photons corresponding to the noise floor given in Table 26. By assuming a Gaussian photon distribution f, the central pixel must receive approximately $f(0)/f(2\ \sigma) \simeq 8$ times more photons than the pixel at $\pm 2\ \sigma$. The signal-to-noise ratio thus obtained is equal to 1 on the pixel located at $2\ \sigma$ and represents the minimum to carry out a measurement. In practice, to ensure a safety margin, one imposes a signal-to-noise ratio S/B of 5 on the pixel located at $2\ \sigma$.

Necessary number of pixels To measure the luminosity with 10% precision, horizontal and vertical proton beam dimensions should be known to 5% precision [Eq. (6)].

Several types of errors must be considered in order to estimate the accuracy of the profile measurement. The first one is the error due to the finite number of points (called here sampling error $\Delta\sigma_1^2$) and represents the error between the exact value to measure $\sigma_{\text{theor.}}$ and the value σ_{measured} of an ideal measurement. It is then necessary to add the various errors made to the measurement itself, which we shall detail further.

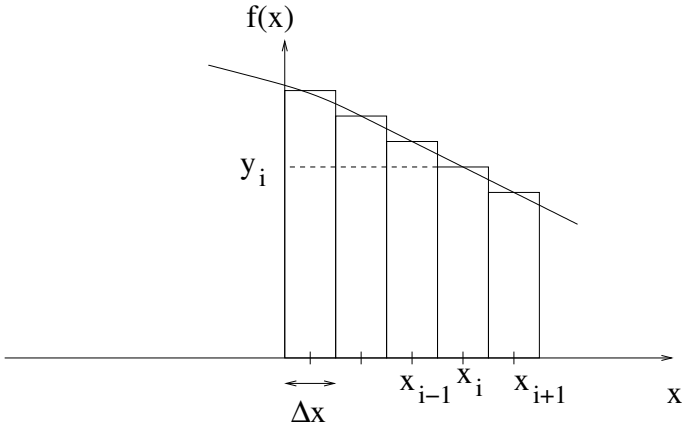

Fig. 58: Notations

The read value at the n-th pixel of dimension Δx centred in $x_i = i\Delta x$ is $y_i = \int_{x_i - \frac{\Delta x}{2}}^{x_i + \frac{\Delta x}{2}} f(u)du$ (Fig. 58). Let us consider $2N$ points (x_i,y_i). The r.m.s. value σ_{measured} of these measurements and the $\sigma_{\text{theor.}}$ theoretical r.m.s. value of the distribution $f(u)$ to be measured (supposed of zero average) are by definition:

$$\sigma^2_{\text{measured}} = \frac{\sum_{i=-N}^{N} x_i^2 y_i}{\sum_{i=-N}^{N} y_i} \qquad \sigma^2_{\text{theor.}} = \frac{\int u^2 f(u)du}{\int f(u)du} \ . \tag{108}$$

For N sufficiently large, the two denominators are equal. The $\Delta\sigma_1^2$ error made because of the discretization is written:

$$\begin{aligned} \Delta\sigma_1^2 &= \sigma^2_{\text{measured}} - \sigma^2_{\text{theor.}} \\ &= (\sigma_{\text{measured}} + \sigma_{\text{theor.}})(\sigma_{\text{measured}} - \sigma_{\text{theor.}}) \\ &\simeq 2\ \sigma_{\text{theor.}} \Delta\sigma_{\text{theor.}} \ . \end{aligned} \tag{109}$$

By introducing Eqs. (108) into Eq. (109), $\Delta\sigma_1^2$ can be expressed as:

$$\Delta\sigma_1^2 = \frac{\sum_{i=-N}^{N} x_i^2 y_i - \int u^2 f(u)du}{\int f(u)du} \quad . \tag{110}$$

By discretizing the integral over u in N intervals of width Δx and introducing the value of y_i, one obtains:

$$\begin{aligned} \Delta\sigma_1^2 &= \frac{\sum_{i=-N}^{N} x_i^2 \int_{x_i-\frac{\Delta x}{2}}^{x_i+\frac{\Delta x}{2}} f(u)du - \sum_{i=-N}^{N} \int_{x_i-\frac{\Delta x}{2}}^{x_i+\frac{\Delta x}{2}} u^2 f(u)du}{\int f(u)du} \\ &= \frac{\sum_{i=-N}^{N} \left(\int_{x_i-\frac{\Delta x}{2}}^{x_i+\frac{\Delta x}{2}} (x_i^2 - u^2) f(u)du \right)}{\int f(u)du} \quad . \end{aligned} \tag{111}$$

On each interval $[x_i - \frac{\Delta x}{2},\ x_i + \frac{\Delta x}{2}]$, it is possible to under-value u by $(x_i - \frac{\Delta x}{2})$ and to overvalue $(x_i^2 - u^2)$ by $(u\Delta x + (\frac{\Delta x}{2})^2)$. Thus:

$$\begin{aligned} \Delta\sigma_1^2 &\leq \frac{\sum_{i=-N}^{N} \Delta x \int_{x_i-\frac{\Delta x}{2}}^{x_i+\frac{\Delta x}{2}} u f(u)du}{\int f(u)du} + \frac{\sum_{i=-N}^{N} (\Delta x/2)^2 \int_{x_i-\frac{\Delta x}{2}}^{x_i+\frac{\Delta x}{2}} f(u)du}{\int f(u)du} \\ &\leq \frac{\Delta x \int u f(u)du}{\int f(u)du} + \frac{(\Delta x/2)^2 \int f(u)du}{\int f(u)du} \\ &\leq \Delta x \frac{\int u f(u)du}{\int f(u)du} + (\Delta x/2)^2 \quad . \end{aligned} \tag{112}$$

In our case f is even, thus the first term is null. The sampling error is then overvalued by:

$$\Delta\sigma_1^2 \leq \left(\frac{\Delta x}{2} \right)^2 \tag{113}$$

where Δx is the pixel size.

However, according to Eq. (109), $\Delta\sigma_1^2 \simeq 2\sigma_{\text{theor.}}\Delta\sigma_{\text{theor.}}$, therefore:

$$\frac{\Delta\sigma_{\text{theor.}}}{\sigma_{\text{theor.}}} \leq \frac{(\Delta x)^2}{8\sigma_{\text{theor.}}^2} \quad . \tag{114}$$

To obtain an accuracy of 5% on the σ value, it is thus necessary to have at least $(\Delta x)^2/8\sigma^2 \geq 0.05$, corresponding to 1.6 pixels per σ, that is to have at least 2 pixels per σ.

Minimum number of photons Owing to the darkness noise on a pixel, it is necessary to add to the sampling error, the error contribution from the measured values y_i. This noise corresponds to a random value δy_i which is added to the ideal value y_i. The random variable δy_i has a Gaussian distribution centred on 0 with the r.m.s. value σ_{noise} defined previously. To evaluate the $\delta\sigma$ error introduced by this noise on the measured σ value, we use a numerical simulation.

A random number generator adds to each y_i of the ideal Gaussian a random noise δy_i with a Gaussian distribution (Fig. 59). One then calculates the σ_i variance of the $(x_i,\ y_i + \delta y_i)$ couples. The operation is repeated for a large number of noise values, typically 10 000, to obtain the σ_i distribution

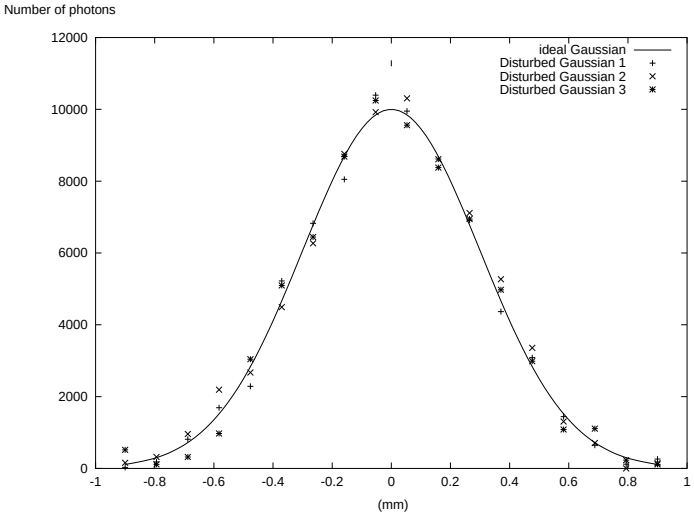

Fig. 59: Three examples of disturbed Gaussian superimposed on the ideal Gaussian

of the variances measured with the noise around the theoretical average σ value. It is then possible to calculate the $\delta\sigma$ variance of the σ_i variances which represents in fact the relative error on σ introduced by the darkness noise. While making the calculation of the σ_i variances dependent on the ideal Gaussian maximum, the points per σ number, the number of points (expressed in a number of σ) used for calculation, etc., it is then possible to study the influence of these various parameters on the σ measurement. To be able to carry out profile measurements with 5% precision in 95% of the cases, it is necessary that 2 $\delta\sigma$ remains lower than the required precision, i.e. 5%.

The Gaussian fit procedure on the $y_i + \delta y_i$ measurements, identical to that used for all the profile monitors, consists in finding the maximum, then the values on both sides of this point corresponding to 60% of this maximum. For a Gaussian curve, these two points correspond to $\pm\sigma$. By defining the retained fit level, (60%, 13% ... of the maximum), it is possible to change the number of points used. In the following, the names '1 σ, 2 σ... fit' specify the percentage of the maximum considered by the different procedures.

Initially, we shall consider profile measurements over 20 ms with the CCD described previously. To evaluate the minimum number of photons necessary to measure the profile, we place ourselves in the most unfavourable case of the noise level corresponding to 2 σ_{noise} given in Table 26, i.e. 720 photons. The random variable δy_i has in this case a Gaussian distribution of r.m.s. value σ_{noise} = 360 photons for a 20 ms integration time. Table 27 gives for 360 noise equivalent photons, the corresponding $\delta\sigma$ and 2 $\delta\sigma$ errors on the σ measurement according to the pixels per σ number, to the maximum number of photons of the distribution, and to the number of σ (corresponding in fact to the number of points) used for the Gaussian fit. Figures 60 and 61 show the evolution of the relative error with the number of photons on the central pixel for injection and collision energy.

These simulations show that one can detect a σ variation of 5% in 95% of the cases (i.e. at $\pm 2\ \delta\sigma$) with 3 pixels per σ for 6500 photons arriving on the central pixel in the most unfavourable case of darkness noise. With a fit procedure using only the top of the curve (so-called '$\pm 1\ \sigma$ fit'), it is then possible to obtain the same result with a maximum of only 1000 photons on the central pixel and 12 pixels per σ.

The preceding results correspond to cuts in the distribution. In the case of projections, the curve obtained corresponds to the sum of the pixels in one direction. Consequently, the noise contribution is averaged on the summed pixel number and is thus reduced. In addition, the CCD specifications indicate that the darkness noise can be decreased by cooling the sensor. The number of noise photons is thus

Table 27: Relative error (at 2 σ i.e. for 95% of measurements) made on the σ measurement for various parameter values, for a given temperature corresponding to $\sigma_{\text{noise}} = 360$ photons for a 20 ms integration time

Photons at central pixel	Pixels/σ	Number of σ used for the fit	$\delta\sigma$ (%)	2 $\delta\sigma$ (%)
500	12	1	4.30	8.70
500	14	1	4.00	7.90
500	21	1	3.10	6.20
500	12	2	7.20	14.40
750	12	1	3.20	6.40
1000	3	1	6.40	12.70
1000	5	1	4.30	8.70
1000	12	1	2.50	5.00
1000	12	2	4.90	9.80
3000	3	2	4.90	9.90
3000	4	2	4.10	8.20
3000	4	1	1.70	3.30
3000	12	1	0.85	1.70
4000	3	2	3.20	6.40
4000	3	1	1.50	3.00
4000	12	1	0.64	1.30
6500	2	2	3.40	6.80
6500	3	2	2.50	5.00
6500	4	2	2.00	4.00
6500	3	1	0.90	1.80
10 000	3	2	1.60	3.20
10^5	2	4	0.80	1.70
10^5	3	2	0.20	0.30
10^6	2	4	0.10	0.20
10^6	3	2	0.02	0.03

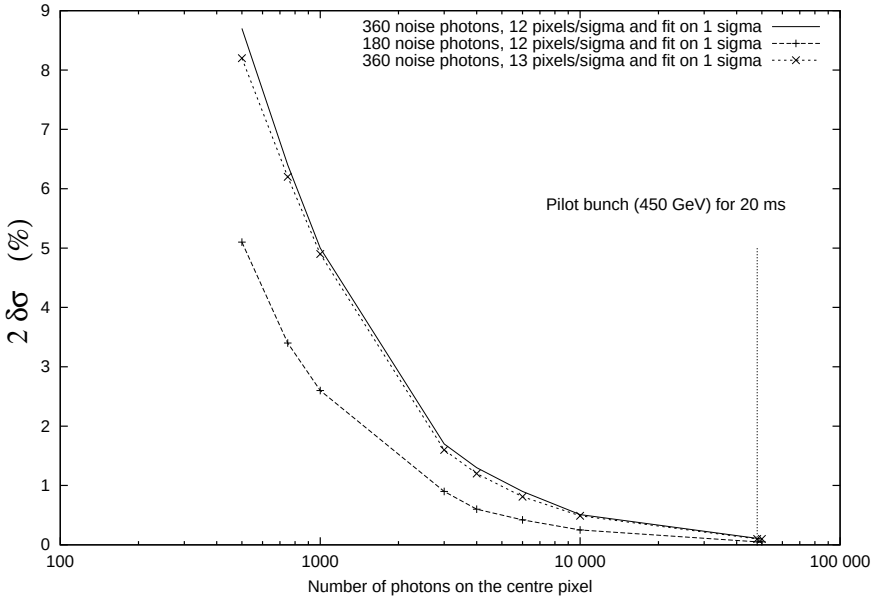

Fig. 60: Relative error (at 2 σ i.e. for 95% of measurements) on the σ according to the number of photons arriving on the central pixel for various fitting types adapted to the 450 GeV proton energy and for various values of σ_{noise}.

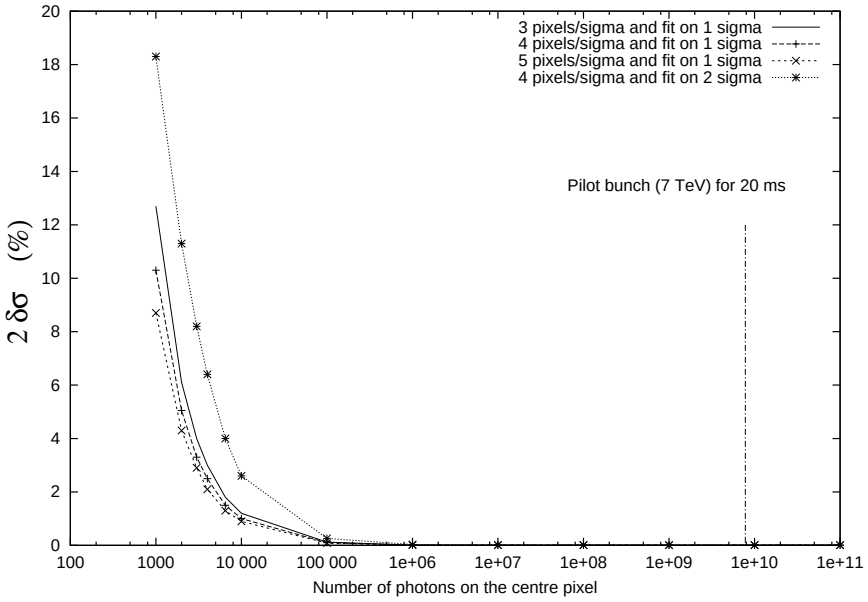

Fig. 61: Relative error (at 2 σ i.e. for 95% of measurements) on the σ according to the number of photons arriving on the central pixel for various fitting types adapted to the 7 TeV proton energy and for various values of σ_{noise}.

divided by 2 every 8 degrees. The preceding evaluations are thus very conservative.

In conclusion, with an additional factor 10 for taking into account the losses due to the transmission, to be able to measure profile variations of 5%, we shall consider two points of operation corresponding to two extreme beam sizes:

1. at 450 GeV: 12 pixels per σ and 5000 photons on the central pixel in 20 ms with a cooling of 8 degrees
2. at 7 TeV: 3 pixels per σ and 20 000 photons on the central pixel in 20 ms.

Minimum energy per proton To allow the direct comparison with the results of the preceding section, it is interesting to convert this minimum number of photons on the central pixel to the energy in joules per proton which it is necessary to collect on the whole CCD.

For the first operation point planned for 450 GeV, one needs 5000 photons on the central pixel with 12 pixels per σ. The central pixel (with the size σ/12) receives in this case, according to the density of probability chart [42], 0.11% of the maximum amplitude and one thus needs 4.5×10^6 photons on the whole CCD. In the same way, for the second operation point, the 20 000 photons on the central pixel with 3 pixels per σ correspond to 3.8 $\times 10^6$ photons on the whole (the central pixel receiving 1.7% of the maximum). The photons having a 2 eV average energy (corresponding to λ = 621 nm), the total number of photons which it is necessary to collect in 20 ms of integration time is converted to a minimum energy of 1.5×10^{-12} J allowing profile measurement at 450 GeV and 3.8×10^{-13} J at 7 TeV. The collected intensity being proportional to the integration time and the number of protons in the beam, dividing this total energy by the number of protons in the bunch to be measured (pilot or nominal), one gets the energy per proton necessary with an integration time of 20 ms, Table 28. Finally, to allow a direct comparison with the energy values given in Section 6, dividing again by the number of turns done during 20 ms, one gets the averaged minimum energy per proton and per turn allowing one to measure the profile within 5% in 20 ms.

Table 28: Minimum energy per proton necessary to allow the 5% precision profile measurement with a pilot bunch (5×10^9 protons) or with a nominal bunch (10^{11} protons) according to the considered integration time

Proton energy (TeV)	Fit procedure	Minimum energy per proton (J) for 20 ms (225 turns)		per turn	
		5×10^9 p	10^{11} p	5×10^9 p	10^{11} p
0.45	12 pixels per σ	2.9×10^{-22}	1.5×10^{-23}	1.3×10^{-24}	6.4×10^{-26}
7	3 pixels per σ	7.5×10^{-23}	3.8×10^{-24}	3.3×10^{-25}	1.7×10^{-26}

For the study in turn-by-turn mode, it is necessary to use an MCP in front of the CCD in order to select one turn and to amplify the signal. In this case, it is necessary to consider the whole chain of transmission to evaluate the darkness noise per turn. The values provided by the manufacturers are generally averaged over a given integration time whereas to obtain the values of noise in turn-by-turn mode, it would be necessary, to be rigourous, to know the distribution density of the noise. Because of the lack of existing measurements of these data, it is necessary to make additional assumptions or to measure them experimentally. A specific study is then necessary to be able to draw conclusions for the turn-by-turn measurements.

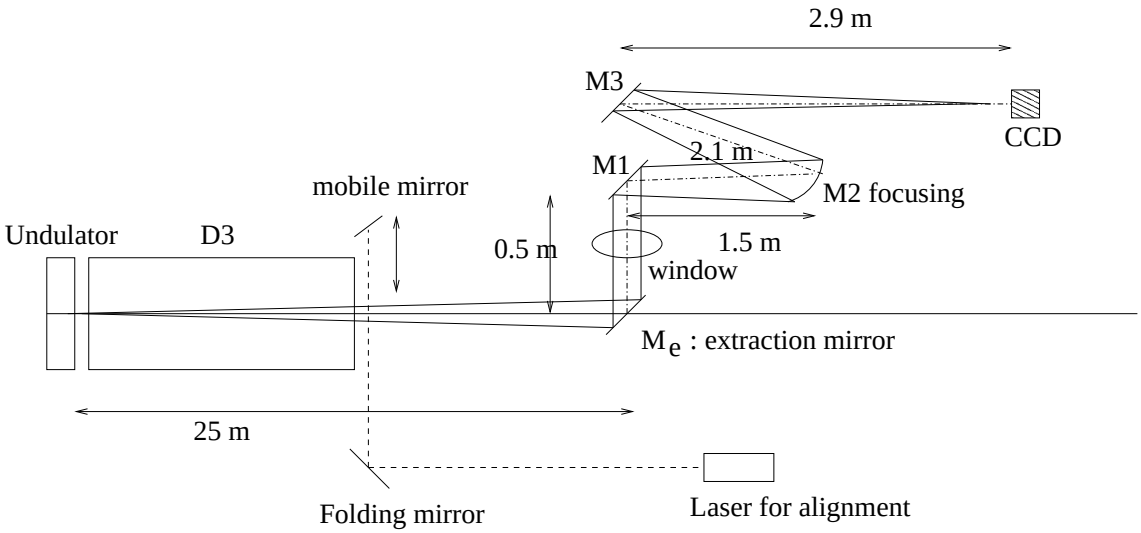

Fig. 62: Dimensions of the optical system, based on that of LEP

7.1.2 Optical set-up

To allow the profile measurement over the whole LHC energy range, a very wide wavelength range is used, going from 200 nm (low limit fixed by the separation window and a front-illuminated CCD) to 1000 nm (high limit fixed by the CCD spectral acceptance range). This working range results in the use of a catoptrical system to avoid the chromatic aberrations introduced by a system of lenses. Moreover, to avoid the deformation of the image due to the reflective surface imperfections, the mirrors selected must have a surface quality better than $\lambda/10$.

To guarantee the precision desired on the $\sigma_{\mathrm{H,V}}$ measurement, one needs 3 pixels per $\sigma_{\mathrm{H,V}}$ for the smallest beam dimensions. The beam being the smallest at 7 TeV in the horizontal plane, optics must thus make it possible to obtain 3 pixels per σ in the image plane for $\sigma_{\mathrm{H,7\,TeV}} = 0.28$ mm in the object plane, that is to say a $G = 0.19$ magnification with a pixel size smaller than 20 μm. With a $p = 27$ m object distance and a focusing mirror available from the LEP telescope (M2) [43] with a 4.167 m focal length, the M2 to image distance is $p' = 5$ m (Fig. 62). The dimensions of this optical layout correspond to those of the LEP telescope. It thus appears possible to re-use it to limit the cost of the LHC diagnostics system.

The folding mirror M3 (Fig. 62) is motorized to centre the image on the detector. From the experience gained on LEP, an alignment system based on a calibration source is also planned. A laser, located close to the telescope emits a light beam toward D3 (Fig. 62). This light is deflected in the vacuum chamber by a set of two mirrors with a 45 degree angle placed at the D3 exit and then sent to the extraction mirror. The second mirror is mobile (Fig. 62) so that it can be introduced into the vacuum chamber in the alignment phase and then withdrawn. The telescope can thus be aligned by using this calibration source. Table 29 recapitulates the dimensions of the optics.

The telescope is equivalent, from the point of view of geometrical optics, to a lens of 4.167 m focal length (the M2 mirror, Fig. 62), with a square aperture, corresponding to the extraction mirror M_e, located 2 m upstream from the focusing element, see Appendix D.

7.2 Image formation

With an ideal optical system, the image of a point is a point. But finite dimensions of the various components introduce degradations of the image, thus replacing the geometrical point image by a distribution of amplitude called Point Spread Function (PSF). By transposing these results to synchrotron radiation [12], the angular distribution of the synchrotron radiation plays the role of an amplitude opening. Thus, even in

Table 29: Dimensions of the optics. The subsystem made up of the laser, the folding mirror, and the mobile mirror is used only for alignment of the telescope mirrors

Entrance undulator–M_e distance	23 m
M_e–M2 distance	2 m
M2–CCD distance	5 m
Magnification	0.19
Focal length	4.167 m (available)
Entrance pupil	Extraction mirror 50×50 mm^2

the absence of any finite physical opening, it is necessary to determine the PSF of a point source in order to evaluate the resolution of the optical system. In this part, we shall consider the monochromatic radiation emitted by a proton in order to simplify calculations and to accelerate the numerical simulations. If the wavelength range of the detector is extended, it is sufficient to integrate over the range considered.

The telescope is equivalent to a simple optical device (diaphragmed lens). But the image collected is that of the light source itself and not that of a lit-up object. The image formation is thus not done within a traditional framework. First of all, the SR source characteristics mix the concept of incoherent illumination (between the various beam particles) and coherent illumination (passage through the longitudinally extended source by one particle). Moreover, the object presents a variable longitudinal range, modifying the focusing point during the energy ramp. After having explained the source characteristics, the next paragraph introduces the role of the various telescope components in the image formation.

7.2.1 Synchrotron light specificity

Polarized light We saw previously that synchrotron light is polarized. With polarizers, it is possible to separate the horizontal (σ) and vertical (π) components of the emitted electric field and thus of the corresponding amplitude distributions:

$$\vec{F}(y,z) = \vec{F}_\sigma(y,z) + \vec{F}_\pi(y,z) \ . \tag{115}$$

The scalar diffraction theory can thus be applied to each component [12, 44] and the total intensity distribution collected in the image plane is the sum of the intensities of each component:

$$I(y,z) = |\vec{F}(y,z)|^2 = |\vec{F}_\sigma(y,z)|^2 + |\vec{F}_\pi(y,z)|^2 \ .$$

Each component can thus be studied independently. In the following, in order to simplify the notations, we shall omit to specify the considered component (σ or π) when the equations can apply to both of them.

'Incoherent' light The synchrotron radiation source is comprised of two essential elements: the particles in the beam and a set of magnetic elements. If the whole beam is considered, each particle emits radiation, in the wavelength range of interest, independently of the other particles. In this sense, the synchrotron radiation is known as 'incoherent'. The resulting intensity distribution $D(y,z)$ in the detector plane is the convolution of the spatial distribution of the protons $O(y,z)$ brought back in the image plane, with the single proton intensity distribution $I(y,z)$:

$$D(y,z) = O(y,z) * I(y,z) \ .$$

The two $O(y,z)$ and $I(y,z)$ distributions are independent. In this case, the r.m.s. values of the various distributions are related by:

$$\sigma^2_{D(y,z)} = \sigma^2_{O(y,z)} + \sigma^2_{I(y,z)} \ . \tag{116}$$

Thus, by measuring the spatial distribution of the intensity in the image plane and by knowing the intensity distribution emitted by a proton brought back in the image plane (i.e. by taking into account the optical system magnification), it is possible to deduce the spatial distribution of the particles in the beam.

'Coherent' light If the light source is a set of several magnetic elements, $F(y, z)$ is the 'coherent' sum of the contributions of each distinct part of the source, following the method described in Section 4. The longitudinal range of the source introduces into the angular distribution of the amplitude a phase structure determining the image formation. It is no longer possible to think in terms of transmitted intensity and it is necessary to use wave front propagation.

The method used to calculate the amplitude distribution in the detector plane is based on the Fourier optics formalism [45] implemented in the numerical code SRW (Synchrotron Radiation Workshop) [39].

7.2.2 Propagation through a diaphragm

According to Huygens' principle [46], all the space points reached by a wave front behave like secondary sources of spherical waves. The envelope of these waves constitutes the wave front. The construction of this envelope at any time makes it possible to represent the light propagation and to build the image of an object. A physical aperture (i.e. a diaphragm) placed along the trajectory of the wave limits its spatial range, and thus cancels the contributions of some sets of secondary waves. The wave front envelope is then deformed compared to in-vacuum propagation, creating a light dispersion.

So, to evaluate the diffraction effect in the LHC SR monitor, it is necessary to take into account two contributions: the presence of a diaphragm corresponding to the finite dimensions of the extraction mirror cutting the distribution at 450 GeV, and the limited angular distribution of the synchrotron radiation creating diffraction whose effect is essentially felt at 7 TeV, when the proton beam size is smallest. Indeed, in the case of synchrotron radiation, the angular opening of the light cone is about $1/\gamma = 0.1$ mrad at 7 TeV. This corresponds to a natural limitation of the wave range which creates diffraction even in the absence of physical openings [12].

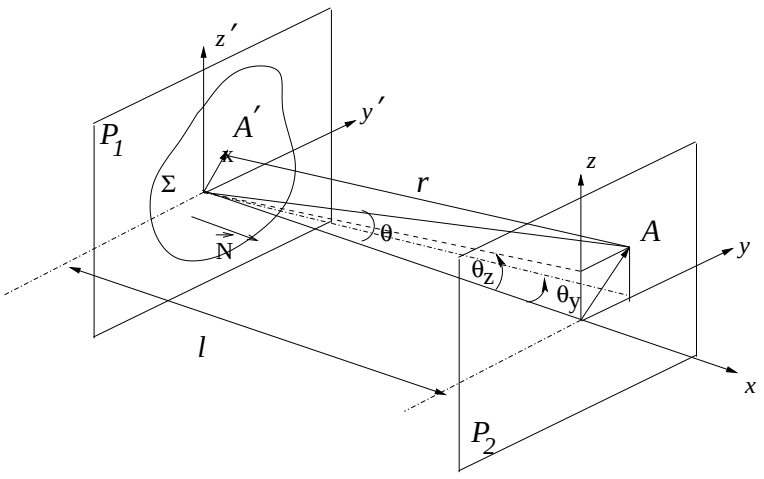

Fig. 63: Propagation between two planes P_1 and P_2.

Propagation between two planes The Huygens–Fresnel principle [46] states that the wave amplitude $F(A)$ received in a point A of co-ordinates (y, z) in the P_2 image plane is the superposition of the

spherical waves emitted by secondary sources $F(A')$ located in the P_1 plane (Fig. 63). For a given wavelength λ (monochromatic light), one has:

$$F(A) = \frac{1}{j\lambda} \iint_{-\infty}^{+\infty} F(A') \frac{\exp\,(j\frac{2\pi}{\lambda}r)}{r} \cos\theta ds \tag{117}$$

where A' is a point of co-ordinates (y', z') in the P_1 plane, l is the distance between the two planes, $\cos\,\theta = \frac{l}{r}$ is the angle between the vector $\vec{N}$ normal to the P_1 plane and the vector $\vec{r}$ joining A to A'. The distance r is given by:

$$r = \sqrt{l^2 + (y - y')^2 + (z - z')^2} \ . \tag{118}$$

The presence of a diaphragm is limiting the spatial range of the wave front in the aperture plane. Mathematically, this is equivalent to limite the spatial integration on the Σ opening or to introduce into the integral a pupillary function $\mathcal{P}(y', z')$ such as $\mathcal{P}(y', z') = 1$ for $(y', z') \in \Sigma$ and $\mathcal{P}(y', z') = 0$ elsewhere. Equation (117) is then written:

$$\begin{aligned} F(y,z) &= \frac{1}{j\lambda} \iint_{\Sigma} F(A') \frac{\exp\,(j\frac{2\pi}{\lambda}r)}{r} \cos\theta ds \\ &= \frac{1}{j\lambda} \iint_{-\infty}^{+\infty} \mathcal{P}(y', z') F(A') \frac{\exp\,(j\frac{2\pi}{\lambda}r)}{r} \cos\theta ds \ . \end{aligned} \tag{119}$$

For the denominator r of Eq. (119), the approximation $r \simeq l$ is sufficient for the majority of the current applications. On the other hand, the term in the exponential, expressing a phase delay between the secondary waves, is sensitive to r variations of the order of λ. Two areas are generally distinguished according to the retained terms in the series expansion of r. When the observation point is sufficiently close to P_1 so that all the phase terms appearing in Eq. (120) have the same order of magnitude, one speaks then about 'near field diffraction', or *Fresnel diffraction*. Conversely, when the observation distance is sufficiently large compared to Σ opening sizes so as to neglect the variations of the quadratic term $(y'^2 + z'^2)$ over the opening, one speaks about 'far field diffraction', or *Fraunhofer diffraction*.

Fresnel diffraction In the Fourier optics approximation when considering propagation directions close to the optical axis, r can be developed as:

$$r \simeq l \left(1 + \frac{1}{2} \left(\frac{y - y'}{l} \right)^2 + \frac{1}{2} \left(\frac{z - z'}{l} \right)^2 \right) \tag{120}$$

where l is the distance between the two planes (Fig. 63). Equation (119), with $\cos\,\theta \simeq 1$, can thus be rewritten in the form:

$$F(y,z) = \frac{\exp\,(j\frac{2\pi}{\lambda}l)}{jl\lambda} \iint_{\Sigma} F(y', z') \exp\left[j\frac{\pi}{\lambda l} \left((y - y')^2 + (z - z')^2 \right) \right] dy' dz' \ . \tag{121}$$

By separating the phase terms to keep under the integral sign only those dependent on the integration variables, Eq. (121) looks like the Fourier transform of the product of the field amplitude on the Σ opening by a quadratic phase term:

$$F(y,z) = \frac{e^{(j\frac{2\pi}{\lambda}l)} e^{(j\frac{\pi}{\lambda l}(y^2+z^2)}}{jl\lambda} \iint_{\Sigma} \left[F(y', z') e^{\left(j\frac{\pi}{\lambda l}(y'^2+z'^2)\right)} \right] e^{\left(-j\frac{2\pi}{\lambda l}(yy'+zz')\right)} dy' dz' \ . \tag{122}$$

Fraunhofer diffraction In the case of far field diffraction, if l satisfies the additional condition [45]:

$$l \gg \frac{\pi(y'^2 + z'^2)}{\lambda}$$

the quadratic phase term in $y'^2 + z'^2$ is roughly equal to 1 over the whole aperture and its variations can be neglected. Equation (121) is written then:

$$F(y,z) = \frac{e^{(j\frac{2\pi}{\lambda}l)}e^{(j\frac{\pi}{\lambda l}(y^2+z^2))}}{j\lambda l}\iint_{-\infty}^{+\infty} F(y',z')e^{(-j\frac{2\pi}{\lambda l}(yy'+zz'))}dy'dz' \quad . \tag{123}$$

To evaluate the profile measurement accuracy, only the relative distribution of intensity in the image plane is necessary, i.e. the square module of $F(y,z)$. In this case, as $|e^{i\xi}|^2 = 1\ \forall\xi$, the phase terms in front of the integral sign can be omitted. The far field diffraction considers that the waves which are superimposed in the image plane result from parallel rays. It establishes a relation between the spatial frequencies defined by $u = \frac{y}{\lambda l}$ and $v = \frac{z}{\lambda l}$ and the director cosine of the observation direction defined by $\zeta_y = \frac{y}{l}$ and $\zeta_z = \frac{z}{l}$. The term in the exponential can then be interpreted as the phase (or optical path) difference between the parallel rays coming from two different points of the diffracting surface. By introducing the spatial frequencies into Eq. (123), the diffracted amplitude calculation appears in the form of a spatial Fourier transform:

$$F(u,v) = C\iint_{-\infty}^{+\infty} F(y',z')e^{(-j2\pi(y'u+z'v))}dy'dz' \tag{124}$$

where $C = \frac{\exp\,(j\frac{2\pi}{\lambda}l)\ \exp\,(-j\pi\lambda l(u^2+v^2))}{j\lambda l}$.

For the particular case of our optical system, the dimensions of the diaphragm (the extraction mirror) are 50×50 mm^2. Thus, for a wavelength λ = 500 nm, and a radius $y'_{\max} = z'_{\max} = 25$ mm, the simplifying but also very constraining Fraunhofer approximation applies for $l \gg 2\pi(2.5 \times 10^{-2})^2/(500 \times 10^{-9}) = 7800$ m! To calculate the diffraction effects with sufficient precision, this approximation can thus not be retained and it is necessary to keep the quadratic phase term $y'^2 + z'^2$, i.e. Eq. (122) and this is what was done in the following.

7.2.3 Action of a lens on a wave front

A lens is commonly built from material of refraction index higher than that of air. In the 'thin lens' approximation, the entry co-ordinate is the same as the exit one. In this case, while crossing the lens an incidental wave undergoes a phase distribution modification in the incidental plane proportional to the lens thickness crossed at each point of this plane. The phase delay introduced by the lens is written:

$$\phi(y,z) = \frac{2\pi}{\lambda}n\Delta(y,z) + \frac{2\pi}{\lambda}[\Delta_0 - \Delta(y,z)] \tag{125}$$

where $\Delta(y,z)$ represents the lens thickness and is a function of the curvature radii R_1 and R_2 of each face and of incidence co-ordinates (y,z) on the lens [45], Δ_0 being the lens thickness on the optical axis. In an equivalent way, the lens action on a wave front is represented by the multiplication of the complex amplitude by a phase transformation term $t_l(y,z) = \exp\,(j\phi(y,z))$. By considering only the wave portion close to the lens axis (paraxial approximation), the $\Delta(y,z)$ function is written in the approximate form:

$$\Delta(y,z) \simeq \Delta_0 - \frac{y^2+z^2}{2}\left(\frac{1}{R_1} - \frac{1}{R_2}\right) \quad . \tag{126}$$

Defining the focal length f of a lens by

$$\frac{1}{f} = (n-1)\left(\frac{1}{R_1} - \frac{1}{R_2}\right) \tag{127}$$

and neglecting the constant phase term, the expansion of Eq. (125) results in the expression of the lens action as the multiplication of the incidental amplitude on the lens by a quadratic dephasing term t_l:

$$t_l(y,z) = \exp\left(-j\frac{\pi}{\lambda f}(y^2+z^2)\right) \quad . \tag{128}$$

7.3 Method with operators

When the number of lenses and diaphragms increases in the optical system considered, the total calculation of the light propagation through the whole system becomes complicated in the integral form. It thus seems to us interesting to introduce the method suggested in Ref. [45] which defines a set of operators characterizing the various transformations associated with the optical elements.

7.3.1 Definition of operators

The operators are defined by their parameter between square brackets [ ] and the function on which they act are written between braces { }.

Multiplication by a quadratic phase term , c being the reverse of a length:

$$\mathcal{Q}[c]\{U(y,z)\} = e^{j\frac{\pi}{\lambda}c(y^2+z^2)}U(y,z) \tag{129}$$

Propagation over a distance l with (y_2,z_2) the co-ordinates after propagation:

$$\mathcal{R}[l]\{U(y_1,z_1)\} = \frac{1}{j\lambda l}\iint_{-\infty}^{+\infty} U(y,z)e^{j\frac{\pi}{\lambda l}((y_2-y_1)^2+(z_2-z_1)^2)}dy_1dz_1 \quad . \tag{130}$$

Here the Fresnel propagation equation is recognized.

Fourier transform

$$\mathcal{F}\{U(y,z)\} = \frac{1}{\sqrt{2\pi}}\iint_{-\infty}^{+\infty} U(y,z)e^{-j(uy+vz)}dydz \quad . \tag{131}$$

Scaling by a constant b

$$\nu[b]\{U(y,z)\} = b^{-1/2}U(by,bz) \quad . \tag{132}$$

Passage through an aperture Σ by defining $P(y,z) = 1$ for (y,z) in Σ and 0 elsewhere,

$$\mathcal{D}[\Sigma]\{U(y,z)\} = P(y,z)U(y,z) \quad . \tag{133}$$

The wave front propagation through an optical system is represented by the product in the opposite order of propagation of the corresponding operators. Various relations between the operators as detailed in Ref. [45] will simplify the complex expressions of propagation by reducing the operator chain. For example:

$$\mathcal{Q}[\frac{1}{d}]\nu[\frac{1}{\lambda d}]\mathcal{F}\mathcal{Q}[\frac{1}{d}] = \mathcal{R}[d] \quad . \tag{134}$$

7.3.2 Application to an SR monitor

To illustrate the use of the operators in a simple case, let us consider the configuration of Fig. 64 representing the synchrotron radiation monitor. The total propagation operator from the point source S to the image point I is written:

$$\mathcal{S} = \mathcal{R}[x_2]\mathcal{Q}\left[-\frac{1}{f}\right]\mathcal{R}[l]\mathcal{D}[\Sigma]\mathcal{R}[x_1-l] \quad . \tag{135}$$

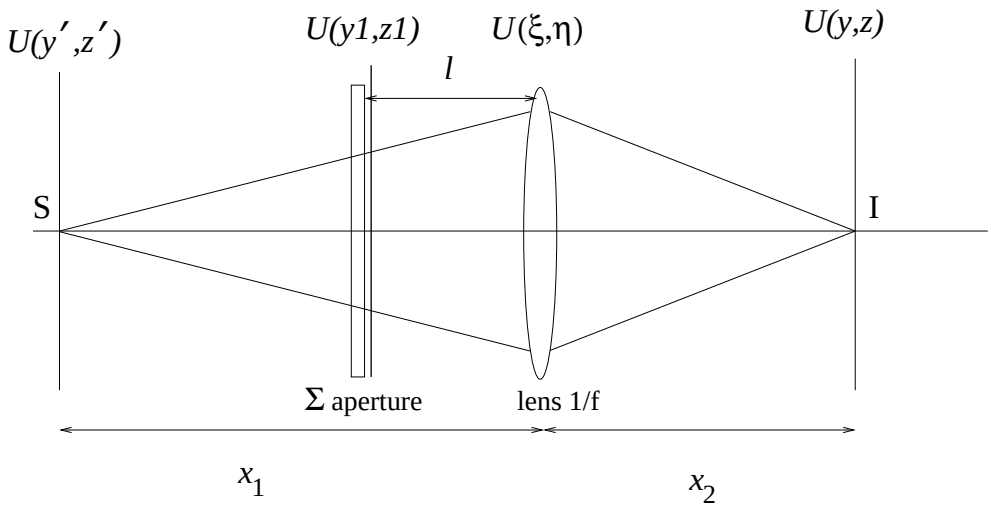

Fig. 64: Geometry equivalent to the telescope: an object located in the plane S is observed through a diaphragm and a lens in a plane I

By moving along the chain from the right-hand side to the left, one finds the propagation over a distance (x_1-l), the crossing of a diaphragm (equivalent of the extraction mirror), the propagation over the distance l, the crossing of the lens of focal length f, and finally the last propagation over a distance x_2.

The numerical program Zgoubi and the analytical methods developed in Section 4 are used for calculating the intensity distribution in the extraction mirror plane. This is why we distinguish two areas: propagation from the source S to the P_1 plane right behind the diaphragm represented by the $\mathcal{S}_1$ operator, then propagation from the P_1 plane till the detector plane (called 'image plane' although no particular relation is supposed a priori between x_1 and x_2), represented by the $\mathcal{S}_2$ operator. By calling $U(y', z')$ the amplitude distribution in the source plane; $U(y_1, z_1)$ that in the P_1 plane; and $U(y, z)$ that in the image plane, one has the relations:

$$U(y_1, z_1) = \mathcal{S}_1\{U(y', z')\} = \mathcal{D}[\Sigma]\mathcal{R}[x_1 - l]\{U(y', z')\} \tag{136}$$

$$U(y, z) = \mathcal{S}_2\{U(y_1, z_1)\} = \mathcal{R}[x_2]\mathcal{Q}\left[-\frac{1}{f}\right]\mathcal{R}[l]\{U(y_1, z_1)\} \ . \tag{137}$$

Propagation through the telescope In integral notation, Eq. (137) is put in the form:

$$U(y,z) = \frac{e^{j\frac{\pi}{\lambda x_2}(y^2+z^2)}}{\lambda^2 x_2 l} \iint_{-\infty}^{+\infty} \left\{ \iint_{-\infty}^{+\infty} U(y_1,z_1) e^{j\frac{\pi}{\lambda l}(y_1^2+z_1^2)} e^{j\frac{\pi}{\lambda}\left(\frac{1}{l}+\frac{1}{x_2}-\frac{1}{f}\right)(\xi^2+\eta^2)} \times e^{-j\frac{2\pi}{\lambda}\left[\left(\frac{y}{x_2}+\frac{y_1}{l}\right)\xi+\left(\frac{z}{x_2}+\frac{z_1}{l}\right)\eta\right]} dy_1 dz_1 \right\} d\xi d\eta \tag{138}$$

where $U(y_1, z_1)$ is the amplitude distribution in the plane right behind the aperture, and (ξ, η) are the co-ordinates in the lens plane.

If one supposes moreover that the lens has an opaque finite support, the integral in $d\xi d\eta$ is limited to the Σ_{lens} aperture of this support. Thus, starting from the amplitude distribution in the plane immediately behind the entrance pupil of the system, it is possible to obtain the intensity pattern in any plane located at the distance x_2. The main difficulty is then to evaluate $U(y_1, z_1)$ in the particular case of the synchrotron light source.

Various common simplifications Equation (138) can be simplified by considering certain particular cases. First of all, if one is interested in the intensity in the image plane, then the phase distribution term in $(y^2 + z^2)$ in the image plane can be omitted.

In addition, if the object is a point source located in the (y_0, z_0) position in the (y_1, z_1) plane, then $U(y_1, z_1) = \delta(y_0, z_0)$ and

$$\iint_{-\infty}^{+\infty} U(y_1, z_1) e^{j\frac{\pi}{\lambda l}(y_1^2+z_1^2)} dy_1 dz_1 = e^{j\frac{\pi}{\lambda l}(y_0^2+z_0^2)} \ . \tag{139}$$

Again, if one is interested only in the intensity distribution in the image plane, the quadratic phase term in $(y_0^2 + z_0^2)$ can be omitted. Equation (138) is reduced then to:

$$U(y, z) \simeq \frac{1}{\lambda^2 x_2 l} \iint_{\Sigma_{\text{lens}}} e^{j\frac{\pi}{\lambda}\ \frac{1}{l}+\frac{1}{x_2}-\frac{1}{f}\ (\xi^2+\eta^2)} e^{-j\frac{2\pi}{\lambda}\left[\ \frac{y}{x_2}+\frac{y_0}{l}\ \xi+\ \frac{z}{x_2}+\frac{z_0}{l}\ \eta\right]} d\xi d\eta \ . \tag{140}$$

An additional simplification appears if x_1 and x_2 satisfies the lens law $\frac{1}{x_1} + \frac{1}{x_2} = \frac{1}{f}$, i.e. when the optics is focused on the source point. The quadratic phase term in $(\xi^2 + \eta^2)$ disappears then from the integral and one finds an expression of the Fourier transform type. Thus, if the optical system carries out the image of a point object with x_1 and x_2 satisfying the lens law of geometrical optics, the intensity distribution in the image plane is the Fraunhofer diffraction pattern of the $\mathcal{P}(\xi, \eta)$ lens support, with $\mathcal{P}(\xi, \eta) = 1$ for (ξ, η) inside Σ_{lens}, the traditional result of the diffraction calculation [46].

However, the particular characteristics of the synchrotron light source, detailed in the following, do not allow using these simplifications.

7.3.3 Characteristics of the synchrotron light source

Extended object In the case of the chosen synchrotron light source for the diagnostics, Section 6, the object has a finite and 'variable' longitudinal range with the proton beam energy, in the detector spectral range. At 450 GeV, only the undulator emits sufficient light to be detected (Table 17). The source is thus 75 cm long. At 7 TeV, the source is comprised of the dipole edge effect. It is thus 15 cm long and located closer to the extraction mirror. For a fixed longitudinal position of the extraction mirror, the source–focusing mirror distance thus varies also with energy. These are the two relatively simple cases. On the other hand for intermediate beam energies, the source is in fact a source doublet, approximately 2 m long. For the image formation, the phase distribution in the wave front is thus the determining factor. The use of the intensity distribution on the extraction mirror is not sufficient and it is necessary to determine the amplitude distribution in the extraction mirror plane.

Use of the analytical models In the particular cases of injection energy and collision energy, the undulator and the edge effect can be compared to point sources and the lens law[8] is applicable. It thus seems possible to use the simplified relation (140). In the case of the undulator, one has an analytical model to describe the amplitude distribution [Eq. (40)]. In the same way, if the angular spectral energy densities emitted by the two sources can be modelled with analytical formulas, by using the interference formulas given in Section 4, it is possible to calculate the amplitude distribution in the extraction mirror plane. However, the edge radiation model developed in the same section is valid only in high-frequency mode, i.e. at low proton energy, where it is in fact the undulator which prevails in the emission. Analytical calculation must initially be preceded by the determination of a simple model of the fringe field allowing the integral calculation (140).

As for the numerical program Zgoubi used until now, it does not provide the phase term necessary to derive integral (140). To be able to study the case which seems a priori the most critical (at the

[8]This supposes a modification of x_2 of a few tens of centimetres to focus optics on the real source in each case.

collision energy), and in order to be efficient, we chose to use additional numerical tools available in other laboratories.

Numerical calculation The intensity distribution calculation in the image plane and the study of the role of the focusing point at intermediate proton energies must be carried out starting from the general expression (138):

$$U_{\sigma,\pi}(y,z) = \frac{e^{j\frac{\pi}{\lambda x_2}(y^2+z^2)}}{\lambda^2 x_2 l} \iint_{\Sigma_{\text{lens}}} \left\{ \iint_{\Sigma_{\text{diaphragm}}} \tilde{E}_{\sigma,\pi}(y_1,z_1) e^{j\frac{\pi}{\lambda l}(y_1^2+z_1^2)} \right. \\ \left. \times\, e^{j\frac{\pi}{\lambda}\left[\frac{1}{l}+\frac{1}{x_2}-\frac{1}{f}\right](\xi^2+\eta^2)} e^{-j\frac{2\pi}{\lambda}\left[\frac{y}{x_2}+\frac{y_1}{l}\;\xi+\;\frac{z}{x_2}+\frac{z_1}{l}\;\eta\right]} dy_1 dz_1 \right\} d\xi d\eta \tag{141}$$

where $\tilde{E}_{\sigma,\pi}(y_1,z_1)$ is the Fourier transform of the electric field received on the diaphragm (or extraction mirror). For quadruple integral evaluation, we have used a simple numerical calculation. Taking into account the lens and diaphragm apertures, the variation of the exponential terms 'oscillates' widely over the integration interval. Thus, to have sufficient precision, one needs a high number of integration points to ensure the integral convergence. A rapid estimate shows that for 8 mm openings, one needs 7×10^8 integration steps to calculate the intensity in one point. Initially, the adopted solution is to limit the integration field to 2×2 mm^2. But in this case, the field distribution is comparable to a spherical wave and one finds the Point Spread Function of a point source. More elaborate numerical methods are thus necessary to calculate precisely the intensity in the image plane for the source comprised of the undulator and the dipole edge.

Thus, the analytical study at particular energies as well as the implementation of a simple numerical method adapted to our monitor case would require the development of additional tools. To be able to carry out a complete study of the diffraction and depth of field effects over the whole energy range, this implementation was forsaken and replaced by the use of an existing code, developed at ESRF for electrons, SRW (Synchrotron Radiation Workshop) [39]. The code is based on the propagation method described previously [47].

7.4 Optical analysis of the SR monitor

The results presented in this part were obtained with the SRW code. The beam used is a 'filament' beam[9], i.e. of null emittance, making it possible to represent the radiation emitted by one particle. Moreover, the horizontal component, generally the least diffracting one and corresponding to the fluxes given in the previous section, is the only one considered. Lastly, the radiation studied is always monochromatic. To obtain the real images in the detector plane, it is thus necessary to integrate the distributions over the different wavelengths of the considered acceptance range and to convolute the result by the spatial distribution of the particles [Eq. (7)] which cannot be done with the numerical code used.

7.4.1 Use of SRW with protons

Although initially intended for use with electrons, SRW gives the results sought with protons with the help of the introduction of corresponding scale factors[10] for the energy and the magnetic fields used in the LHC. To guarantee a good starting point, a systematic comparison of intensities collected at the extraction mirror, obtained with SRW on the one hand, and Zgoubi on the other hand, was made. The two most representative cases are presented below.

[9] The beam has the LHC beam nominal current, but all the particles pass on the same trajectory; the emittance effects are neglected and the image is obtained with a simple convolution [Eq. (7)].

[10] A proton with energy E in the magnetic field B is simulated by an electron with the energy $E \times m_e/m_p$ in a $B \times m_e/m_p$ magnetic field, where m_e/m_p is the ratio of the proton and electron rest masses, i.e. about 1/1836.

At 7 TeV Figures 65 show the intensity emitted by the undulator–D3 source at the collision energy, simulated with Zgoubi at the left, and SRW at the right. At 7 TeV, the main source is the D3 dipole. The radiation of the centre of D3 becomes comparable with that of the edges, corresponding to the two peaks in the $\phi \simeq \pm\frac{\alpha}{2} \simeq \pm 0.8$ mrad direction.

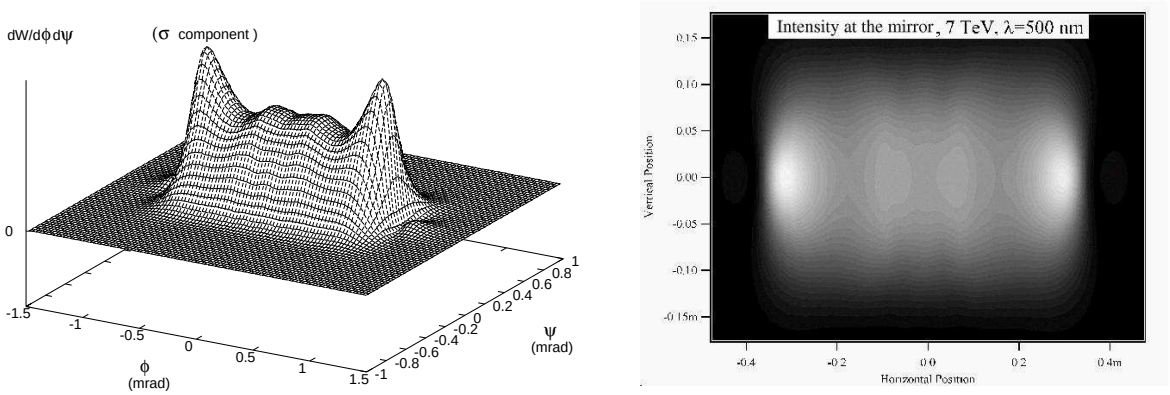

Fig. 65: Intensity emitted (horizontal component) for a proton energy of 7 TeV and $\lambda = 500$ nm, with a distance $d = 1$ m between the two sources, simulated with Zgoubi (on the left) and SRW (on the right).

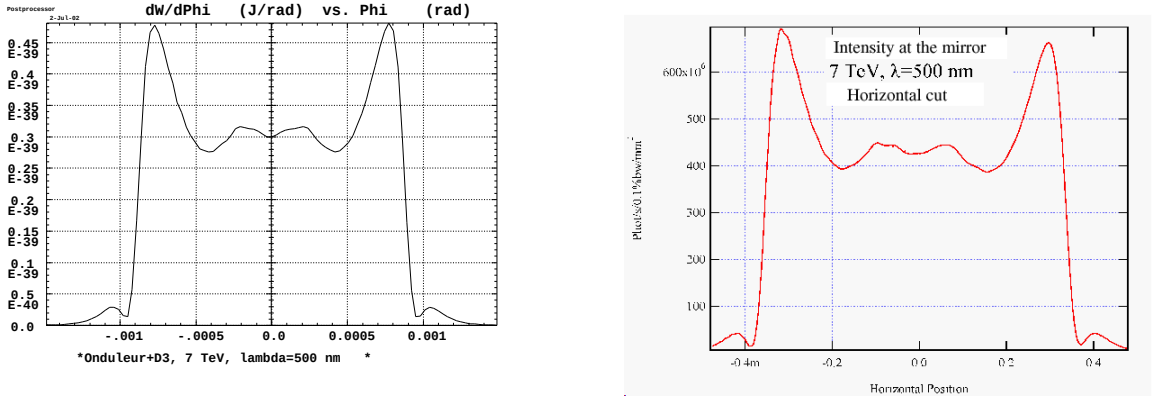

Fig. 66: Cuts in the horizontal plane of the intensity emitted (horizontal component) for a proton energy of 7 TeV and $\lambda = 500$ nm, with a distance $d = 1$ m between the two sources, simulated with Zgoubi (on the left) and SRW (on the right) for a source-to-mirror distance of 400 m.

On the cuts in the horizontal plane (Figs. 66) one notices that the peaks of the edge radiation do not correspond exactly to the physical position of the magnet edge, but are at $\phi = \pm(\frac{\alpha}{2} - \frac{1}{\gamma})$, with a secondary peak at $\phi = \pm(\frac{\alpha}{2} + \frac{1}{\gamma})$ [Eqs. (51) and (52)]. These results correspond to those already presented in Section 4.2, in the limit of validity of the low-frequency model (Fig. 17). Note that the identical end peak intensities in the Zgoubi case (left) comes from the assumption of a constant observation distance r, Eq. (26).

At 1 TeV Figures 67 show the intensity collected in the extraction mirror plane at 1 TeV and λ = 500 nm simulated with the two numerical codes Zgoubi and SRW when the source is made up of the undulator and the D3 dipole separated by 1 m. The first code, Zgoubi, uses the far field approximation neglecting the $1/r^2$ term in the expression of the electric field emitted by the particle [Eq. (13)] while the second, SRW, calculates the intensity distribution including the near field component [47] [Eq. (11)]. Both methods reveal the same source characteristics, so the approximation in the Zgoubi code that keeps the

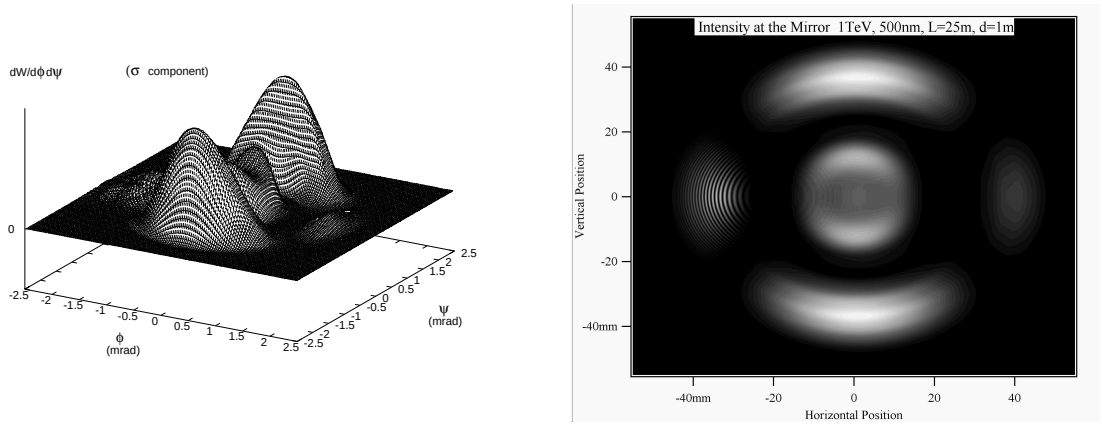

Fig. 67: Intensity emitted (horizontal component) by 1 TeV protons, λ = 500 nm, with a distance $d = 1$ m between the two sources, simulated with Zgoubi (on the left) and with SRW (on the right).

distance r between the source and the observer constant all along the range of the source to calculate the module of the received electric field is acceptable.

First of all, the central lobe is comprised of the interference between the emission in the undulator axis direction and the emission at the dipole entrance edge. The intensity is thus modulated with a period depending on the distance between the two sources (Section 4.3). Secondly, the ring, corresponding to the emission direction of the λ = 500 nm wavelength at 1 TeV, i.e. θ = 1.6 mrad according to Eq. (38), is modulated by the non-symmetrical angular distribution term of Eq. (42) [$F_u(\theta, \varphi)$ defined page 44]. It appears as four different intensity peaks, more intense in the vertical plane than in the horizontal plane. Lastly, the θ = 1.6 mrad direction corresponds to the D3 dipole deflection (Section 6.1.4). The dipole exit edge emits in the same direction as the undulator ring corresponding to a λ = 500 nm wavelength. They thus interfere with an oscillation period varying linearly with the distance separating the two sources. One thus observes interference black fringes with a frequency higher than that observed on the central lobe corresponding to the interference between the entrance edge and the undulator (Fig. 68). The method developed in Section 4.3 shows that the intensity modulation due to the interference between the two sources varies as sin $(\frac{2\pi c}{\lambda}T)$ where T is the crossing time of the straight section of length d and of the D3 dipole of length L, that is to say according to Eqs. (64) and (B.3):

$$T = \frac{L}{2\gamma^2 c}\left[1 + \gamma^2(\phi^2 + \psi^2) + \frac{K^2}{3}\right] + \frac{d}{2\gamma^2 c}\left[1 + \gamma^2(\phi^2 + \psi^2)\right] \tag{142}$$

where $K = \alpha\gamma/2$ is the dipole deflection parameter, and the co-ordinates (ϕ, ψ) are defined in Fig. 7. The $\phi(n)$ angular positions of black fringes are defined by solving in ϕ the condition:

$$\frac{2\pi c T}{\lambda} = n 2\pi \tag{143}$$

where n is an integer. The numerical application for $\lambda = 500$ nm and n of the order of 30 for the ϕ region of Fig. 68, gives an angular distance $\phi(n) - \phi(n-1)$ between the interference rings of 0.035 mrad, corresponding for 25 m to an inter-fringe distance of 0.9 mm, in agreement with Fig. 68.

The agreement between the two programs using two different approximations is very good in our case and it will thus be noticed that the near field method is not necessary for our application.

7.4.2 Qualitative approach

With the wave front propagation method, it is possible to calculate numerically the intensity distribution in any plane and to obtain the Point Spread Function (PSF) in the detector plane. Before studying

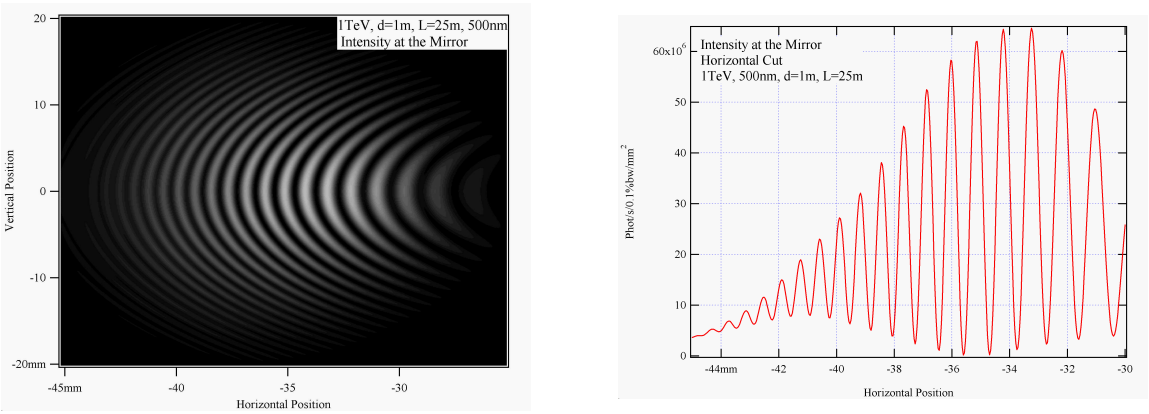

Fig. 68: Angular spectral energy density (zoom of Fig. 67) and cut in the horizontal plane for λ = 500 nm, with $d = 1$ m (Fig. 69), and 1 TeV proton energy, horizontal component.

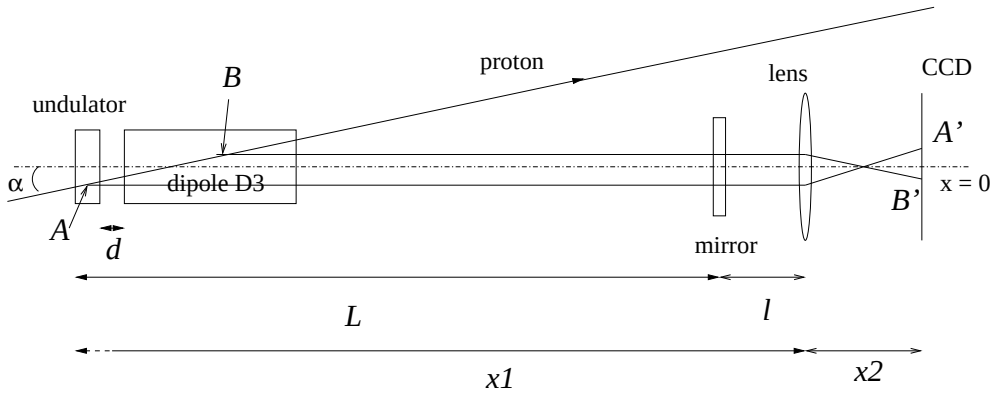

Fig. 69: Configurations and notations used for the numerical simulations of image formation. According to the chosen focusing point, A or B for example, the image position, A' or B', is different in the detector plane.

more precisely the influence of the various parameters in order to choose an optimal configuration, the presentation of the plots obtained for three representative energies introduces some significant results.

The configuration used for simulations, the optical equivalent of the telescope, is shown in Fig. 69. The SRW propagation calculation can be carried out only for small angles, of the order of a mrad. To remain in this approximation with the mirror sizes considered, it was decided to centre the optical elements on the $x = 0$ axis. The filament beam trajectory thus enters the undulator with an angle $\alpha = 0.7$ mrad. The optical axis and the undulator radiation axis are thus shifted by this α angle. The consequence of this shift on the synchrotron radiation is simply a shift of the emitted fundamental wavelengths. Indeed, the beam 'sees' in place of the real spatial period λ_u, its projection on the α direction, i.e. λ_u cos α which represents a negligible variation. Moreover, the x_2 distance (Fig. 64, page 71) can be modified allowing for the choice of the trajectory point focused onto the detector plane, for a given lens. The change of the object point on which the optics is focused, illustrated by points A and B on Fig. 69 added to the angular shift α is at the origin of a change of position of the corresponding images (A' and B' on Fig. 69). This is visible on the following figures resulting from SRW simulations.

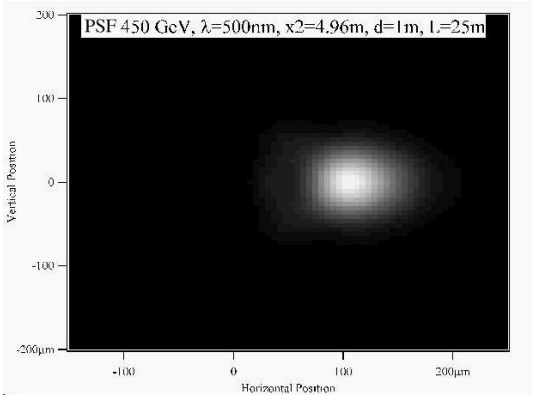

Fig. 70: Intensity in the detector plane for a 450 GeV energy, λ = 500 nm, optics being 'focused' on the undulator exit (x_2 = 4.96 m), collected with a 50×50 mm^2 mirror at $L = 25$ m, whose edge is at $15\ \sigma_{H,450\ \mathrm{GeV}}$ from the proton beam axis (the edge effect contribution to the illumination is negligible).

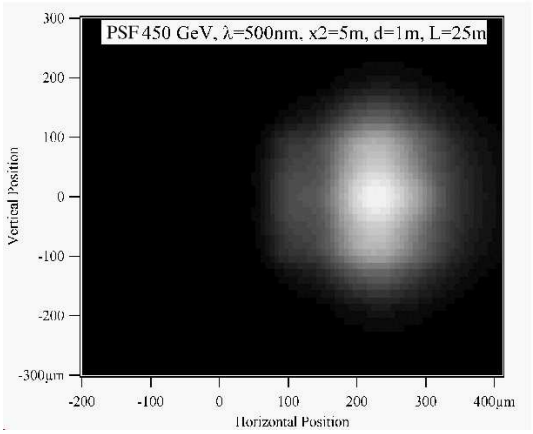

Fig. 71: Intensity in the detector plane for a 450 GeV energy, λ = 500 nm, optics being 'focused' on the D3 dipole entrance (x_2 = 5 m), collected with a 50×50 mm^2 mirror at $L = 25$ m, whose edge is at $15\ \sigma_{H,450\ \mathrm{GeV}}$ from the proton beam axis.

At the injection energy At 450 GeV, the intensity produced by the D3 dipole is negligible compared with that produced by the undulator (Table 17, page 51). The source is thus comprised only of the undulator. For the λ = 500 nm wavelength close to the fundamental, the angular distribution of the radiation is a lobe centred on the undulator symmetry axis. The image of this source obtained by focusing the optics on the undulator exit (x_2 = 4.96 m, for a 4,167 m focal length) is also a peak to which the diffraction effect is added (Fig. 70). If the optics is focused in order to observe a point corresponding to the D3 dipole entrance (Fig. 71) one finds the same image spot, but widened.

At the collision energy At 7 TeV, the source is comprised of the D3 dipole, edge and interior. We saw in Section 4.2.1 that in the low-frequency approximation (i.e. for observation frequencies lower than the inverse of the pulse duration), the edge radiation, instead of being a cone centred on the physical edge position, breaks up into two cones of different intensities centred on $\pm 1/\gamma$ on both sides of the edge. The lens recombination of this radiation gives normally a point. However, the mirror position does not make it possible to collect the totality of the dipole edge radiation distribution in this case [Fig. 72 corresponding to Fig. 57-(c) to be compared with Fig. 66]. The image recombination is thus performed

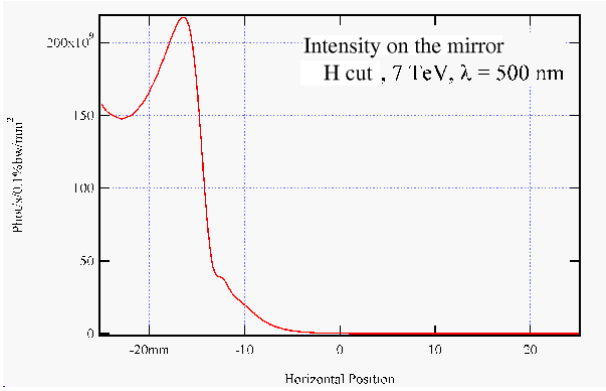

Fig. 72: Cut in the horizontal plane of the intensity collected on the extraction mirror whose edge is at $\sigma_{H,450\text{ GeV}}$ = 18 mm from the proton beam axis, for λ = 500 nm and a proton energy of 7 TeV.

from truncated angular distributions, resulting in pronounced diffraction effects (Figs. 73 and 74). One finds the same types of figures as for 450 GeV, but this time the focusing point is on the entry of D3 (Figs. 73 and 74).

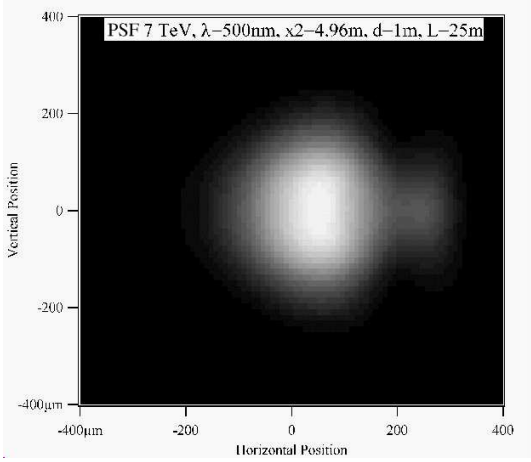

Fig. 73: Intensity in the detector plane for a 7 TeV beam energy, λ = 500 nm, optics being focused on the undulator exit (x_2 = 4.96 m), collected with a 50×50 mm^2 mirror at $L = 25$ m. The mirror edge is at 15 $\sigma_{H,450\text{ GeV}}$ from the proton beam.

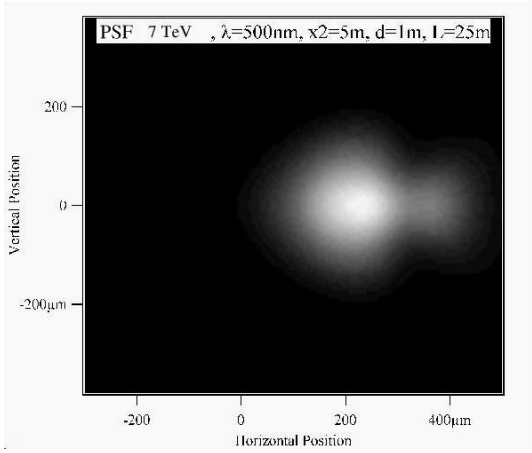

Fig. 74: Intensity in the detector plane for a 7 TeV beam energy, λ = 500 nm, optics being focused on the D3 dipole entrance (x_2 = 5 m), collected with a 50×50 mm^2 mirror at $L = 25$ m. The mirror edge is at 15 $\sigma_{H,450\text{ GeV}}$ from the proton beam.

At 1 TeV The angular structure of the radiation source at this intermediate energy is quite complex. It is made up of a peak centred on the optical axis containing the undulator and the D3 edge effect contributions, and of four peaks located on a ring of angular radius θ = 1.6 mrad, corresponding to the λ = 500 nm wavelength emission direction (Fig. 67). Figure 75 compared with Figure 67 shows the part of the total intensity distribution collected by a 50×50 mm^2 mirror at the distance $L = 25$ m whose edge is at 15 $\sigma_{H,450\text{ GeV}}$ from the proton beam axis. The cone centred on the α direction (that is to say -17.5 mm at 25 m) is the coherent superposition of the radiation emitted by the undulator and the D3 edge located at the distance d. Because of the eccentric mirror position with respect to the undulator radiation emission axis, only a fraction of the ring corresponding to the 500 nm wavelength is collected:

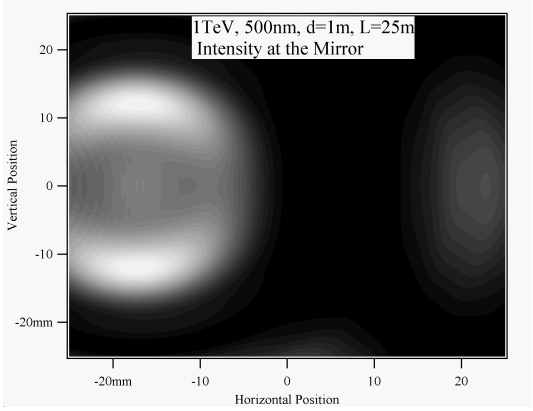

Fig. 75: Intensity collected (σ component) on the 50×50 mm^2 extraction mirror at $L = 25$ m whose edge is at $15\ \sigma_{H,450\ \mathrm{GeV}}$ from the proton beam axis, for a 1 TeV energy and λ = 500 nm. Only an eccentric square of 50×50 mm^2 is taken from Fig. 67 corresponding to a square with 60 mm sides.

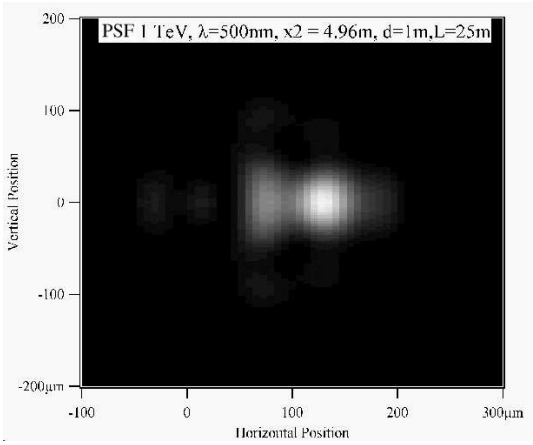

Fig. 76: Intensity in the detector plane for a 1 TeV energy, λ = 500 nm, with the optics focused on the undulator exit, collected with a 50×50 mm^2 mirror at the $L = 25$ m distance whose the edge is at $15\ \sigma_{H,450\ \mathrm{GeV}}$ from the proton beam axis.

the two lobes appearing in the vertical plane on Fig. 67 are outside the mirror angular acceptance and thus disappear on Fig. 75. In the same way, only a very small portion from the lobe centred at 35 mm in the horizontal plane (Fig. 67) is collected by the mirror (Fig. 75). During the phase recombination by the lens, the symmetrical part of this lobe with respect to the emission axis is eliminated. One then sees appearing on the left of the central peak (image inversion) a second very attenuated peak corresponding to the part of the ring collected.

The images obtained in various image planes corresponding to different focusing points are represented in Figs. 76, 77 and 78. According to the focusing point, contributions to the central peak coming

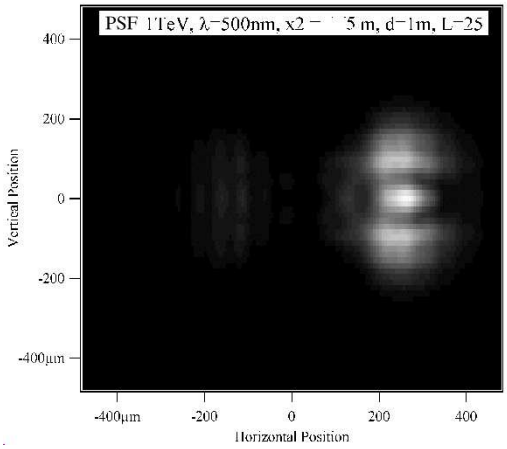

Fig. 77: Intensity in the detector plane for an energy of 1 TeV, λ = 500 nm, with the optics focused on the D3 edge, collected with a 50×50 mm^2 mirror at $L = 25$ m whose edge is at $15\ \sigma_{H,450\ \mathrm{GeV}}$ from the proton beam axis.

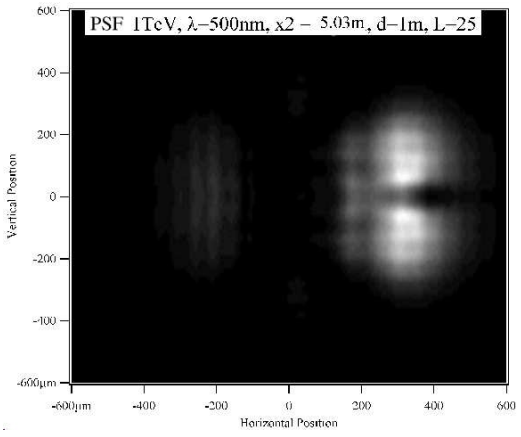

Fig. 78: Intensity in the detector plane for an energy of 1 TeV, λ = 500 nm, with the optics focused in the middle of D3, collected with a 50×50 mm^2 mirror at $L = 25$ m whose edge is at $15\ \sigma_{H,450\ \mathrm{GeV}}$ from the proton beam axis.

from the two components of the source are more or less diluted. The shape of this lobe (i.e. the number and the width of local maxima) thus varies with the focusing distance.

7.4.3 Study of the influence of the various parameters

Although our detector optics is simple, it is possible to adjust various parameters in order to optimize the performance, in particular by limiting the diffraction and depth of field effects. This section presents the studies carried out to choose the configuration giving the best space resolution, i.e. the smallest PSF.

Influence of λ Intensity distribution calculations in the detector plane depend on the observation wavelength. In the case of the monitor, the spectral ranges of the CCD and intensifiers used are relatively broad (between 200 and 900 nm). It is thus possible, either to integrate across a wide range to 'smooth out' the effects observed in monochromatic light, or on the contrary to choose a narrow range around an optimal wavelength to minimize the diffraction effects. Table 30 presents the r.m.s. sizes of the PSF horizontal cut, brought back in the object plane, as a function of the proton beam energy for several wavelengths (Figs. 79, 80 and 81).

Table 30: r.m.s. width of the PSF horizontal cut brought back to the object plane for various wavelengths. The $50\times$ 50 mm^2 extraction mirror is $L = 25$ m upstream from the undulator entrance, the focusing mirror is $l = 2$ m from the extraction mirror and the detector is x_2 from the focusing mirror. The proton beam size in the object plane is shown in the last column for comparison.

Focusing point: undulator exit				
Proton energy (TeV)	r.m.s. width of the PSF H cut (mm)			r.m.s. beam size object plane (mm)
	λ = 200 nm	λ = 500 nm	λ = 900 nm	
0.45	0.064	0.15	0.20	1.12
1.00	0.078	0.19	0.35	0.75
7.00	0.210	0.52	0.91	0.28

Table 30 makes it possible to check a traditional result of diffraction calculations: the diffraction effect decreases with the wavelength. However, the fundamental wavelength emitted by the undulator at 450 GeV is 620 nm. The intensity emitted away from this wavelength is much lower (Fig. 79 in relative scale). The optimal wavelength from the point of view of the spatial resolution is the smallest possible. However, from the point of view of the collected signal level, it is preferable to work with wavelengths close to fundamental as long as the radiation of the undulator is detectable. Then, when the D3 edge becomes dominating, one improves the resolution by decreasing the wavelength to the minimum allowed by the detector's spectral acceptance.

Influence of the choice of the focusing point (depth of field) We showed that between 1 and 2 TeV, the radiation is produced by equivalent contributions of the undulator and of the D3 dipole edge (Table 17). The optical system thus makes in this case the image of a longitudinally extended source $\overline{AB} = a$.

While calling A_i and B_i the respective images of the extreme points of the sources A and B, located respectively at the distances p_A and p_B from the lens (Fig. 82) and by supposing the optics focused on point A, the geometrical image of point B in the plane of A_i is not a point but a disk of radius r_A:

$$r_A = \overline{A_i B_i} \tan u_i \ . \tag{144}$$

By using the relations of geometrical optics between A and $\overline{a_i b_i}$, one obtains the relation [46]:

$$r_A = \frac{a u_i f^2}{p_A p_B} \tag{145}$$

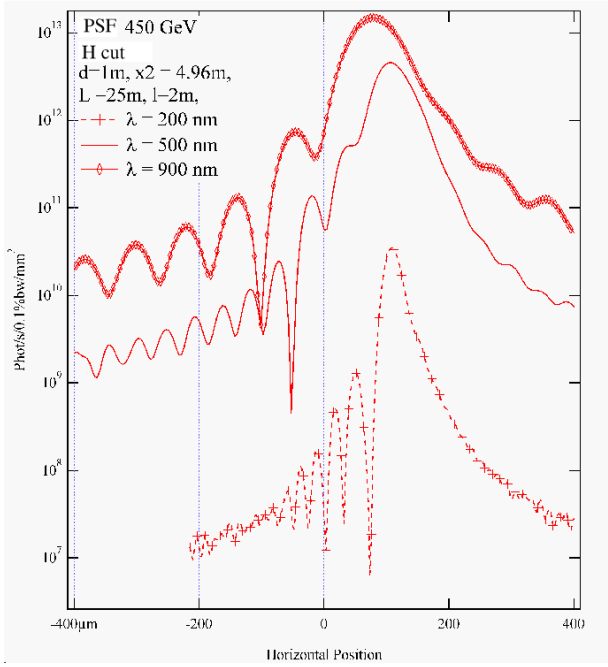

Fig. 79: Comparison for various wavelengths of the PSF horizontal cuts in the detector plane at 450 GeV for the undulator and the D3 magnet (negligible)

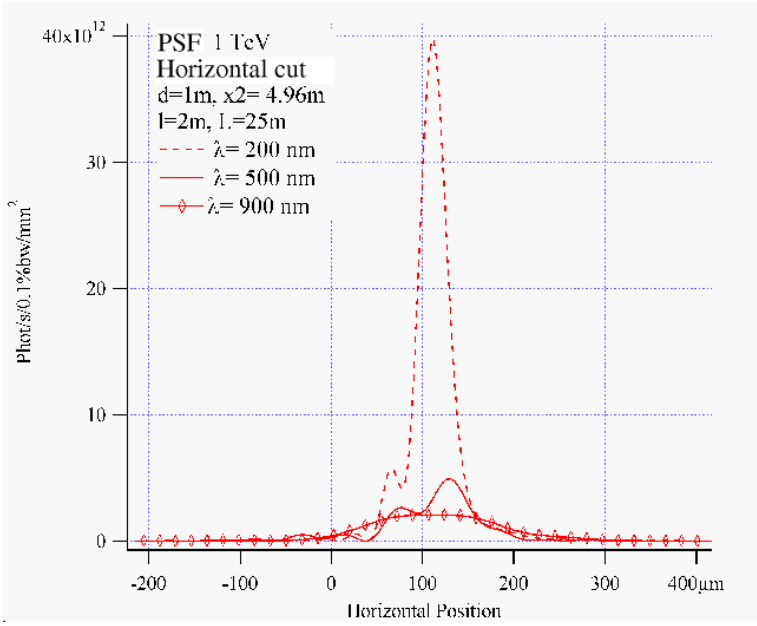

Fig. 80: Comparison for various wavelengths of the PSF horizontal cuts in the detector plane at 1 TeV for the undulator and the D3 magnet (equal contribution to the illumination)

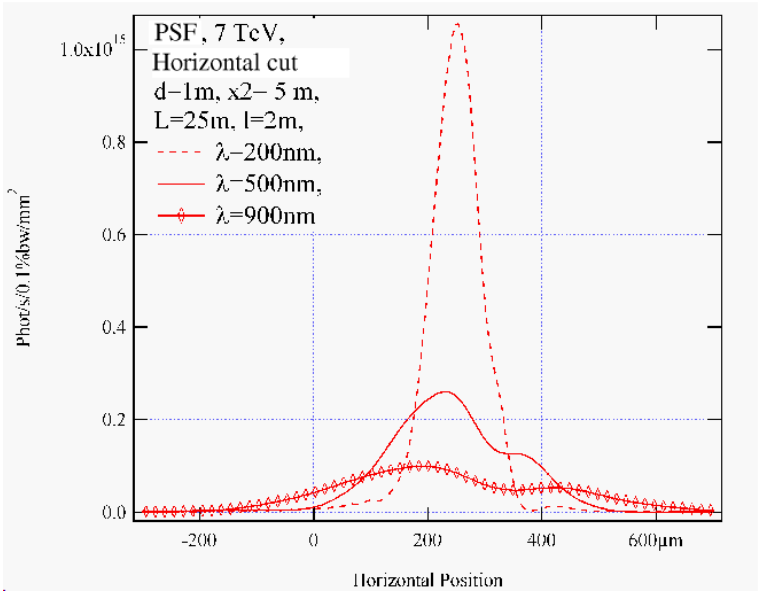

Fig. 81: Comparison for various wavelengths of the PSF horizontal cuts in the detector plane at 7 TeV for the undulator (negligible) and the D3 magnet

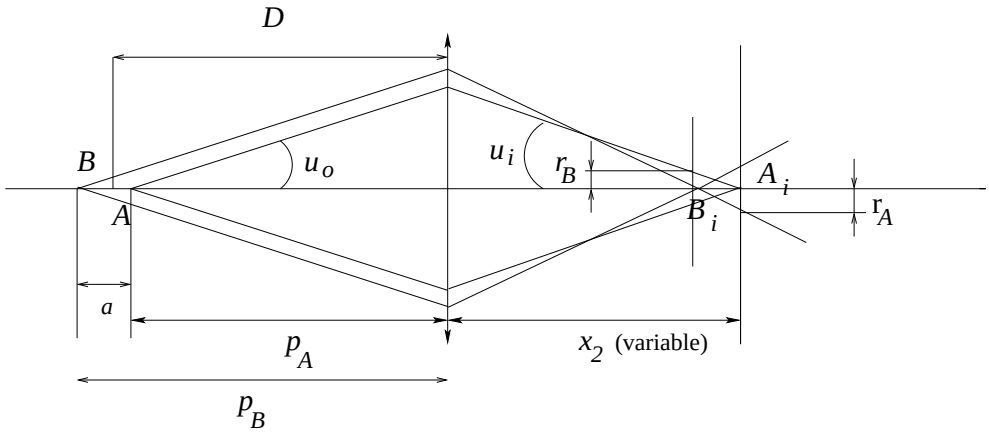

Fig. 82: Depth of field. A_i is the image of A and B_i that of B

where f is the focal length of the lens. Thus, the spot image radius increases with the emission angle[11] and with the length a. The radius r_A is null in the case of a point source located in A corresponding to $a = 0$.

The optimal focusing distance D is obtained by equalizing the radii r_A and r_B calculated for the two extreme focusing positions corresponding to the object distances p_A and p_B (Fig. 82). By applying the conjugate Newton formulas [46], one shows that D is given by:

$$D = \frac{2\, p_A p_B}{p_A + p_B} \quad . \tag{146}$$

In the case of the synchrotron radiation source comprised of the undulator and D3, a is about 2 m and p_B is the distance x_1 = 27 m. To study the depth of field effect, we varied the detector position x_2 between the points B_i and A_i. That is equivalent to varying optically the observed point source (called here 'focusing point') between the two physical limits A and B of the object. Table 31 presents the variation of the size of the horizontal cut of the PSF obtained by this source sweeping between the undulator entry and the D3 entry, that is to say approximately 2 m.

Table 31: r.m.s. value of the PSF horizontal cut in the detector plane and brought back to the object plane for various focusing points. The 50×50 mm^2 extraction mirror is 25 m upstream from the undulator entrance, the focusing mirror is 2 m from the extraction mirror.

λ = 500 nm $d = 1$ m			r.m.s. size			
			In the image plane		In the object plane	
Proton energy (TeV)	x_2 (m)	G	PSF H cut (mm)	Proton beam (mm)	PSF H cut (mm)	Proton beam (mm)
0.45	4.92	0.18	0.039	0.200	0.22	1.12
0.45	4.96	0.19	0.028	0.210	0.15	1.12
0.45	5.00	0.20	0.068	0.220	0.34	1.12
0.45	5.03	0.21	0.096	0.240	0.46	1.12
1.00	4.92	0.18	0.040	0.135	0.22	0.75
1.00	4.96	0.19	0.038	0.142	0.20	0.75
1.00	5.00	0.20	0.043	0.150	0.22	0.75
1.00	5.03	0.21	0.067	0.157	0.32	0.75
7.00	4.92	0.18	0.099	0.050	0.55	0.28
7.00	4.96	0.19	0.105	0.053	0.55	0.28
7.00	5.00	0.20	0.103	0.056	0.52	0.28
7.00	5.03	0.21	0.100	0.059	0.48	0.28
7.00	5.08	0.22	0.111	0.013	0.50	0.28

Figures 83 and 84 present the comparison of horizontal PSF sizes for various focusing points for 450 GeV and 7 TeV proton beam energy. In both cases, the source is a quasi point-like one. Thus, the spot size is minimal when the optics is focused on the real source position: on the undulator at 450 GeV and on the D3 edge at 7 TeV. In addition, the radiation cone opening u_i is smaller with high energy (u_i = 0.13 mrad) than with low energy (u_i = 2 mrad) and, in agreement with relation (145), the spot image widening due to defocusing induced by the depth of field over the source length a is thus more sensitive at 450 GeV than at 7 TeV. For the injection energy and u_i = 2 mrad, the PSF is 3.5 times broader

[11] Related to the angle u_i by the Abbe sine condition in air $\overline{A_0 B_0}$ sin $u_0 = \overline{A_i B_i}$ sin u_i.

while focusing on the D3 edge (x_2 = 5.03 m) than while focusing on the undulator exit (x_2 = 4.96 m), but widening remains acceptable in all the cases when compared with the beam size. On the other hand at 7 TeV, when the beam size is the smallest, widening is only 12% and remains negligible with respect to the diffraction effect (at this wavelength, 90% of PSF widening compared to the real beam size).

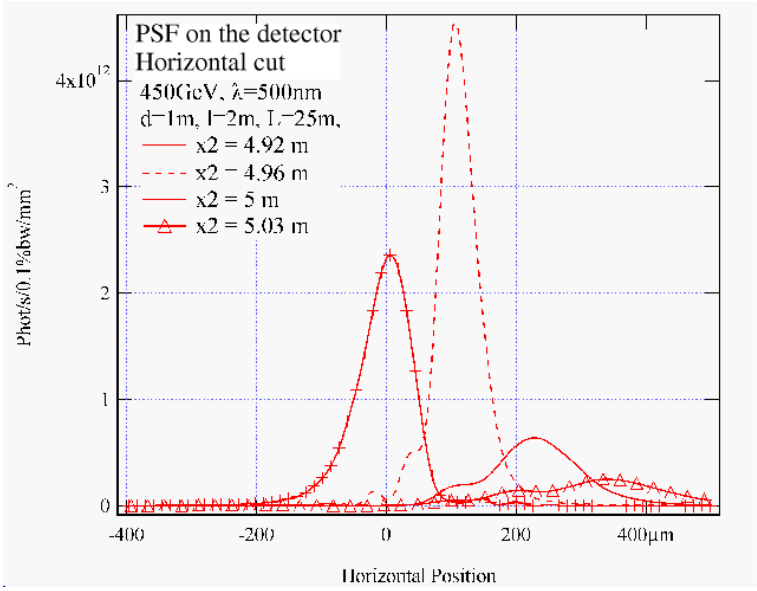

Fig. 83: Comparison for various focusing points of the PSF horizontal cuts in the detector plane at 450 GeV proton energy and for λ = 500 nm

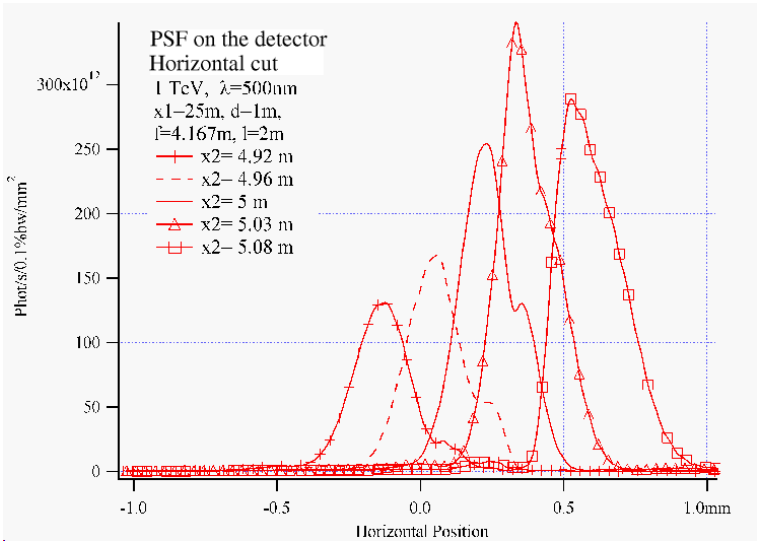

Fig. 84: Comparison for various focusing points of the PSF horizontal cuts in the detector plane at 7 TeV proton energy and for λ = 500 nm

Figure 85 presents the same comparison carried out at 1 TeV. At this energy, the effective source length is a = 2 m. With p_B = 27 m, one finds an optimal focusing distance of $D = 25.8$ m, corresponding to the undulator exit, as can be seen in Table 31.

To minimize the depth of field effects throughout the beam energy range, it is necessary to envisage modifying the focusing point, i.e. a longitudinal movement of the detector of about 5 cm corresponding to the sweep of the source between the undulator exit and the dipole entrance. However, since the effect

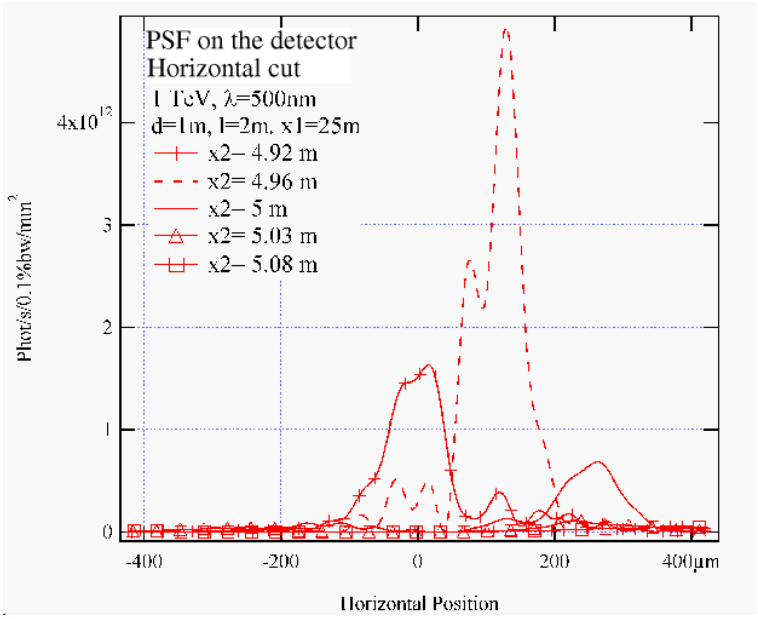

Fig. 85: Comparison for various focusing points of the PSF horizontal cuts in the detector plane at 1 TeV proton energy and for λ = 500 nm

is significant at low energy, where the beam size to be measured is not critical, one can focus the optics on the D3 edge. The image broadening introduced at 450 GeV compared to the beam size is less than 14%.

Influence of the size of the extraction mirror At 450 GeV, the light cone has an angular opening larger than the acceptance of the extraction mirror. One thus collects only a part of the angular distribution and the cut in the angular spectral distribution creates diffraction, that is the effect of a diaphragm. It is thus the position of the mirror edge that determines the widening of the spot image. However, at this energy, the proton beam size is sufficiently large that the PSF widening due to the diffraction effect is not limiting in resolution.

At 7 TeV, on the other hand, the opening of the light cone is smaller than the mirror acceptance and should thus be the limiting factor. However, the positioning of the mirror edge at 15 $\sigma_{H,450\text{ GeV}}$ from the proton beam axis precludes collecting the totality of the dipole edge radiation (Fig. 72). Again, the cut in the energy angular spectral distribution creates diffraction larger than that of the limited opening of the light cone. To reduce the diffraction effect, a solution is to bring the edge of the mirror closer to the beam axis in order to collect the full edge radiation. Table 32 shows that the diffraction effect is strongly reduced at the collision energy when the edge is at 8 $\sigma_{H,7\text{ TeV}}$ instead of 15 $\sigma_{H,450\text{ GeV}}$ from the proton beam axis. When one brings the edge closer to the mirror, the PSF widens again because the depth of field effect then increases by accepting the radiation coming from the centre of D3.

Thus, more than the mirror size, the position of the edge of the mirror seems to be a factor influencing the system resolution to a significant degree. However, the optimization of the flux collected at injection entails taking the largest possible mirror, taking into account the geometrical constraints imposed by the dimension of the vacuum chamber. For reasons of economy, if the collected flux is sufficient at injection energy, it would be better to use a 40×40 mm^2 mirror.

Influence of the distance d between the undulator and the dipole As long as one of the two sources dominates the other, the effect of the distance d is reduced to a defocusing which can be corrected with

Table 32: Comparison between diffraction spot sizes and the beam size in the image plane for various mirror sizes for λ = 500 nm. The focusing point is defined by its distance from the focusing mirror

				r.m.s. dimensions			
Proton energy (TeV)	x_2 (m)	Mirror dimensions (mm × mm)	Mirror edge position	Image plane		Object plane	
				PSF (mm)	Beam (mm)	PSF (mm)	Beam (mm)
0.45	25.8	50 × 50	15 $\sigma_{H,450\ \mathrm{GeV}}$	0.036	0.210	0.19	1.12
0.45	25.8	40 × 40	15 $\sigma_{H,450\ \mathrm{GeV}}$	0.028	0.210	0.15	1.12
7.00	25	50 × 50	15 $\sigma_{H,450\ \mathrm{GeV}}$	0.103	0.056	0.51	0.28
7.00	25	40 × 40	15 $\sigma_{H,450\ \mathrm{GeV}}$	0.103	0.056	0.51	0.28
7.00	25	40 × 40	15 $\sigma_{H,7\ \mathrm{TeV}}$	0.083	0.056	0.42	0.28
7.00	25	40 × 40	7 $\sigma_{H,450\ \mathrm{GeV}}$	0.062	0.056	0.31	0.28

a longitudinally mobile detector. But, in the beam energy range where the two sources are equivalent from the point of view of emitted flux, the distance d determines the period of the interference rings, according to what was seen in Section 4. These interference rings between the undulator and the dipole edge have been observed in an SPS experiment [4]. Thus, the larger the distance d, the more numerous are the rings visible in the central lobe in the plane of the extraction mirror (Figs. 86–89).

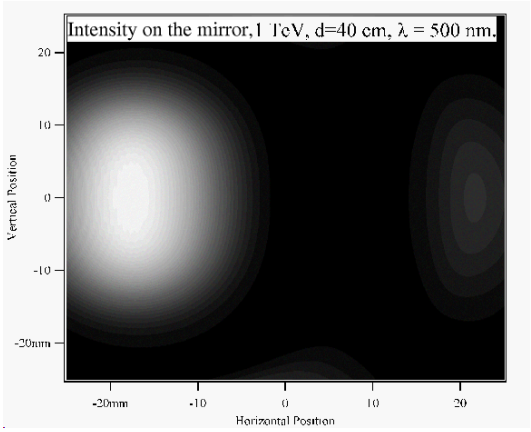

Fig. 86: Intensity emitted by a filament beam in the plane of the mirror at 1 TeV for $d = 40$ cm

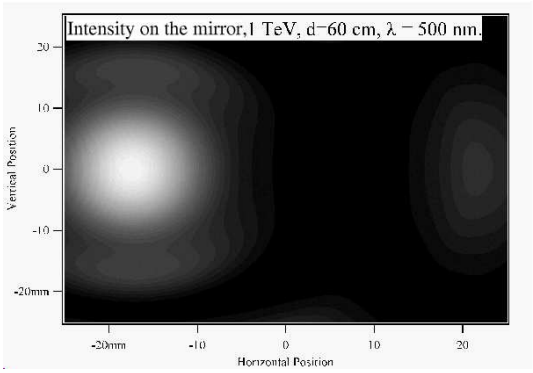

Fig. 87: Intensity emitted by a filament beam in the plane of the mirror at 1 TeV for $d = 60$ cm

However, the cuts in the angular spectral energy density are appreciably the same and thus the contributions of the diffraction to the PSF broadening stay at the same order of magnitude over the range of variations of the d distance from 40 m to 1 m (Figs. 90 and 91). Above this limit, the defocusing of one of the two sources becomes too important and we can see different spots in the image plane, as shown on the cut with $d = 3$ m (Fig. 92).

When the distance d is increased, the maximum collected intensity decreases and the r.m.s. spot size increases (Fig. 92). Above a distance d about 1 m, the two sources become incoherent and the central peak is divided into two peaks corresponding to the two sources. It would then be better to minimize the distance between the undulator and the D3 dipole taking into account the layout constraints for the undulator and the D3 dipole cryostats.

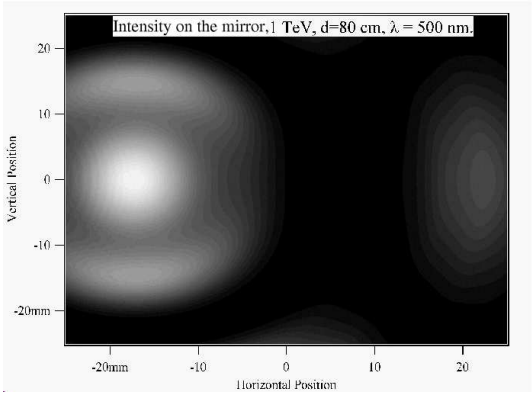

Fig. 88: Intensity emitted by a filament beam in the plane of the mirror at 1 TeV for $d = 80$ cm

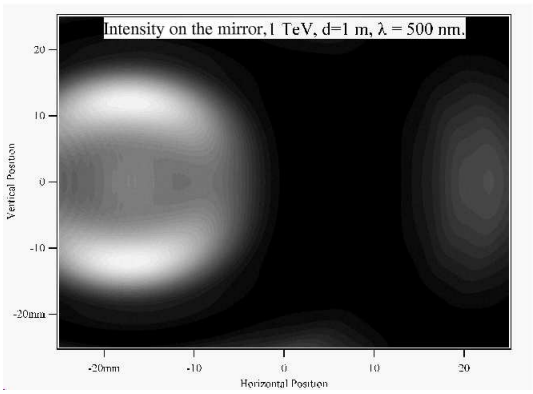

Fig. 89: Intensity emitted by a filament beam in the plane of the mirror at 1 TeV for $d = 1$ m

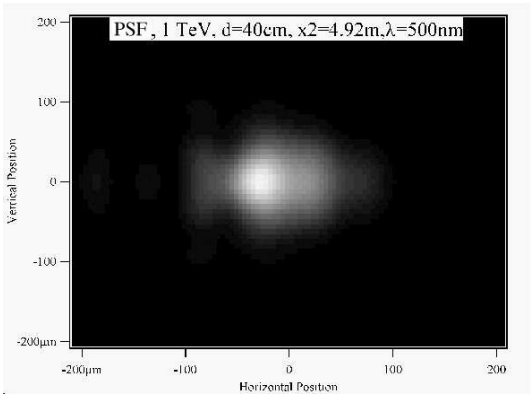

Fig. 90: Intensity emitted by a filament beam in the detector plane at 1 TeV for $d = 40$ cm

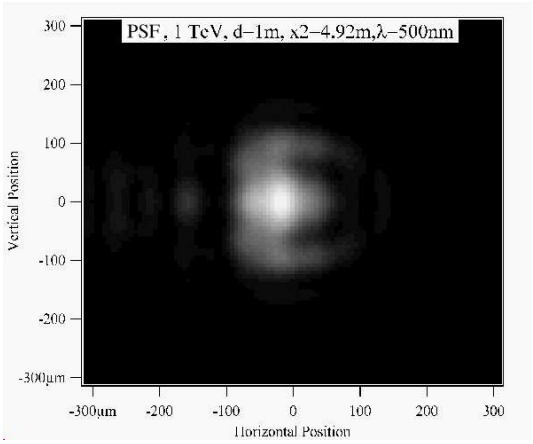

Fig. 91: Intensity emitted by a filament beam in the detector plane at 1 TeV for $d = 1$ m

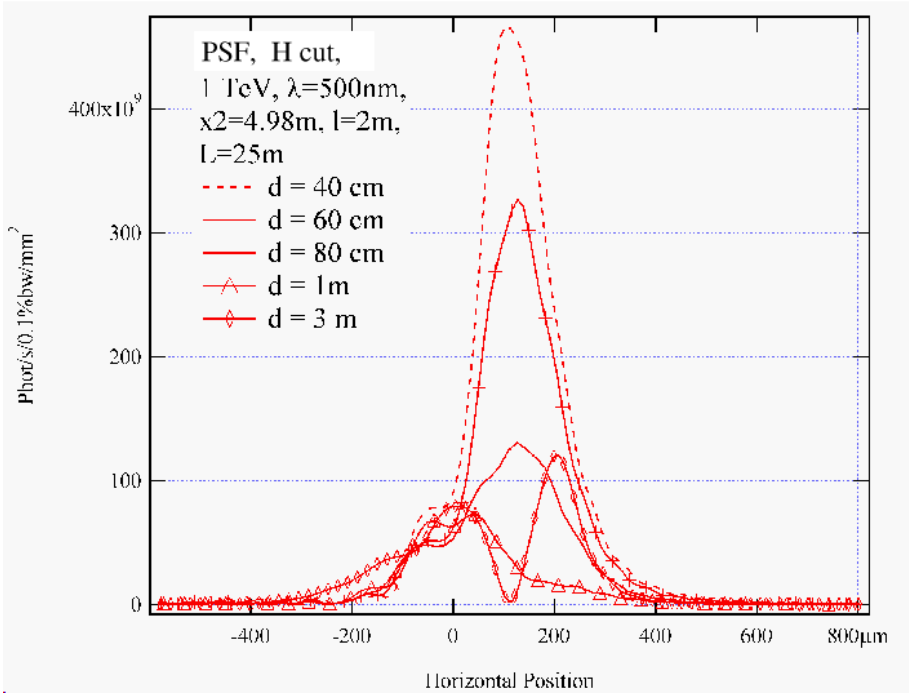

Fig. 92: Comparison for various d of the PSF horizontal cuts in the detector plane at 7 TeV proton energy and for $\lambda = 500$ nm

Influence of the distance l between the extraction mirror and the focusing mirror The extraction mirror displacement wrt the focusing mirror, for the same mirror dimensions and as long as the extraction mirror remains the limiting aperture, amounts to modify the angular acceptance of the system. The more reduced the acceptance, the larger the diffraction effect (Table 33).

Table 33: Comparison of the sizes of the PSF horizontal cut and of the beam in the image plane for various distances l between the extraction mirror and the focusing mirror, Fig. 69, for λ = 500 nm and x_2 = 5 m

				r.m.s. dimensions			
Protons	l	L	Mirror	Image plane		Object plane	
energy			dimensions	Image	Beam	Image	Beam
(TeV)	(m)	(m)	(mm × mm)	(mm)	(mm)	(mm)	(mm)
7	0	27	40 × 40	0.110	0.056	0.55	0.28
	1	26	40 × 40	0.109	0.056	0.54	0.28
	2	25	40 × 40	0.103	0.056	0.51	0.28
7	0	27	50 × 50	0.111	0.056	0.56	0.28
	1	26	50 × 50	0.106	0.056	0.53	0.28
	2	25	50 × 50	0.103	0.056	0.52	0.28
7	2	25	46.3 × 46.3	0.103	0.056	0.52	0.28

However, because of the decentring of the mirror compared to the symmetry axis of the radiation, for the same angular acceptance from a purely geometrical point of view, the diffracting effect is different according to l because the angular distribution of the radiation is not uniform. In the telescope case, a distance l of the order of 2 m allows to increase the angular acceptance for given mirror sizes while keeping almost the same illumination on the mirror (Figs. 93 and 94).

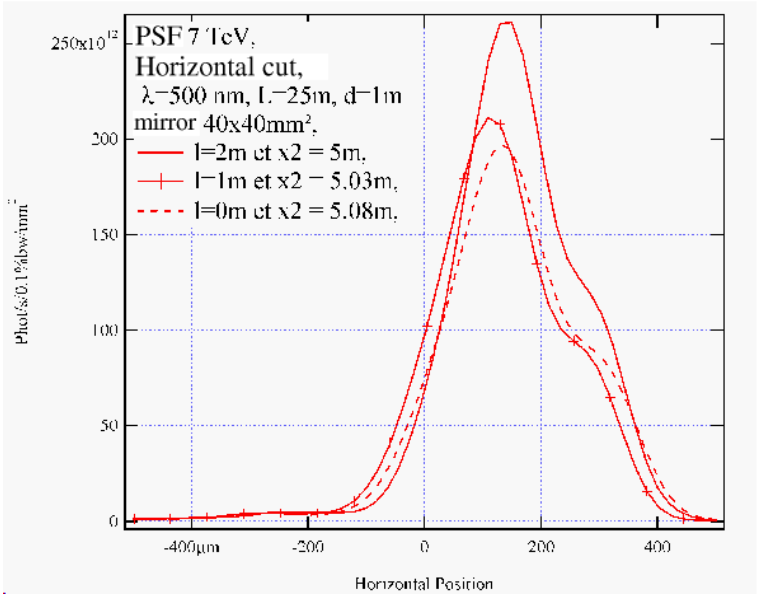

Fig. 93: Cuts in the horizontal plane of the PSF at 7 TeV for various l and a 40×40 mm^2 mirror

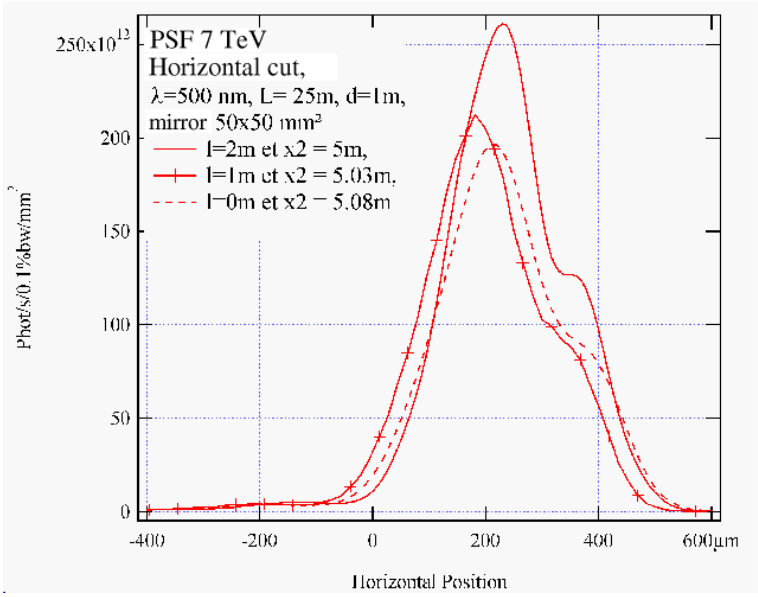

Fig. 94: Cuts in the horizontal plane of the PSF at 7 TeV for various l and a 50×50 mm^2 mirror

7.4.4 Use of a slit in the focal plane

We saw previously that the position of the extraction mirror is very important at the collision energy. Indeed, if the edge is too far from the beam axis, the mirror intercepts only part of the edge radiation. On the other hand, if one brings the mirror edge closer to the beam while remaining at 15 $\sigma_{H,\ 7\ \mathrm{TeV}}$, then it is possible to collect all the edge radiation. Diffraction is then supplanted by the depth of field effect. A solution to this problem is to use a vertical slit in the focal plane of the focusing mirror, as was done in the LEP monitor [17].

This slit is equivalent to a limitation of the angular acceptance of the optical system independent of the beam position [33, 34]. By choosing its horizontal and vertical dimensions, as well as its horizontal position, it is thus possible to select an angular portion of the emitted radiation.

At 7 TeV We will suppose here that the mirror edge is at 15 $\sigma_{H,\ 7\ \mathrm{TeV}}$ from the proton beam axis. In this case, the angular intensity distribution collected on the extraction mirror, presented in Fig. 95, is comprised of the edge radiation and of part of the D3 centre radiation. One notices that in the vertical plane, the only limitation comes from the angular opening of the radiation. The slit in the focal plane, centred on the position of the edge radiation maximum, makes it possible to angularly select the radiation coming from the dipole and thus to limit the depth of field effect. Figure 96 gives the horizontal and vertical PSF r.m.s. size evolution with the horizontal opening of the slit. The angular acceptance limitation

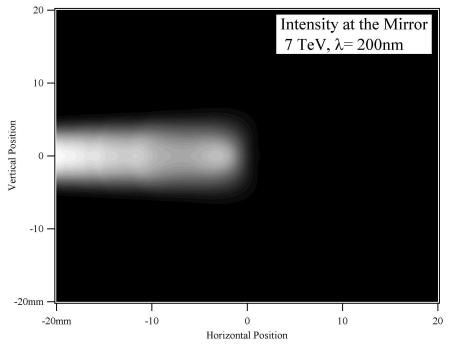

Fig. 95: Intensity collected at 7 TeV on an extraction mirror of 40×40 mm^2 at 25 m whose edge is at 15 $\sigma_{H,\ 7\ \mathrm{TeV}}$ from the proton beam axis, for λ = 200 nm. The beam axis is at -25 mm taking into account angular separation between the optical axis [in (0,0) on the figure] and the beam direction on the outlet side of the D3 magnet.

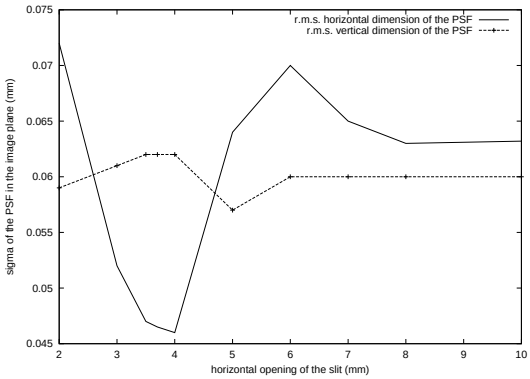

Fig. 96: Horizontal and vertical PSF r.m.s. sizes evolution at 7 TeV according to the horizontal opening of the slit

in the horizontal plane amounts to reducing the observed length of the source. The PSF r.m.s. dimension decreases with the horizontal opening of the slit as long as the slit is sufficiently open to collect the whole radiation coming from the edge. Then, when it becomes too narrow and cuts into the angular distribution of the edge radiation, diffraction again becomes more significant and the PSF widens.

In the vertical plane, the effect is different. The limitation of the horizontal angular acceptance reduces the depth of field without introducing a limitation in the vertical plane. However, the effect is very small in this case because the diffraction due to the small angular opening remains dominant and the r.m.s. size of the PSF in the vertical plane remains almost constant.

Figure 97 shows the PSF and its cut in the horizontal plane for a proton energy of 7 TeV and λ = 200 nm. The angular filtering by the slit not only improves the resolution, but it also improves the quality of the image (cf. Fig. 74).

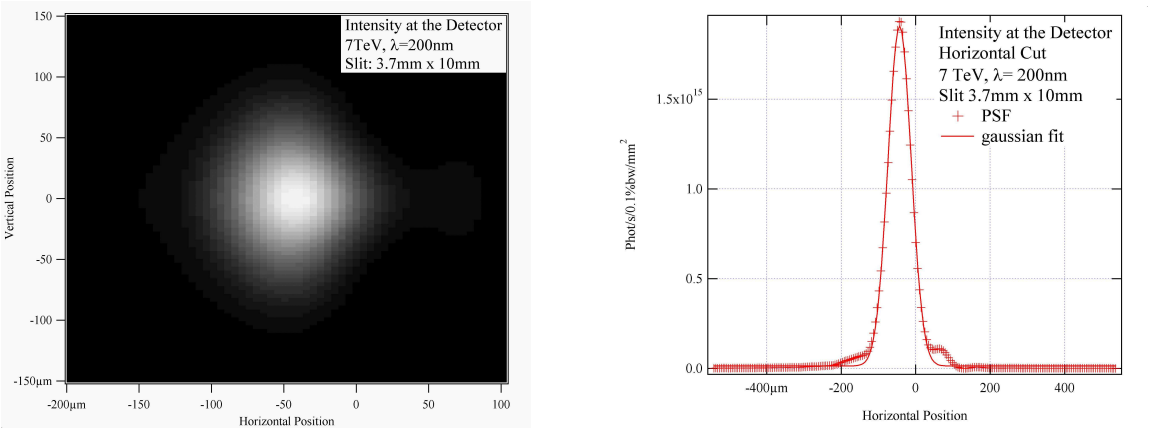

Fig. 97: PSF and cut in the horizontal plane at 7 TeV, for λ = 200 nm with a vertical slit in the focal plane of dimensions (H,V) 3.7 mm by 10 mm centred on the direction of the entrance edge of the dipole and of the undulator

At 1 TeV We saw previously that at 1 TeV the emitted angular spectral energy density is cut in an asymmetric way by the extraction mirror (Fig. 75) giving an image with two spots (Fig. 76). For the same extraction mirror, the slit in the focal plane provides again angular filtering of the contribution of the intercepted part of the ring corresponding to the λ = 500 nm wavelength at the origin of the secondary lobe (Fig. 98). The image quality is thus improved to a significant degree with a slit (or more exactly a

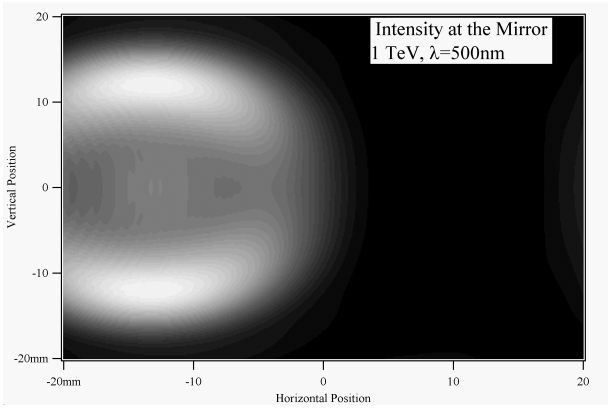

Fig. 98: Intensity collected on a 40 $\times$40 mm^2 mirror at an energy of 1 TeV

rectangular diaphragm) in the focal plane, making it possible to limit the angular acceptance (cf. Figs. 99 and 100).

7.5 Conclusions

In order to optimize the resolution at collision energy, it is necessary to use the smallest possible wavelength for the optical system and the chosen synchrotron radiation source. This wavelength could be 200 nm when taking into account the existing components. On the other hand, for lower energies, it is possible to work with more traditional wavelengths, near to 500 nm. The procedure suggested is thus to use a relatively broad wavelength range around 500 nm at low energies, to maximize the collected flux, then to use a narrow spectral range near to 200 nm at high energy, when there is enough light intensity.

To minimize the depth of field effect by keeping a fixed image point, it is then necessary to focus the optics on the D3 dipole edge. An additional improvement can be made for low energies by choosing to focus the optics on the undulator exit up to 1 TeV, afterwards only on the edge of the dipole. Thus, to

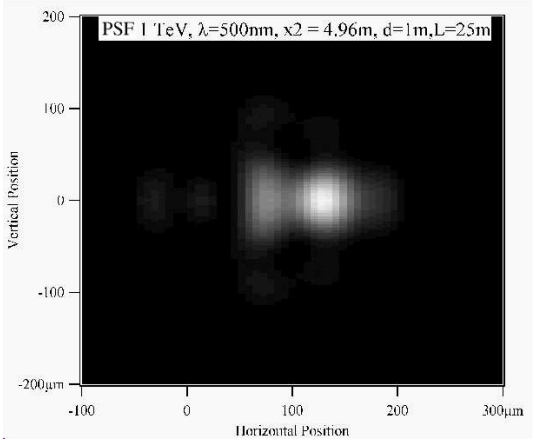

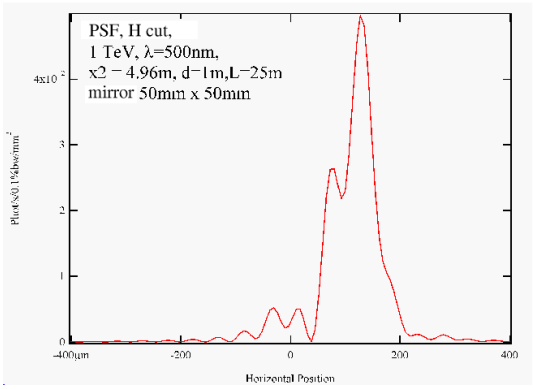

Fig. 99: PSF and cut in the horizontal plane at 1 TeV, for λ = 500 nm with a 50×50 mm^2 mirror

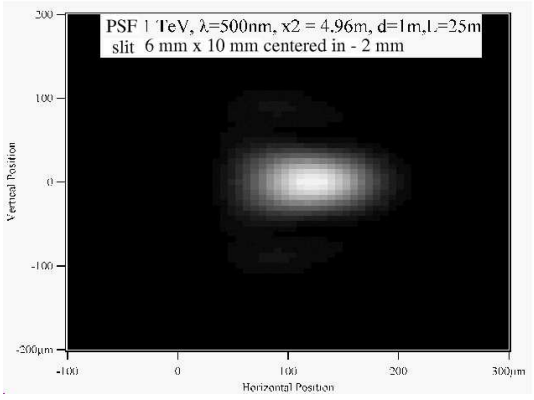

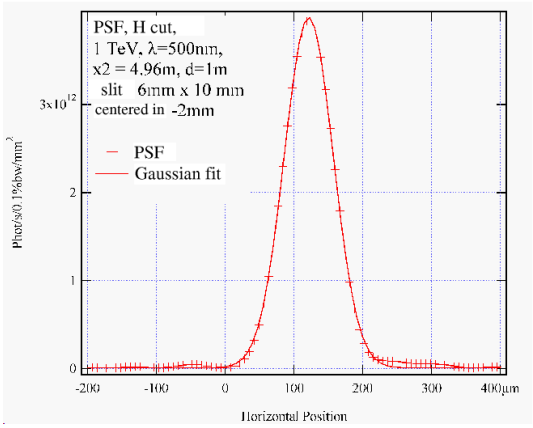

Fig. 100: PSF and cut in the horizontal plane at 1 TeV, for λ = 500 nm with the 50×50 mm^2 mirror and a rectangular diaphragm (H,V) 6 mm $\times$ 7 mm in the focal plane

limit the longitudinal movement of the detector while improving the quality of the image, it is necessary to reduce the distance between the undulator and the dipole. A compromise between the manufacturing cost and the optical performance leads to $d = 80$ cm.

Finally, the size of the extraction mirror is not a limit for the resolution, but also for the collected flux. On the other hand, the position of the edge of this mirror compared to the undulator and D3 entrance axis is a determining factor for the prcision of the instrument, in particular at high energy. It is necessary to come as close as possible to the beam axis. A mobile extraction mirror thus makes it possible to remain at 15 σ_{H} for a given energy while coming closer to the beam with the rise in the proton beam energy.

Table 34 summarizes the performance of the optical system with the procedure described previously. The proton beam sizes ($\sigma_{O,H \text{ or } V}$) come from Table 2, the PSF r.m.s. sizes ($\sigma_{\mathrm{PSF},H \text{ or } V}$) are obtained by starting from a numerical Gaussian fit, carried out with the SRW code, and are brought back to the object plane to be independent of the optical magnification G. Image sizes ($\sigma_{I,H \text{ or } V}$) are obtained starting from Eq. (116) by quadratically adding the r.m.s. size of the proton distribution and of the PSF. Finally, the last two columns give the widening, expressed in per cent of the spot image compared to the real dimensions of the beam, due to the diffraction and the depth of field effects:

$$\frac{\delta\sigma_{H \; or \; V}}{\sigma_{H \text{ or } V}} = \frac{\sigma_{I,H \text{ or } V} - \sigma_{O,H \text{ or } V}}{\sigma_{O,H \text{ or } V}} \quad . \tag{147}$$

Table 34: Performance of a monitor using the superconducting undulator and the D3 dipole as a synchrotron radiation source

	Size							
Proton energy (TeV)	Proton beam		PSF		Image			
	$\sigma_{O,H}$ (μm)	$\sigma_{O,V}$ (μm)	$\sigma_{PSF,H}$ (μm)	$\sigma_{PSF,V}$ (μm)	$\sigma_{I,H}$ (μm)	$\sigma_{I,V}$ (μm)	$\frac{\delta\sigma_H}{\sigma_H}$ (%)	$\frac{\delta\sigma_V}{\sigma_V}$ (%)
0.45	1120	1480	159	141	1131	1487	1.0	0.5
1.00	750	990	198	120	776	997	3.4	0.7
7.00	280	380	156	194	320	427	14.5	12.3

In all cases, the widening of the image spot due to the diffraction and depth of field effects remains lower than 15% of the size of the beam to be measured (Table 34). It is thus sufficiently small to obtain the real size of the beam by quadratic subtraction. In addition, this widening is given mainly by the angular distribution of the radiation, and is therefore stable for a given energy. Moreover, it is independent of the beam intensity. The corrections to be introduced can thus be calculated and calibrated with the help of the wire scanners at low intensity [8].

It should be noted that the resolution can be increased by modifying the local optical functions of the LHC machine ($\beta_{H,V}$ function with $\sigma_{H,V} = \sqrt{(\beta_{H,V}\epsilon_{H,V})}$): for the same widening, the beam to be measured is then larger. The possibility of using the same telescope on the D2 dipole, in a point of the LHC where the optics of the machine is modified in collision mode, can become interesting at high energy.

8 CONCLUSION

The goal of this work subject of a thesis [48] was the design of a monitor using the synchrotron radiation to measure the proton beam profiles over the whole LHC energy range (450 GeV–7 TeV). Preliminary studies had led to a pre-selection of possible sources and had resulted in considering the use of a LHC

dipole (a dispersion suppressor dipole or a separation dipole of the D2 type) in IR5 from 2 TeV up to 7 TeV and the insertion at another location of a dedicated set-up, like a short dipole, from the injection up to 2 TeV. The analytical and numerical studies realized within the framework of this work have confirmed the weaknesses of this solution for low energies (below 2 TeV). A modification of the LHC layout in IP4 followed by a comparative study of the performance of several magnetic configurations resulted then in the choice of a unique source dedicated to profile measurement: a superconducting undulator with a 5 T peak magnetic field combined with a dipole edge effect.

After a presentation of the LHC machine and of the working hypotheses for the monitor in Section 2, the main results of the synchrotron radiation theory are presented in Section 3 introducing the equations used for both the analytical calculation and the numerical tools. Section 4 explains the various analytical models at our disposal or developed for the calculation of the angular spectral energy densities of various types of sources. Two simplifying models are explained: the study of interferences between two sources and the low-frequency approximation of the angular spectral energy density allowing analytically calculable integrals with series expansions up to different orders. Section 5 presents the Zgoubi program, used to simulate the synchrotron radiation emitted by any magnetic source, in particular when no known model is applicable. Particular care was taken to cross-check as often as possible the results with the analytical formulas at disposal.

The last two Sections, 6 and 7 detail the results of the work completed. First of all, a thorough comparison of the performance of the various sources studied was carried out in order to justify the final choice. The principal configurations considered are the D2 dipole, a superconducting miniwiggler creating a self-compensated orbit bump, a room-temperature undulator, and, finally, a superconducting undulator. The comparison of fluxes is largely in favour of the combination of a superconducting undulator with a dipole edge effect. Section 7 gives the study of the optical performance of the monitor, based on simulations with the SRW code.

The system finally selected consists of a superconducting undulator with two 28 cm long periods, with a 5 T peak magnetic field peak, combined with the edge effect of a 9.45 m long dipole with a magnetic field of 3.9 T at 7 TeV. The performance in terms of intensity collected as well as in terms of precision of the optics should satisfy the requirements of the users, including with a pilot bunch and in turn-by-turn modes.

As an extension to the work already completed, several points can be still developed. First of all, the study of the optical performance, based on simulations with SRW, was carried out with ideal components. The imperfections of these components thus remain to be introduced for more rigour. Commercial codes such as Zemax have complete catalogues to study the telescope with real components in a detailed way. However, they generally do not make it possible to simulate the synchrotron radiation sources. At the other end of the chain, Zgoubi simulates the source precisely, but not the optical propagation. An interesting development could thus be brought to the Zgoubi code by introducing the optical calculation of the propagation of synchrotron radiation based on the operator method. The ingredients necessary (methodology, equations and electric fields) have been given and the largest part of the work would consist in developing and testing the code.

Another point to evaluate is the use of the SR monitor with ions beam. In addition, the evaluation of the energy collected by the telescope was calculated starting from simulations of undulator magnetic field maps. When the undulator prototype will be built, one will undoubtedly need to perform the simulations with the measured field maps.

A APPENDIX LOW-FREQUENCY DERIVATION UP TO ORDER 2

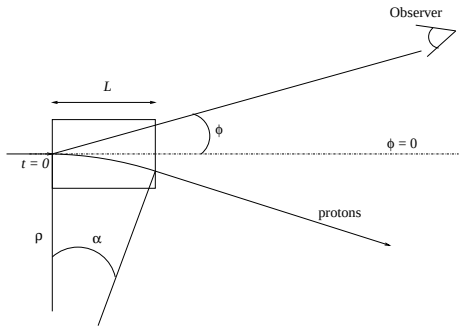

Fig. A.1: Definition of the reference frame used for calculation

If the observation frequency ω is such that $\omega\Delta t \ll 1$, the Fourier transform of the electric field is written:

$$\begin{aligned}\tilde{E}(\phi,\psi,\omega) &= \frac{1}{\sqrt{2\pi}}\int_{-\infty}^{+\infty} E(\phi,\psi,t)e^{-i\omega t}dt \\ &\underset{\omega\ll\omega_l}{\simeq} \frac{1}{\sqrt{2\pi}}\int_{\Delta t} E(\phi,\psi,t)(1-i\omega t-\frac{(\omega t)^2}{2}+i\frac{(\omega t)^3}{6}+...+\frac{(i\omega t)^n}{n!})\,dt\ .\end{aligned} \tag{A.1}$$

The calculation of $\tilde{E}(\phi,\psi,\omega)$ is reduced thus to integrals calculations of the form $\int E(t)t^n dt$ with n an integer.

A.1 Calculation of order 0: $R_0 = \int_{-\infty}^{+\infty} E(\phi,\psi,t)dt$

According to Eqs. (15)–(16) with $\omega_0 = \frac{c}{\rho}$, the σ component of the electric field is defined by:

$$\begin{aligned} t &= \frac{1+\gamma^2(\phi^2+\psi^2)}{2\gamma^2}t' - \frac{\omega_0\phi t'^2}{2} + \frac{\omega_0^2}{6}t'^3 \\ \frac{dt}{dt'} &= \frac{1+\gamma^2\psi^2+\gamma^2(\omega_0 t'-\phi)^2}{2\gamma^2} \\ E_\sigma(t') &= \frac{q\omega_0\gamma^4}{\pi\epsilon_0 cr}\frac{(1+\gamma^2\psi^2)-\gamma^2(\omega_0 t'-\phi)^2}{(1+\gamma^2\psi^2+\gamma^2(\omega_0 t'-\phi)^2)^3}\ . \end{aligned} \tag{A.2}$$

By defining $P(t') = \frac{(1+\gamma^2\ \psi^2)-\gamma^2(\omega_0 t'-\phi)^2}{(1+\gamma^2\psi^2+\gamma^2(\omega_0 t'-\phi)^2)^2}$, R_0 is rewritten in the form:

$$R_0 = \frac{q\omega_0\gamma^2}{2\pi\epsilon_0 cr}\int_0^{\frac{L}{c}} P(t')dt'\ . \tag{A.3}$$

By carrying out the change of variable $u = \frac{\gamma(\omega_0 t'-\phi)}{\sqrt{1+\gamma^2\psi^2}}$, the calculation of $P_1(t') = \int P(t')dt'$, a primitive form of $P(t')$, is written:

$$P_1(t') = \int P(t')dt' = \frac{1}{1+\gamma^2\psi^2}\int\frac{1-u^2}{(1+u^2)^2}\frac{\sqrt{1+\gamma^2\psi^2}}{\gamma\omega_0}du \tag{A.4}$$

$$= \frac{1}{\gamma\omega_0\sqrt{1+\gamma^2\psi^2}}\frac{u}{1+u^2} \tag{A.5}$$

$$P_1(t') = \frac{\omega_0 t'-\phi}{\omega_0\left(1+\gamma^2\psi^2+\gamma^2(\omega_0 t'-\phi)^2\right)}\ . \tag{A.6}$$

Whence the following expression of R_0, with $K = \alpha\gamma/2$ and $\alpha = L/\rho$:

$$R_0 = \frac{q\gamma}{2\pi\epsilon_0 cr}\left[\frac{2K-\gamma\phi}{1+\gamma^2\psi^2+(2K-\phi)^2}+\frac{\gamma\phi}{1+\gamma^2(\psi^2+\phi^2)}\right] \quad . \tag{A.7}$$

By carrying out the change of orientation of the reference frame $\phi \Rightarrow \phi + \alpha/2$ (Fig. A.1) one finds the expression (48) given in Section 4.

A.2 Calculation of order 1: $R_1 = \int_{-\infty}^{+\infty} E(\phi,\psi,t)t\,dt$

se beam profile measurements, the first stage is to choose the best possible source in terms of flux co

In the same way, R_1 is written according to t' for a L long magnet:

$$R_1 = \frac{q\omega_0\gamma^2}{2\pi\epsilon_0 cr}\int_0^{\frac{L}{c}} \frac{(1+\gamma^2\psi^2)-\gamma^2(\omega_0 t'-\phi)^2}{(1+\gamma^2\psi^2+\gamma^2(\omega_0 t'-\phi)^2)^2} \left(\frac{1+\gamma^2(\phi^2+\psi^2)}{2\gamma^2}t' - \frac{\omega_0\phi t'^2}{2}+\frac{\omega_0^2 t'^3}{6}\right)dt' \quad . \tag{A.8}$$

By defining $P(t') = \frac{(1+\gamma^2\psi^2)-\gamma^2(\omega_0 t'-\phi)^2}{(1+\gamma^2\psi^2+\gamma^2(\omega_0 t'-\phi)^2)^2}$, one reduces the problem to calculations of several integrals of the S_n type:

$$R_1 = \frac{q\omega_0\gamma^2}{2\pi\epsilon_0 cr}\left[\frac{1+\gamma^2(\phi^2+\psi^2)}{2\gamma^2}\underbrace{\int_0^{\frac{L}{c}} P(t')t'dt'}_{S_1} - \frac{\omega_0\phi}{2}\underbrace{\int_0^{\frac{L}{c}} P(t')t'^2dt'}_{S_2}+\frac{\omega_0^2}{6}\underbrace{\int_0^{\frac{L}{c}} P(t')t'^3dt'}_{S_3}\right] \quad . \tag{A.9}$$

Calculation of $S_n = \int_0^{\frac{L}{c}} P(t')t'^n dt'$ The calculation of R_1 is reduced to the calculation of three integrals $S_n = \int_0^{\frac{L}{c}} P(t')t'^n dt'$. By carrying out several integrations by parts, one notices that these three integrals are expressed starting from the successive primitives of $P(t')$. For example, the calculation of S_3 by three successive integrations by parts integrating $P(t')$ and by deriving t'^3 leads to:

$$S_3 = \left[P_1(t')\right]_0^{L/c} - 3\left[P_2(t')\right]_0^{L/c} + 6\left[P_3(t')\right]_0^{L/c} - 6\left[P_4(t')\right]_0^{L/c} \tag{A.10}$$

with $P_n(t') = \int P_{n-1}(t')dt'$ primitive of $P_{n-1}(t')$. By introducing the values of $P_n(L/c)$ and $P_n(0)$ into the expressions of type (A.11), one obtains the expressions of S_n:

$$S_3 = P_1(L/c)\frac{L^3}{c^3} - 3P_2(L/c)\frac{L^2}{c^2} + 6P_3(L/c)\frac{L}{c} - 6\left(P_4(L/c)-P_4(0)\right) \tag{A.11}$$

$$S_2 = P_1(L/c)\frac{L^2}{c^2} - 2P_2(L/c)\frac{L}{c} + 2\left(P_3(L/c)-P_3(0)\right) \tag{A.12}$$

$$S_1 = P_1(L/c)\frac{L}{c} - 2\left(P_2(L/c)-P_2(0)\right) \quad . \tag{A.13}$$

Calculation of $P_n(t') = \int P_{n-1}(t')dt'$ The calculation of $P_1(t') = \int P(t')dt'$ was already carried out for calculation with order 0:

$$P_1(t') = \frac{\omega_0 t'-\phi}{\omega_0\left(1+\gamma^2\psi^2+\gamma^2(\omega_0 t'-\phi)^2\right)} \quad . \tag{A.14}$$

With the same change of variable $u = \frac{\gamma(\omega_0 t' - \phi)}{\sqrt{1+\gamma^2\psi^2}}$, the following primitives give:

$$P_2(t') = \frac{1}{2(\gamma\omega_0)^2} \ln\left(1 + \frac{\gamma^2(\omega_0 t' - \phi)^2}{1+\gamma^2\psi^2}\right) \tag{A.15}$$

$$P_3(t') = \frac{\sqrt{1+\gamma^2\psi^2}}{(\gamma\omega_0)^3}\left[\text{Arctan}\left(\frac{\gamma(\omega_0 t' - \phi)}{\sqrt{1+\gamma^2\psi^2}}\right) - \frac{\gamma(\omega_0 t' - \phi)}{\sqrt{1+\gamma^2\psi^2}}\right. \tag{A.16}$$
$$\left. + \frac{\gamma(\omega_0 t' - \phi)}{2\sqrt{1+\gamma^2\psi^2}} \ln\left(1 + \frac{\gamma^2(\omega_0 t' - \phi)^2}{1+\gamma^2\psi^2}\right)\right]$$

$$P_4(t') = \frac{1+\gamma^2\psi^2}{(\gamma\omega_0)^4}\left[-\frac{3\gamma^2(\omega_0 t' - \phi)^2}{4(1+\gamma^2\psi^2)} - \frac{1}{4}\ln\left(1 + \frac{\gamma^2(\omega_0 t' - \phi)^2}{1+\gamma^2\psi^2}\right)\right. \tag{A.17}$$
$$\left. + \frac{\gamma(\omega_0 t' - \phi)}{\sqrt{1+\gamma^2\psi^2}} \text{Arctan}\,\frac{\gamma(\omega_0 t' - \phi)}{\sqrt{1+\gamma^2\psi^2}} + \frac{\gamma^2(\omega_0 t' - \phi)^2}{4(1+\gamma^2\psi^2)} \ln\left(1 + \frac{\gamma^2(\omega_0 t' - \phi)^2}{1+\gamma^2\psi^2}\right)\right] .$$

Coming back to the expression of R_1 All the ingredients are calculated, it only remains to go up the chain until R_1. First of all, by introducing the values $P_n(L/c)$ and $P_n(0)$ calculated from Eq. (A.15) in the expressions of S_n [Eq. (A.11)], then the expressions of S_n for $n = 1$ to 3 in expression (A.9), one finally obtains after simplification of Eq. (57):

$$R_1 = \int E(\phi,\psi,t)\, t\, dt \tag{A.18}$$
$$= \frac{q\gamma^2\alpha\rho}{4\pi\epsilon_0 c^2 r}\left[\left(\frac{1+\gamma^2(\phi^2+\psi^2)}{\gamma^2} - \alpha\phi + \frac{\alpha^2}{3}\right)\frac{\alpha-\phi}{1+\gamma^2((\alpha-\phi^2)+\psi^2)} + \frac{2\phi-\alpha}{2\gamma^2}\right] .$$

A.3 Calculation of order 2: $R_2 = \int_{-\infty}^{+\infty} E(\phi,\psi,t)t^2 dt$

Calculation with order 2 is in fact an approximation with order 3 in t'. Indeed, the development of t^2 as a function of t' starting from Eq. (16) gives by keeping only the terms of order 3 in t':

$$t^2 \simeq \frac{1+\gamma^2(\phi^2+\psi^2)}{2\gamma^2}\left[\frac{1+\gamma^2(\phi^2+\psi^2)}{2\gamma^2}t'^2 - \omega_0\phi t'^3\right] . \tag{A.19}$$

With the previous definition of P(t'), R_2 can be written in the form:

$$R_2 = \frac{1+\gamma^2(\phi^2+\psi^2)}{2\gamma^2}\frac{q\omega_0\gamma^2}{2\pi\epsilon_0 cr}\left[\frac{1+\gamma^2(\phi^2+\psi^2)}{2\gamma^2}\underbrace{\int_0^{L/c} P(t')t'^2dt'}_{S_2} - \omega_0\phi\underbrace{\int_0^{L/c} P(t')t'^3dt'}_{S_3}\right] . \tag{A.20}$$

One finds the same integrals as with order 1. In the same way, one thus obtains expression (58) with $\alpha = L/\rho$:

$$\int E(\phi,\psi,t)\, t^2\, dt =$$
$$\frac{q\rho^2(1+\gamma^2(\phi^2+\psi^2))}{4\pi\epsilon_0 c^3 r\gamma^2}\left[\left(\frac{1+\gamma^2(\phi^2+\psi^2)}{2\gamma^2} - \alpha\phi\right)\frac{\gamma^2\alpha^2(\alpha-\phi)}{1+\gamma^2((\alpha-\phi)^2+\psi^2)}\right.$$
$$- \alpha\left(\frac{1+\gamma^2(\psi^2-2\phi^2)}{\gamma^2} - \frac{3}{2}\alpha\phi\right) - \frac{2\phi(1+\gamma^2(\psi^2-\phi^2/2))}{\gamma^2}\ln\frac{1+\gamma^2((\alpha-\phi)^2+\psi^2)}{1+\gamma^2\phi^2+\gamma^2\psi^2}$$
$$\left. + \frac{\sqrt{1+\gamma^2\psi^2}(1+\gamma^2(\psi^2-5\phi^2))}{\gamma^3}\left(\text{Arctan}\,\frac{\gamma(\alpha-\phi)}{\sqrt{1+\gamma^2\psi^2}} - \text{Arctan}\,\frac{-\gamma\phi}{\sqrt{1+\gamma^2\psi^2}}\right)\right] . \tag{A.21}$$

B APPENDIX CALCULATION OF THE PHASE DELAY

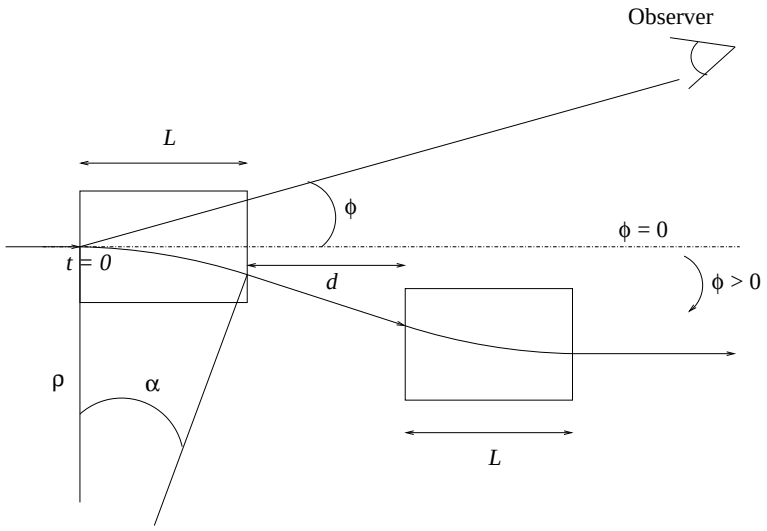

Fig. B.1: Definition of the reference frame used for the calculation of the crossing time of the magnets

Crossing time of a dipole Equation (16) gives the relation between particle time and observer time.

$$2\gamma^2 t = \left[1 + 2\gamma^2(\phi^2 + \psi^2)\right] t' - \gamma^2\phi\frac{c}{\rho}t'^2 + \frac{\gamma^2 c^2}{3\rho^2}t'^3 \quad . \tag{B.1}$$

Defining T^+ as the crossing time of the $L = \rho\alpha$ long dipole in observer time, Eq. (16) leads to:

$$\begin{aligned} 2\gamma^2 T^+ &= \left[1 + 2\gamma^2(\phi^2 + \psi^2)\right] \frac{\alpha\rho}{c} - \gamma^2\phi\frac{c}{\rho}\left(\frac{\alpha\rho}{c}\right)^2 + \frac{\gamma^2 c^2}{3\rho^2}\left(\frac{\alpha\rho}{c}\right)^3 \\ T^+ &= \frac{\alpha\rho}{2\gamma^2 c}\left[1 + \gamma^2(\phi^2 + \psi^2) - \gamma^2\phi\alpha + \frac{\alpha^2\gamma^2}{3}\right] \quad . \end{aligned} \tag{B.2}$$

Crossing time of a straight section In the same way, defining T_d as the crossing time of a d long straight section corresponding to an infinite curvature ρ, seen under the angle ϕ (Fig. B.1):

$$T_d = \frac{d}{2\gamma^2 c}\left(1 + \gamma^2(\phi^2 + \psi^2)\right) \quad . \tag{B.3}$$

Example of application Let us consider two magnets of the same length L, same radius of curvature ρ, separated by the distance d (Fig. B.1). The two magnets are in a configuration of opposite magnetic field so that the directions of entry and exit of the beam are the same. The direction of observation corresponds to an angle ϕ. The crossing time T of the whole magnetic structure is:

$$T = T^+ + T_d + T^- \tag{B.4}$$

with T^+ and T^- being the crossing time of the first and the second magnet, respectively, and T_d the crossing time of the straight section. T^+ is given by Eq. (B.2) and T_d by Eq. (B.3). For the second dipole, by symmetry, the problem comes back to that of the first dipole with a radius of curvature $-\rho$, a deflection angle $-\alpha$, and a direction of observation $-\phi$. Consequently $T^- = T^+$. Finally, the total crossing time of the structure in observer time is written:

$$T = \frac{\alpha\rho}{\gamma^2 c}\left[1 + \gamma^2(\phi^2 + \psi^2) - \gamma^2\phi\alpha + \frac{\alpha^2\gamma^2}{3}\right] + \frac{d}{2\gamma^2 c}\left[1 + \gamma^2((\phi - \alpha)^2 + \psi^2)\right] \quad . \tag{B.5}$$

C APPENDIX MAGNETIC SIMULATIONS OF THE UNDULATOR

The undulator is currently under construction. A model was designed [38] and Figs. C.1–C.4 give the performances obtained.

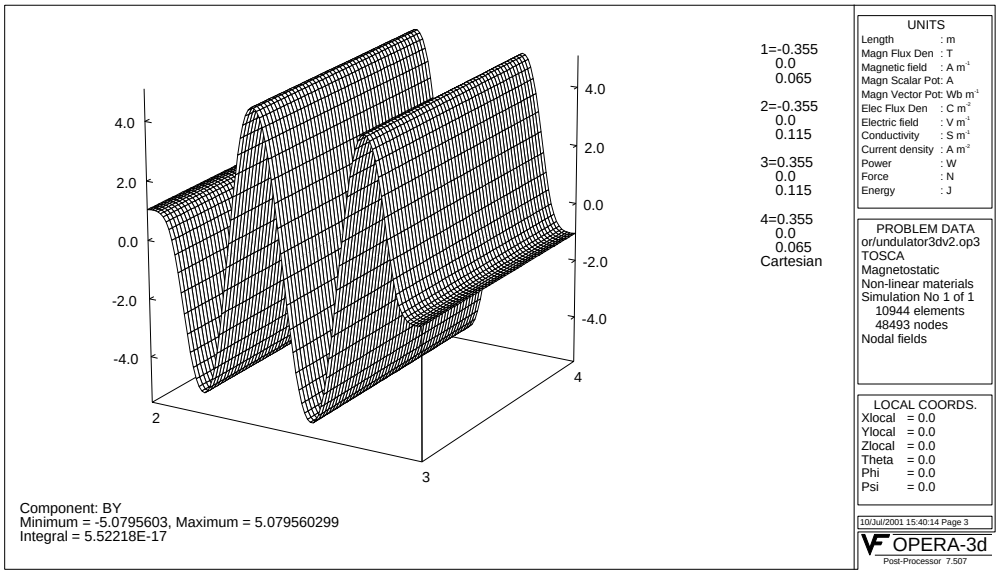

Fig. C.1: The B_Y component (transverse vertical) of the magnetic field in the horizontal median plane of the undulator

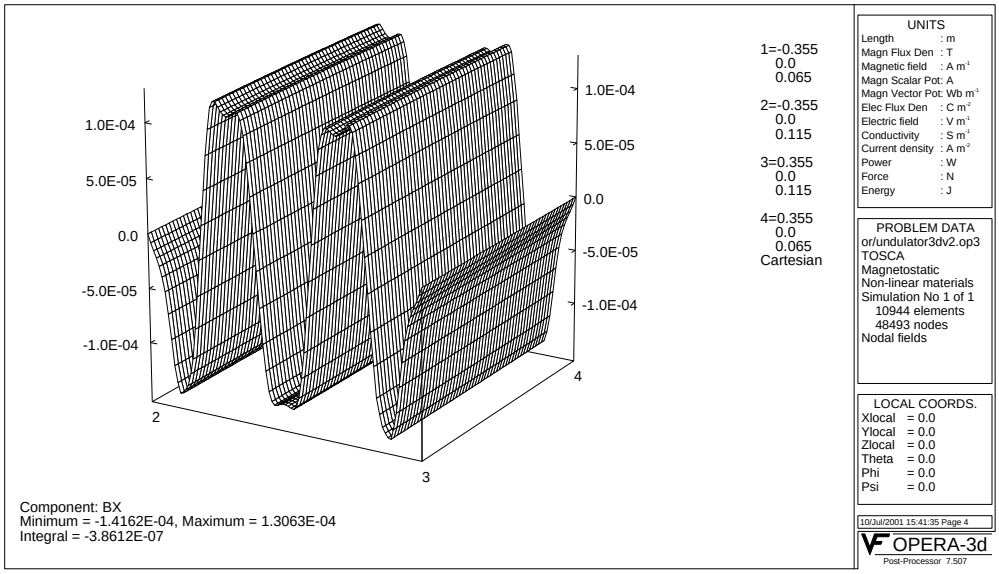

Fig. C.2: The B_X component (transverse horizontal, corresponding to the Y direction of Fig. 7) of the magnetic field in the median horizontal plane of the undulator

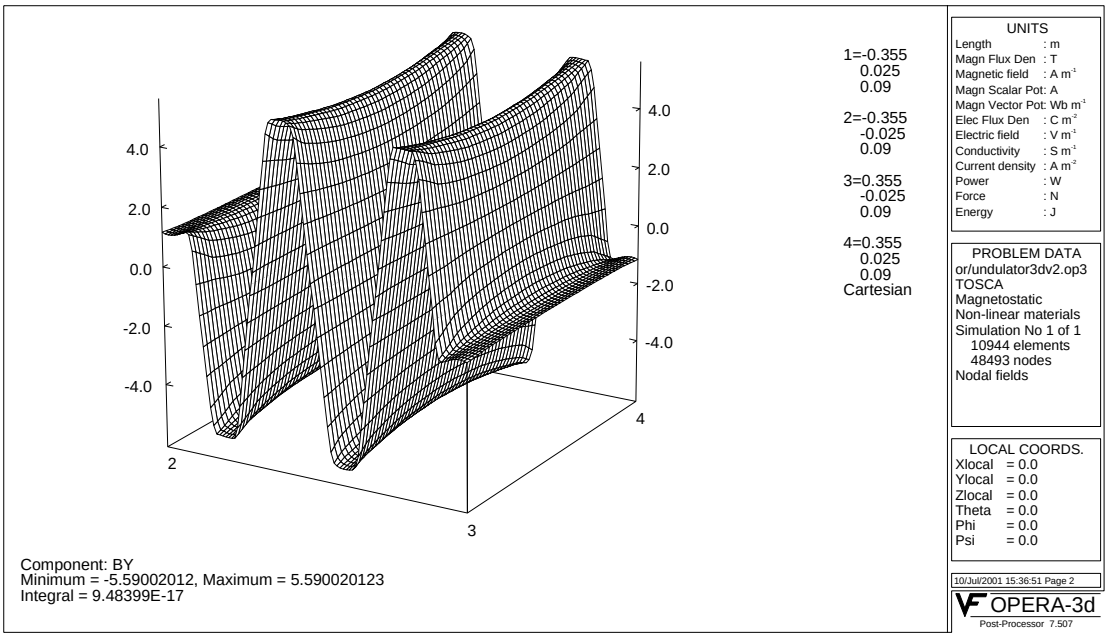

Fig. C.3: The B_Y component (transverse vertical) of the magnetic field in the vertical median plane of the undulator

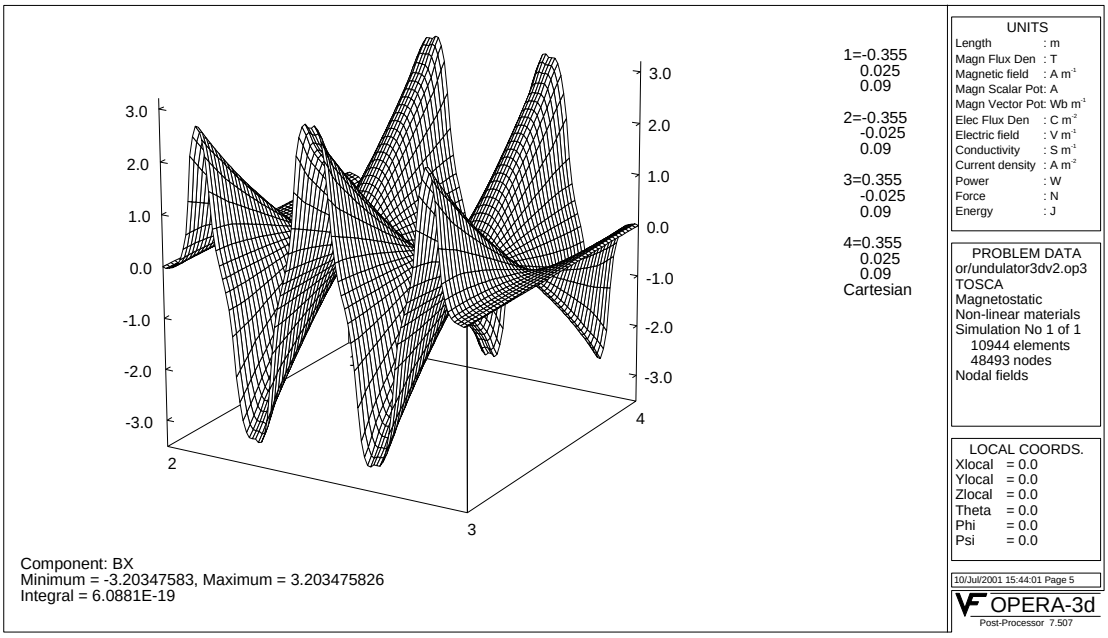

Fig. C.4: The B_X component (transverse horizontal, corresponding to the Y direction of Fig. 7) of the magnetic field in the median vertical plane of the undulator

D APPENDIX OPTICAL EQUIVALENT TO THE TELESCOPE

To confirm the equivalence between the telescope installed in LEP (BEUV) and the diaphragmed lens, from the optical point of view, we have compared the MTF and the cut of the PSF in both cases (Figs. D.1 and D.2, with the help of the Zemax program [49].

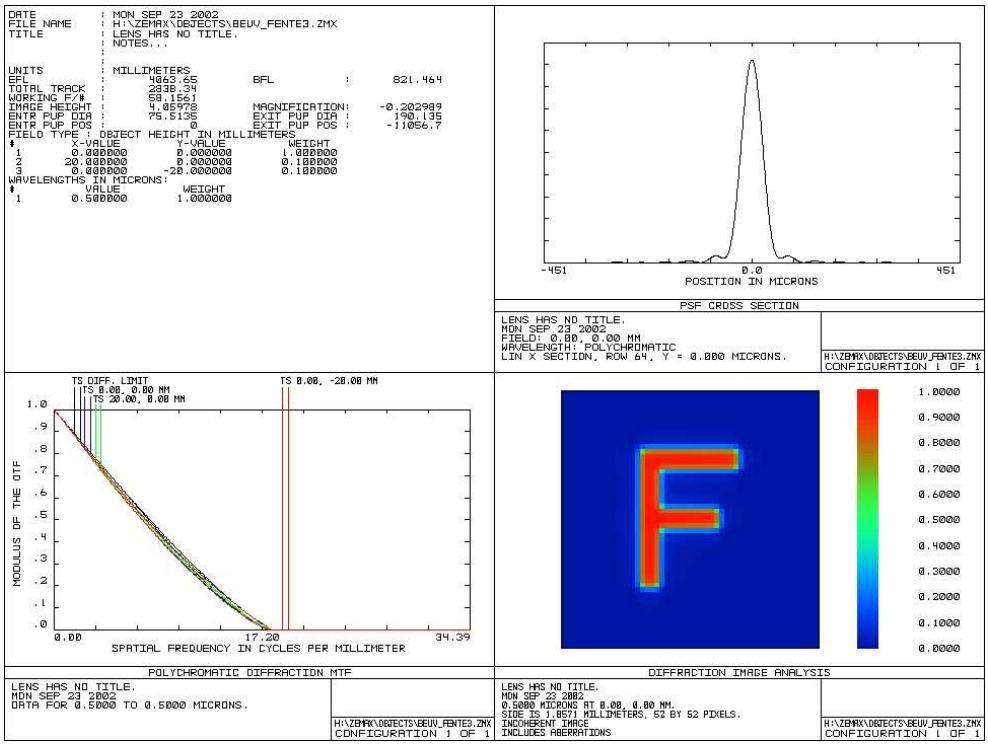

Fig. D.1: Optical data, cut of the PSF, MTF and diffracted image with the BEUV telescope

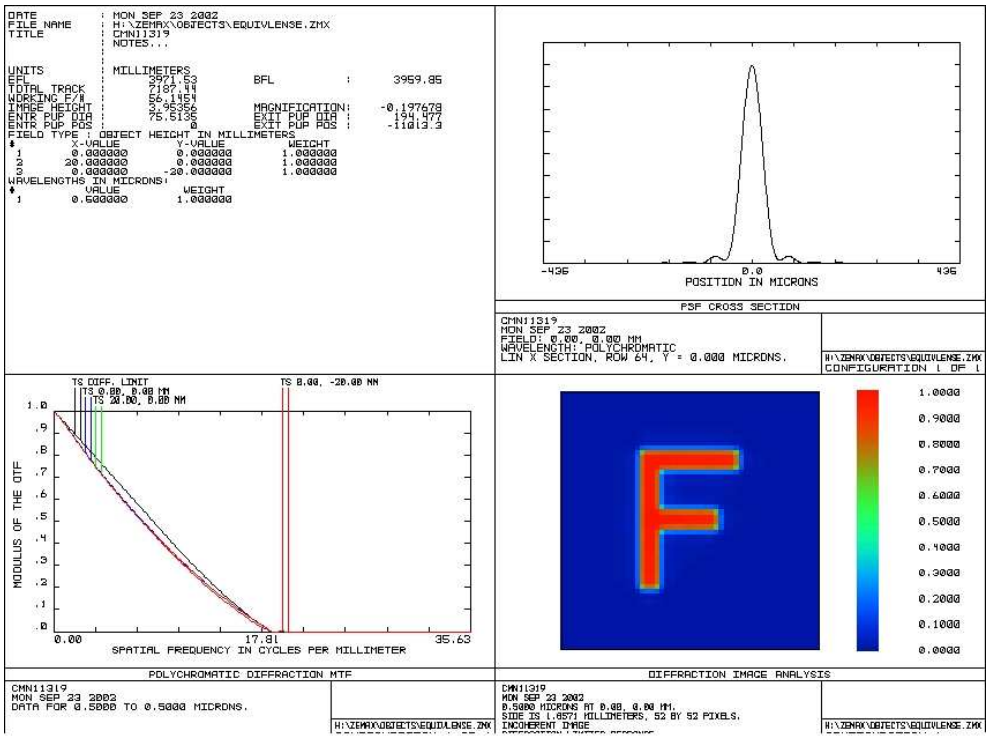

Fig. D.2: Optical data, cut of the PSF, MTF and diffracted image with the equivalent diaphragmed lens

REFERENCES

[1] J. Jackson, Classical Electrodynamics, 3rd ed. (Wiley, New York, 1998).

[2] F. R. Elder, R. V. Langmuir, A. M. Gurewich, H. C. Pollock, Phys. Rev. **71** (1947) 827.

[3] A. Hofmann, Diagnostics with synchrotron radiation, Proc. of the CERN Accelerator School, Grenoble, France, April 1996, Ed. S. Turner, CERN 98-04 (1998).

[4] J. Bosser, L. Burnod, R. Coisson, G. Ferioli, J. Mann and F. Méot, Characteristics of the radiation emitted by protons and antiprotons in an undulator, J. Phys. Lett. **45**, L343–351 (1984).

[5] The LHC Study group, The Large Hadron Collider Conceptual Design, CERN/AC/95-05(LHC) (1995).

[6] H. Brück, Accélérateurs circulaires de particules (Saclay: Bibliothèque de Sciences et Techniques Nucléaires, 1966).

[7] M. Martini, Transverse beam dynamics, Proc. Joint Universities Accelerator School (Archamps, 1996).

[8] J. Bosser and C. Bovet, Wire Scanners for LHC, LHC Project Note-108 (1997).

[9] G. Burtin, J. Camas, G. Ferioli, R. Jung, J. Koopman, R. Perret, A. Variola and J. M. Vouillot, The luminescence profile monitor of the CERN SPS, CERN-SL-2000-031 BI, presented at European Particle Accelerator Conf., Vienna (Geneva, E.P.S., 2000).

[10] C. Fischer, J. Koopman, Ionization profile monitor tests in the SPS, Proc. European Particle Accelerator Conf., Vienna, 2000, CERN-SL-99-046 BI (2000).

[11] E. Rossa, Proposition pour la mesure du profil longitudinal des paquets d'électrons circulant dans le LEP, par une méthode d'autocorrélation temporelle, CERN-LEP-Note-554 (1986).

[12] A. Hofmann, F. Méot, Optical resolution of beam cross-section measurements by means of synchrotron radiation, CERN/ISR-TH/82-04, Nucl. Instrum. Methods **203**, 483–493 (1982).

[13] J. J. Gras, LHC Injection Scenarios and Consequences on Beam Instrumentation (CERN, Geneva, to be published).

[14] MCP XX1450HD, DEP, The Netherlands.

[15] P. Rullhusen, X. Artru and P. Dhez, Novel radiation sources using relativistic electrons from infrared to X-rays, Series on Synchrotron Radiation Techniques and Applications, Vol 4 (World Scientific, 1998).

[16] A. Hofmann, Characteristics of synchrotron radiation, Proc. of the CERN Accelerator School, Grenoble, France, April 1996, Ed. S. Turner, CERN 98-04 (1998).

[17] R. Jung, Precision emittance measurements in LEP with imaging telescopes, comparison with wire scanner and X-ray detector measurements, CERN SL/95-63(BI) (1995).

[18] R. Coisson, Angular-spectral distribution and polarization from a 'short magnet', Phys. Rev. **A20**, (1979) 524.

[19] R. Bossart, J. Bosser, L. Burnod, R. Coisson, E. D'Amico, A. Hofmann and L. Mann, Observation of visible synchrotron radiation emitted by a high-energy proton beam at the edge of a magnetic field, Nucl. Instrum. & Methods. **164**, 375–380 (1979).

[20] R. P. Walker, Insertion devices: undulators and wigglers, Proc. of the CERN Accelerator School, Grenoble, France, April 1996, Ed. S. Turner, CERN 98-04 (1998).

[21] F. Méot, A theory of low-frequency far-field synchrotron radiation, Part. Accel. **62**, 215–239 (1999).

[22] Private communication, D. Tommasini, CERN.

[23] F. Méot, L. Ponce and N. Ponthieu, low-frequency interference between short synchrotron radiation sources, Phys. Rev. ST- Accelerators and Beams **4**, 063801 (2001).

[24] D. Garreta, J. C. Faivre, First Version of Zgoubi, Dph-N report, unpublished (CEA, Saclay, 1972).

[25] F. Méot, Synchrotron radiation interferences at the LEP mini-wiggler, CERN SL/94-22-AP (1994).

[26] C. Bovet, A. Burns, F, Méot, M. Placidi, E. Rossa, J. de Vries, Synchrotron radiation interferences between short dipoles at LEP, CERN-SL/97-59 BI (1997).

[27] A. Burns, Measurements of intensity of synchrotron light spots for different miniwiggler currents, SL-Note 97-38 BI (1997).

[28] F. Méot and S. Valero, Zgoubi user's guide, DSM/DAPNIA/SEA-97-13 (CEA, Saclay, 1997).

[29] L. Ponce and F. Méot, Undulator radiation simulation tool in view of proton beam diagnostics in LHC, SL-Note-2001-038 BI and DSM/DAPNIA/SEA-01-13 (2001).

[30] F. Méot, Raytracing in 3-D field maps with Zgoubi, internal report CEA/LNS/GT/90-01 (1990).

[31] L. Cadet, Diagnostic par rayonnement synchrotron des faisceaux de protons du LHC, DSM/DAPNIA/SEA-99-06 (CEA, Saclay, 1999).

[32] J. Bosser, C. Bovet and R. Jung, Preliminary studies on a profile monitor for the LHC using Synchrotron radiation, LHC/Note 192 and PS/BD Note 92-03 (1992).

[33] A. P. Sabersky, The geometry and optics of synchrotron radiation, Part. Acc. **5**, 199–206 (1973).

[34] C. Bovet, G. Burtin, R. J. Colchester, B. Halvarsson, R. Jung, S. Levitt, J. M. Vouillot, The LEP synchrotron light monitors, CERN SL/91-25 (BI) (1991).

[35] Private communication, P. Elleaume, ESRF.

[36] Private communication of the magnetic field maps simulated with ROXIE, S. Russenschuck.

[37] Private communication of the magnetic field maps simulated with OPERA 3D, M. Sassowsky.

[38] P. A. Komorowski, Electromagnetic design study of the 5 T superconducting undulator for the proton synchrotron light source and LHC beam diagnostics, LHC-MMS Technical Note 2002-01 (2002).

[39] O. Chubar and P. Elleaume, SRW software, ESRF.

[40] CCD Matrix S7171-0909, Hamamatsu, Japan.

[41] CCD Matrix TH7863, Thomson, France.

[42] M. Chossat, Mathématiques de l'ingénieur: Aide mémoire (Dunod, Paris, 1977).

[43] G. Burtin, R. J. Colchester, J. J. Gras, R. Jung, J. M. Vouillot, Adaptative optics for the LEP 2 synchrotron light monitors, CERN SL-99-049 BI (1999).

[44] K. Honkavaara, X. Artru, R. Chehab, A. Variola, Considerations on the diffraction limitations to the spatial resolution of optical transition radiation, Part. Accel. **63**, 147–170 (1999).

[45] J. W. Goodman, Introduction to Fourier Optics, 2nd ed. (MacGraw-Hill, New York, 1996).

[46] J.-P. Pérez, Optique, Enseignement de la Physique, 5ème édition (Masson, Paris, 1996).

[47] O. Chubar and P. Elleaume, Accurate and efficient computation of synchrotron radiation in the near field region, Proc. European Particle Accelerator Conf., Stockholm, Sweden, 1998, Ed. S. Myers, L. Lijeby, Ch. Petit-Jean-Genaz, J. Poole, K. G. Rensfelt (Bristol, I.O.P, 1998), pp. 1177–1179 (1998).

[48] L. Ponce, Diagnostic par rayonnement synchrotron des faisceaux de protons du LHC, Ph.D. thesis, Institut National Polytechnique de Grenoble, 2002.

[49] Zemax, Optical Design Program, Focus Software, Inc.